UNIVERSITY OF CALIFORNIA, SAN DIEGO

Ultrasound-Responsive Particles for Cancer Diagnostics and Therapeutics

A dissertation submitted in partial satisfaction of the
requirements for the degree of Doctor of Philosophy

in

Electrical Engineering (Photonics)

by

Michael Jerome Benchimol

Committee in charge:

Professor Sadik Esener, Chair
Professor Michael Heller
Professor Yu-Hwa Lo
Professor Roger Tsien
Professor Deli Wang

2012

The Dissertation of Michael Jerome Benchimol is approved, and it is acceptable in quality and form for publication on microfilm and electronically:

_____

_____

_____

_____

_____
Chair

University of California, San Diego

2012

DEDICATION

I dedicate this dissertation to:

My mother and father, for supporting me through all my studies and always caring for my best interest.

My brother Larry, for being an awesome friend, a man of principle, and a role model.

My girlfriend Begüm, for making the past few years a joy and for putting up with me through the stressful times.

EPIGRAPH

I guess I can pick up this lying around project again tomorrow.
I just hope I don't lose my momentum.

Daria Morgendorffer

TABLE OF CONTENTS

LIST OF FIGURES

LIST OF TABLES

ACKNOWLEDGEMENTS

Professor Sadik Esener has been an amazing advisor and a huge inspiration in my time at UCSD. From his guidance with research to helping me make the transition to the life sciences to writing papers and proposals to preparing scientific presentations and many many other things, his help and advice have been beyond measure. His positivity is contagious, thankfully, for the frustrating times when he was able to lift my spirits. His guidance and inventiveness have led to many interesting and impactful projects. The freedom that Prof. Esener gave me in pursuing different ideas allowed me to have a fun and exciting graduate school experience and to learn the research independence to move a project forward.

I would like to thank the members of my excellent committee, which included Professors Sadik Esener, Michael Heller, Yu-Hwa Lo, Roger Tsien, and Deli Wang. This group is truly a blend of creativity, brilliance, positivity, and entrepreneurialism that was always capable of generating ideas in my exams.

Inanc Ortac was a great classmate and friend to suffer through difficult optics homework with and share wild ideas for class presentations. The lighthearted atmosphere he created in lab was always welcome.

Hod Finkelstein helped me with my focus in research and taught me a lot about photodetectors while I was working with him on single-photon avalanche diodes.

Mark Hsu gave me much hands-on training with optical systems and later helped in the testing and optimization of ultrasound modulated fluorescent microbubbles discussed in Chapter 6.

Stuart Ibsen taught me the importance of sticking up for myself.

Dmitri Simberg taught me about chemistry, fabrication of microbubbles, emulsions, liposomes, and generally lipid-based particles. His creation of the first microbubble-incorporating

liposome enabled virtually all of the work described in Chapter 2. His inventiveness and love of technology made for many interesting experiments.

Ahmet Erten had the drive to get the lab up to speed on microfluidic device design and manufacturing, and fortunately pass on some of that knowledge to me.

Jason Steiner helped explain to me about many biological assays and also enjoyed discussing science and philosophy at length.

Corbin Clawson was responsible for many interesting lunchtime debates and entrepreneurial discussions. His fondness for spelunking and magic fruit are memorable.

Carolyn Schutt helped with many cell experiments as well as microscope analysis of fluorescent microbubbles.

Professor David Hall contributed to fluorescence modulation concepts described in Chapter 6 and also helped me with fluorescence and fluorescence lifetime imaging.

Brad Messmer was an important creative mind to have brainstorming sessions with and have the foresight to identify downstream challenges and strategize accordingly.

Gen Yong was a huge help working on virus and plasmid delivery. Working with Gen was always a delight, no matter how challenging it was for us to reproduce other people's published "results".

Dr. Robert Mattrey was a voice of guidance in all of the ultrasound related projects. The ultrasound equipment which he graciously allowed me to use was very enabling for my work.

Professor Roger Tsien contributed many helpful concepts to the enzyme prodrug concept discussed in Chapter 4. His knowledge and recommendations helped bring the technology to a stage ready for animal testing.

Roy Weinstain was a great help in incorporating enzymes within liposomes. His chemistry expertise helped in optimizing bioconjugation as well as guiding the parameters used in the liposome fabrication.

Chris Barback was indispensible in the mouse experiments described in Chapter 3. His broad knowledge and willingness to help in all aspects were much appreciated.

Professor Clark Wu's vast knowledge of acoustics and clinical ultrasound devices was very important in helping me understand the physical mechanisms behind many of the observed acoustical phenomena as well as the clinical relevance of different ultrasound contrast agents.

Daniel Kagan had an admirable focus that allowed the development of record setting microrockets from the concept stage in a very short amount of time.

Chapter 2 contains materials from Ibsen, Stuart; Benchimol, Michael; Simberg, Dmitri; Schutt, Carolyn; Steiner, Jason; Esener, Sadik. "A novel nested liposome drug delivery vehicle capable of ultrasound triggered release of its payload", Journal of Controlled Release, vol. 155, 2011. The dissertation author was a primary investigator of this paper.

Chapter 3, in part, is being prepared for submission for publication as Benchimol, Michael; Barback, Christopher; Ibsen, Stuart; Simberg, Dmitri; Wu, Zhe; Mattrey, Robert; Esener, Sadik. "An Ultrasound-Ruptured Liposome Using Cavitation Threshold Reducing Nanoparticles". The dissertation author is the primary investigator of this paper.

Chapter 4, in part, is being prepared for submission for publication as Benchimol, Michael; Weinstain, Roy; Ibsen, Stuart; Simberg, Dmitri; Tsien, Roger; Esener, Sadik. "Ultrasound-Directed Exposure of Asymmetric Beta-lactamase Liposomes". The dissertation author is the primary investigator of this paper.

Chapter 5, in part, contains material from Kagan, Daniel; Benchimol, Michael; Claussen, Jonathan; Chuluun-Erdene, Erdembileg; Esener, Sadik; Wang, Joseph. "Acoustic Droplet Vaporization and Propulsion of Perfluorocarbon-Loaded Microbullets for Targeted Tissue Penetration and Deformation", Angewandte Chemie, vol. 51, 2012. The dissertation author was a primary investigator of this paper.

Chapter 6, in part, has been submitted for publication as it may appear in Soft Matter, Benchimol, Michael; Hsu, Mark; Schutt, Carolyn; Hall, David; Mattrey, Robert; Esener, Sadik. "Phospholipid/Carbocyanine Dye-Shelled Microbubbles as Ultrasound-Modulated Fluorescent Contrast Agents". The dissertation author is a primary investigator of this paper.

VITA

2006	Bachelor of Science, Boston University
2008	Master of Science, University of California, San Diego
2012	Doctor of Philosophy, University of California, San Diego

PUBLICATIONS

S. Ibsen, M. Benchimol, D. Simberg, C. Schutt, J. Steiner, S. Esener, "A Novel Nested Liposome Drug Delivery Vehicle Capable of Ultrasound Triggered Release of its Payload," Journal of Controlled Release 155(3) (2011)

D. Kagan, M. Benchimol, J. Claussen, E. Chuluun-Erdene, S. Esener, J. Wang, "Acoustic Droplet Vaporization and Propulsion of Perfluorocarbon-Loaded Microbullets for Targeted Tissue Penetration and Deformation," Angewandte Chemie 124, 1-5 (2012)

S. Ibsen, M. Benchimol, S. Esener, "Fluorescent Microscope System to Monitor Real-Time Interactions between Focused Ultrasound, Echogenic Drug Delivery Vehicles, and Live Cell Membranes," *In Press*

G. Shi, W. Cui, M. Benchimol, Y.-T. Liu, S. Kesari, R. Mattrey, S. Esener, D. Simberg, "Isolation of Rare Cancer Cells from Blood with Perfluorocarbon Gas Immuno-Microbubbles," *Submitted to* PLoS ONE

M. Benchimol, M. Hsu, C. Schutt, D. Hall, R. Mattrey, S. Esener, "Ultrasound-Induced Fluorescence Modulation of Microbubble Contrast Agents," *Submitted to Soft Matter*

M. Benchimol, C. Barback, S. Ibsen, D. Simberg, Z. Wu, R. Mattrey, S. Esener, "An Ultrasound-Ruptured Liposome Using Cavitation Threshold Reducing Nanoparticles," *In Preparation*

M. Benchimol, R. Weinstain, S. Ibsen, D. Simberg, R. Tsien, S. Esener, "Ultrasound-Directed Exposure of Asymmetric Beta-lactamase Liposomes," *In Preparation*

S. Ibsen, M. Benchimol, D. Simberg, S. Esener, "Ultrasound mediated localized drug delivery," Adv. Exp. Med. Biol. 733 145-53 (2012)

FIELDS OF STUDY

Major Field: Electrical Engineering (Photonics)

Studies in Optics & Photonics
Professor Sadik Esener

Studies in Cancer Therapeutics, Diagnostics, and Nanomedicine

ABSTRACT OF THE DISSERTATION

Ultrasound-Responsive Particles for Cancer Diagnostics and Therapeutics

by

Michael Jerome Benchimol

Doctor of Philosophy in Electrical Engineering (Photonics)

University of California, San Diego 2012

Professor Sadik Esener, Chair

Ultrasound is a toolbox for interacting with the human body and especially cancer where there is a need for precision and deep tissue access. Practiced medicinal applications of ultrasound are limited to depositing mechanical energy or probing mechanical properties of tissue. However, when particles capable of harnessing ultrasound energy are interfaced with complex systems, the capabilities of ultrasound become multidimensional and virtually limitless. One such potential investigated in this work is the ability to direct the exposure of encapsulated therapeutic agents to specific tissues. The incorporation of an ultrasound-sensitizing particle into a liposome yields a carrier which can circulate throughout the body and rupture to release its contents when and where ultrasound is applied. Tissues adjacent to the ultrasound focus do not experience a high enough pressure to cause drug release, since the acoustic energy is concentrated in all 3 dimensions.

In vitro experiments have visually and quantitatively demonstrated the rapid fragmentation of liposome membranes as well as the localized release of entrapped molecules. Localized deposition of fluorescent molecules in mice has been demonstrated by intravenous administration of liposomes and application of focused ultrasound to the site of interest. Foreign

enzyme has been hidden and incorporated in liposome membranes so that focused ultrasound can expose the enzyme to its substrate. This ability could be used for enzyme prodrug therapy, where immune evasion and delivery specificity are key challenges needing to be addressed.

Another approach described here aims to break physical barriers to effective delivery. Engineered microstructures can direct concentrated acoustic energy, producing a powerful impulse which allows them to penetrate tissues for efficient delivery. The resulting "microbullet" is 100 times faster than current micromotors and does not rely on the presence of external fuel.

The final portion of this dissertation presents a new fluorescent microbubble contrast agent capable of being tagged by ultrasound for precise localization. Radial oscillations of the microbubble modulate the fluorophore separation and fluorescence emission through a physical mechanism only theorized in the past. By directly attacking the biggest challenges in the field, these new directions for cancer therapeutics and diagnostics promise to evolve into game-changing technologies.

Chapter 1:

Introduction: The Paradigm of Smart Medicine

1.1 How Did We Get Here?

Living things have a strong thirst for survival, needed to reach maturity and propagate their species. Each reacts to the environment in its own way in order to prolong life and promote well being. For human beings, it is natural to seek nourishment, shelter, shade on a hot sunny day, etc. It is also in our nature to respond to illness and injury (e.g. to clean a wound). Many living things share in these preventative and reactive behaviors; however, our innate ability to design and build tools for these purposes sets us apart from the other species, and thus redefines the bounds of nature.

For thousands of years, surgery and medication has been used to treat the sick. Societal evolution necessitated the development of more sophisticated medicine to protect important leaders. In the meantime, civilizations were tested by wars, epidemics, and natural disasters. With the aid of experimentalists, inventors, and pioneering physicians, new techniques became increasingly widespread, until today. Now, (in the United States, at least) anyone can walk into a hospital, and receive better care than what was offered to even the most powerful rulers a century ago. Thus, our existence today is owed to and defined by generations of ancestors who learned how to adapt and survive through courageous innovation. If we wish to follow in their footsteps, then it too is our responsibility to apply our resources, knowledge, and technological advancements for the benefit of human health.

In modern times, antibiotics, vaccines, and other pharmaceutical products have revolutionized the treatment of infections and common illnesses which were once serious problems. For other diseases where these are less applicable, we have been forced to develop alternate approaches. Where there is less of a distinction between a disease target and other healthy tissues, it is a greater challenge to design agents which attack the target only. Such is the case with cancer cells, which are our own, and are therefore often difficult to distinguish even with the best in vitro/in vivo techniques[1-5].

Innovators have found medical applications for many newly developed technologies, no matter how imperfect some may be. For example, although we have long known the dangers of ionizing radiation and its mutagenicity, today radiation therapy is routinely used to treat cancer. For a healthy person with a minor ailment, there is no need to intervene with potentially harmful means. However, for a person suffering from a life-threatening disease such as cancer, the balance is tilted in the favor of action.

1.2 Cancer Treatment

X-ray radiation was first used to treat cancer in the late 19th century, just after its discovery. Since then, radiation therapy has cured many people of cancer. While many advances have been made to localize the radiation, and minimize effects to healthy tissue, there is still significant exposure to healthy tissue regions. This method relies on the body's ability to repair resulting replication errors/mutations. Unfortunately, in a predisposed state, a single mutation is enough to redirect a cell to a cancer pathway. Also, even without triggering carcinogenesis, radiation has many damaging/debilitating local effects such as skin sores, alopecia, incontinence, infertility, brain swelling, and tooth decay.

Surgical methods are some of the oldest medical techniques used to treat cancer, and still remain an active area of innovation (e.g. robotic surgery, image guidance, etc.) However, even with the best techniques, surgery is not always an option due to inaccessibility or excessive danger of cutting critical nerves and/or blood vessels. Ablation techniques are alternatives to surgery which use concentrated energy to kill a region of cells. For example, thermal/cryo-ablation uses intense heating or freezing to destroy tissue. A needle or probe is typically inserted into the desired region, and can be heated with RF, microwaves. By using less invasive procedures, these methods can limit complications associated with the treatment. Other technologies now reaching the clinic can achieve similar results without the need for any incision

or penetration. High intensity focused ultrasound (HIFU) is an example of one such emerging noninvasive method for thermal or mechanical ablation.

As our treatment options become more advanced in the future, we may one day look back on today's methods as crude and barbaric. Existing front-line chemotherapy treatments use highly toxic chemicals, many of which are highly toxic to rapidly dividing cells, the immune system, and vital organs (heart, liver, etc.) Even more, many of these drugs are themselves carcinogens. For an outside observer, it could be hard to believe that some of these were rationally designed, not stumbled upon like the natural remedies which were once the only option. For all these treatments, the fundamental medical rationale remains the same – we have good faith that the potential benefits of intervening outweigh the risks of inaction. Our available treatments are not a consequence of some big pharma conspiracy. The current treatment paradigm exists because regulatory approval takes time and right now it's the best available option. That said, there is a whole lot of room for improvement.

1.3 The Age of Cancer Targeting

As new alternatives emerge, safer and more effective treatments will displace current methods once their benefit has been realized. In this respect, we have made great strides thus far with both pharmaceuticals and physical methods. Many new and upcoming drugs have mechanisms of action which are targeted, or do not decrease the error rate of DNA replication, a source of carcinogenesis[6-8]. After ensuring that a drug is safe enough for use in humans, it must still have a greater toxicity to tumor cells than to other healthy tissues in order to be effective. The figure of merit which defines this property of specificity is the therapeutic index, which for humans is typically defined as:

$$Therapeutic\ Index = \frac{Effective\ Dose}{Toxic\ Dose}$$

For a high therapeutic index, it is easier to achieve an effective dose while avoiding a toxic dose, so the safety margin is larger. Since administered doses are typically limited by these toxicities, increasing the therapeutic index leads to decreased mortality, and increased treatment efficacy[9, 10]. Many chemotherapy drugs used today have a therapeutic index of about 1, meaning that a dose that is effective almost certainly causes toxic side effects[11]. Two main classes of targeted molecular therapeutics have proven successful in achieving a higher therapeutic index than predecessors[12-15]:

1) Monoclonal antibodies/antibody-drug conjugates which target a protein overexpressed by cancer cells (Examples: Trastuzumab (Herceptin®), Bevacizumab (Avastin®), Alemtuzumab (Campath®))
2) Inhibitors of enzymes and other components of cancer-associated signaling pathways (Examples: Imatinib mesylate(Gleevec®), Erlotinib (Tarceva®), Sorafenib (Nexavar®))

The key to successes like these is not the identification of the targeted compounds – discovery and development of these are well defined problems with established methods in the pharmaceutical industry[16]. The real challenge is in identification of the targets themselves. While our ability to profile the massive proteome of different cell types is ever improving, our ability to identify new targets has not kept up. The targets that we have found are only consistent in specific patient subpopulations, and much of the pharmaceutical industry's effort is currently devoted to the development 2nd and 3rd generation therapies of these same few successes[17-19].

A common example of the potential of monoclonal antibody therapeutics is the blockbuster drug trastuzumab (Herceptin®). 20-30% of patients with breast cancer are HER2 positive, meaning the cancer cells overexpress the HER2/neu receptor linked to uncontrolled cell proliferation[20-22]. For these patients, trastuzumab (an antibody to this receptor) is an effective drug with a low toxicity. But the lack of an equally effective alternative for the remaining 80% of

patients highlights the fundamental issue of biochemically targeted therapies: cancer is an incredibly diverse and dynamic system, and it may not always be possible to find a unique druggable differentiator[23]. Even if one is found, cancer's keen ability to evolve and develop resistance can quickly negate the effects, and in some cases incite a more aggressive cancer[24, 25]. Such is the case for trastuzumab, where 66-89% of patients develop resistance[26].

The story of inhibitors has the same theme. The most successful inhibitor cancer therapeutic to-date is imatinib (Gleevec®). For about 80% of patients with chronic myelogenous leukemia (CML), the inhibition of a tyrosine kinase by imatinib can make their disease manageable (though not cured)[27-29]. However, imatinib is not nearly as effective for most other cancers, and a different target with equivalent effectiveness also have yet to be found[30].
The inhibitors which do have a general anti-cancer function are also the ones with the lowest therapeutic index. Topoisomerase inhibitors, for instance, do not target a specific pathway, but instead target enzymes essential to transcription and replication of DNA in any cell. Thus, like other chemotherapeutics which impair cell replication, their main mode of cancer selectivity is based on the rapidly dividing property of cancer cells, and like those same drugs, they too are highly toxic to all dividing cells[31, 32].

1.4 Nanoparticle Cancer Therapeutics

Another class of emerging therapeutics are drug-loaded nanoparticles (NPs). NPs can provide the benefit of long circulation and protection of a drug payload for a more sustained release profile and a lower required dose[33-36]. The chemical versatility and large size of NPs compared to molecules enables modularity, allowing them to incorporate surface components for immune stealthing, targeting, and other functionalities independent of their core payload. However, their unique physicochemical properties are accompanied by associated challenges. NPs can be subject to immune recognition and phagocytosis by immune cells as well as local

accumulation in organs such as the liver, spleen, lungs, and kidneys[37, 38]. If they are above the size which can be safely eliminated through the kidneys (typically 5-15 nm), then they should safely degrade in a short enough time to prevent local tissue effects such as inflammation[39-42]. Additionally, since NPs cannot diffuse into a cell like a small molecule, they must be actively taken into the cell (usually by endocytosis), or degrade and release their payload in the cell's vicinity[43-45]. If endocytosed, the particle or drug must then be able to escape the endosome so it can reach its biological target located in another compartment of the cell[46, 47].

To outweigh all of these challenges, NPs must leverage all of their potential strengths, especially their ability to improve on specificity of delivery. Many properties of NPs can be exploited to alter their pharmacokinetic properties. Their surface can be functionalized with targeting components (e.g. ligands, aptamers, antibodies) made to bind specifically to receptors overexpressed by cancers[48-52]. These components for "active" targeting can function by binding a certain cell surface receptor, or by additionally inducing cell internalization of the NP[53, 54]. Although this idea has existed for decades, there are still no FDA approved actively-targeted cancer NPs. As discussed previously, one reason is that our inability to find these unique receptors is a barrier to achieving specific delivery. Even if the NP can effectively limit its nonspecific accumulation, receptors present in other tissues result in off-target accumulation and depletion of the NPs from circulation.

1.5 Passive Targeting via the Enhanced Permeation and Retention (EPR) Effect

The physical properties of NPs alone (namely size) can be controlled for "passive" targeting of tumors via the enhanced permeability and retention (EPR) effect. The irregularity of rapidly growing tumor vasculature imparts a distinct geometry with significantly larger inter-cell spacing compared to the usually encountered tight junction[55-57]. These gaps allow small NPs to extravasate, where the vascular system present in other tissues will not[58-60]. Thus, by carefully

tailoring the size of a NP, one can maximize the probability that it will end up in the interstitial space near a cancer cell[61-64]. Once in this space, the NPs should degrade, release their payload, or be taken up by cells before random diffusion causes them to be washed out.

The EPR effect should also be optimized for ligand-targeted NPs, since the NPs will have to extravasate before reaching their target receptor on a cancer cell[65]. Targeting the neovasculature near a tumor can bypass this need, but this approach achieves a different goal than treating cancer cells directly.

Many physical means have the ability to locally ablate specific tissues, as alternatives to surgery or in cases where surgery is not an option. Nonionizing electromagnetic radiation such as radio frequency and near-infrared light have been used to cause hyperthermia. Since diffraction and scattering limit the ability to precisely focus these types of energy in tissue, nanoparticles are often used to locally concentrate the energy[66, 67]. Some examples of these are magnetic iron oxide nanoparticles for radio frequency and gold nanoparticles for near infrared[68-70]. The presumption for doing this is that nanoparticles can be targeted by some means with greater specificity than the diffuse energy source. If there is selective accumulation of the nanoparticles in off-target tissues distant from the tumor, these can potentially be avoided by directing the energy source away from this region.

One limitation of using a physically focused method is the need for a priori knowledge of the tumor location, if it is too unpractical to scan the source across the whole body. Even if it would be possible to do so, a whole body scan would negate the benefits of selectivity, unless energy-concentrating particles were targeted to the tissue of interest, and the source was kept away from susceptible vital organs. With modern imaging techniques, we typically have location information before beginning treatment, but in advanced cases where there are many metastatic lesions, it can be difficult to find each individual lesion, some of which may be microscopic and

distant from the primary tumor. Therefore, without the ability to scan across the whole body, treating these advanced patients with local methods may be inadequate.

One relevant finding shows that 90% of cancer deaths occur due to metastasis[71, 72]. This commonly misinterpreted statistic is often used as justification for the development of therapies designed for late stage cancer treatment. This is akin to asserting that to save heart disease patients, we should focus all efforts on emergency heart attack treatments, and forego all attempts at early treatment. Without question, treating metastasis is necessary. However, although metastasis is the final stage of most cancer fatalities, it is unclear how many of these cancers can be intercepted at an earlier stage, preventing the occurrence of metastasis.

1.6 A Statistical Context to Cancer and Metastasis

Table 1.1 shows the rate of incidence and death by cancer site, and the fraction of patients who present metastasis at the time of detection. These data were taken from the National Cancer Institute website (cancer.gov), provided by their Surveillance Epidemiology & End Results (SEER) Program fact sheets. A weighted average across the different cancer sites shows that as a whole, 20.9% of cancer patients have metastatic cancer at the time of diagnosis. When compared to the total # of deaths/total # incidences (41.4%), it appears that for every death in which the cancer was detected at a late stage, there is one death in which the cancer was detected at an earlier stage.

Breast cancer is a good example of the significance of this, likely due to the prevalence of screening methods. In breast cancer (in the U.S.), 5% of patients have metastatic disease at the time of detection, or about 10,000 women a year have this diagnosis. Every year however, about 40,000 women die of breast cancer[73]. It is evident that most of these patients were originally diagnosed with localized or regional cancer. In other words, over 70% of breast cancer deaths in the U.S. are of patients where no metastasis was seen at the time of detection. As technological

advancements move us towards earlier detection, there will be a growing opportunity to treat the disease at these early stages. Thus, while we continue to develop systemic treatments for metastasis, we need to rethink our approach to develop alternate technologies for localized treatments that capitalize on our successes in early detection.

Strategy Going Forward: Delivery Vehicle Design

Analysis of today's cancer treatments have taught us that improvements in the safety and efficacy of treatments are directly tied to increases in specificity. Nanoparticles give us a platform for delivering drugs which is customizable enough to allow targeting components to be incorporated. In order to get the most out of a targeted nanoparticle, it must be made long-circulating to give it a good chance of reaching its target before it is removed from the system. Since the diversity of cancer presents a challenge in targeting a specific biochemical state, we can circumvent this problem by physically directing the action of the nanoparticles after they have been introduced into the system

Table 1.1 Rates of cancer incidence and death in the U.S. by cancer site. These data were taken from the National Cancer Institute website (http://www.cancer.gov), provided by their Surveillance Epidemiology & End Results (SEER) Program fact sheets. For cancer types which were gender restricted or had a strong gender bias (e.g. prostate, breast), rates were adjusted to reflect the impact on the total population. Data was sorted by the number of deaths in descending order.

Cancer Site	Age-adjusted Incidence per 100k Men & Women	Age-adjusted Deaths per 100k Men & Women	% With Distant (Metastatic) Cancer at Diagnosis
Lung	62	51.6	56
Colorectal	47.2	17.1	20
Prostate	78	11.8	4
Breast	62	11.75	5
Pancreatic	12	10.8	53
Lymphoma	22.7	7.1	46
Leukemia	12.5	7.1	Uncited
Liver	7.3	5.3	19
Bladder	21.1	4.4	4
Brain & Other Nervous System	6.5	4.3	2
Esophagus	4.5	4.3	32
Ovarian	6.4	4.2	62
Kidney & Renal Pelvis	14.6	4	18
Stomach	7.7	3.7	34
Myeloma	5.7	3.5	95
Skin	22.7	3.5	Uncited
Oral Cavity &	10.6	2.5	15
Cervix Uteri	4.05	2.4	12
Corpus & Uterus	11.95	2.1	8
Soft Tissue (Including Heart)	3.3	1.3	15
Larynx	3.4	1.2	17
Vulva	1.15	1	5
Thyroid	11	0.5	5
Bone & Joint	0.9	0.4	Uncited
Small Intestine	2	0.4	27
Other Endocrine	0.7	0.3	Uncited
Testicular	2.75	0.2	12
Anal	1.6	0.2	12
Eye & Orbit	0.8	0.1	Uncited

1.7 Cancer Diagnostics

Cancer detection and monitoring are as vital as treatments, since the more we know about a problem, the better chance we will have at solving it. Among the multitude of available tools, imaging techniques are the main methods used to detect and locate solid tumors. Biopsies are often taken to confirm a diagnosis, but usually after another method has detected a suspicious tissue mass. Less invasive methods are much better tolerated by patients and can reduce exam associated risks[74]. However, some of these exams expose the patient to ionizing radiation, which has its own set of risks. Although non-ionizing imaging modalities exist (MRI, ultrasound), other modalities are often chosen due to their low cost or better accuracy. X-ray imaging is a common diagnostic tool for even mild injuries, since a single x-ray image involves only a very small radiation exposure. However, a patient exposed to repeated x-ray scans (as done in CT to build 3-dimensional images) quickly accumulates a large radiation dose.

Positron emission tomography (PET) is one of the most sensitive and accurate imaging modalities for cancer diagnosis and staging[75-79]. A key reason for this is that it generates functional information based on the metabolic rates of different tissues. Thus, where another modality may not be able to distinguish a benign mass from a malignant mass, in PET, only the malignant mass will appear "hot", due to its high uptake of radioactive glucose[80, 81]. Unfortunately, PET relies on the systemic administration of a radioactive contrast agent which results in a radiation exposure equivalent to few hundred chest x-rays, similar to the dose given in CT scans[82, 83]. Diagnostic exams of this nature bring a non-negligible risk of carcinogenesis, which radiologists consider in designing an exam schedule[84, 85]. In order not to cause excessive exposure, the yearly number of PET scans which a patient can receive is limited, and even more so if a PET/CT scan is performed or the patient has had other radiation exposures. The disease may be progressing quickly while waiting for the next opportunity to monitor the efficacy of the last treatment. Exam cost is also a great limiting factor, due to the expensive machinery required

and especially for PET where the unstable radiopharmaceuticals are typically produced off-site the same day due to their short half-life (110 min. for ^{18}F-FDG)[86, 87].

For the above-mentioned reasons, the most accurate detection technologies are not suitable for early screening procedures. Instead, procedures such as x-ray mammography are favored, despite their non-negligible radiation exposures and high inaccuracy rates which pose the risk of unnecessary treatment.

The new generation of contrast-enhanced and contrast-free imaging modalities is looking to provide similar functional information in a safer and less costly manner. This would allow more frequent disease monitoring for the patients who are at the greatest risk, as well as the potential for accessible and accurate cancer screening. The same benefits that exist for targeted therapeutic particles also apply for targeted contrast agents, but with less stringent requirements. Since contrast agents are generally very biocompatible and have little to no cytotoxicity, it is not dangerous if they accumulate in healthy tissue regions. Radiologists are trained to know these consistently high signal regions, and therefore focus on abnormal sites.

1.8 Ultrasound: A Versatile Tool for Medicine

Well controlled ultrasound waves are very safe, which explains their use in prenatal imaging (obstetric ultrasonography)[88, 89]. Since acoustic energy is strictly mechanical, there is no risk of exposure to ionizing radiation present in other imaging modalities. The ability to focus non-ionizing energy through deep tissue, while still maintaining the ability to safely interact, is a rare and powerful combination of properties. While ultrasound waves are subject to the same limitations as all waves (wavelength-dependent diffraction, scattering, etc.), there exists a favorable window which allows both tight focusing and good tissue penetration. The speed of sound in soft tissue ranges from 1400-1700 m/s, and up to ~4000 m/s in bone[90]. Therefore, at a frequency of 3 Mhz, the wavelength is $\approx$ 0.5 mm in soft tissue. At this frequency, the 6 dB

penetration depth through breast fat is 59 mm and the use of lower frequencies allows for even greater penetration due to lower tissue absorption and scattering[91, 92].

While low intensity ultrasound can be applied for extended durations without causing any harm, higher intensity ultrasound can be used to induce tissue damage. This damage can either be due to excess amounts of absorbed energy, or due to higher peak pressures. The former case leads to hyperthermia, and the latter results in mechanical damage due to a pressure-based phenomenon known as cavitation.

1.9 Acoustic Cavitation

Cavitation is the formation and/or collapse of a gaseous cavity (bubble) in liquid due to pressure changes[93]. Specifically, the low or negative pressure induced by sound waves or rapid motion causes vaporization of the liquid in a process analogous to boiling. When the pressure returns back to normal, the newly formed bubble will often collapse/implode on itself. The rate at which the bubble retracts greatly exceeds the rate of heat transfer, and is therefore a nearly adiabatic process[94, 95]. Since a micron-sized bubble will collapse to a nanoscopic scale, heat will quickly collect in this pinpoint, causing temperatures to reach near 5000°K, near the temperature on the surface of the sun[96, 97]. At this temperature, a significant amount of radiation is emitted, including ultraviolet light and higher energy waves which produce free radicals[98, 99]. High temperatures are just one of the proposed sources of light from this phenomenon known as sonoluminescence. This extreme heat is very tightly confined, so that most of the surrounding matter is not exposed to these temperatures.

A more pronounced consequence of the bubble formation and collapse is a powerful shockwave which extends tens of microns[100]. These shockwaves when repeated are capable of breaking membranes, lysing cells and generally damaging tissue architecture[101-105]. Asymmetric collapse of the bubble due to structural imperfections or interactions with nearby objects leads to

formation of powerful jets which are more directed, and share the same potential for disrupting structures[106, 107].

1.10 Insonation Regimes

There are 4 different regimes in which an ultrasound system can operate, depending on the pulse parameters, specifically pressure and duty cycle (Fig. 1.1). Ultrasound intensity is a power density proportional to the square of the pressure amplitude. For the frequencies in question, any one of these 4 regimes is practically achievable. The regime producing no hyperthermia or cavitation (shaded green) is the one defined by the FDA (with a safety margin) for diagnostic ultrasound imaging, but in general can be achieved by maintaining a low peak negative pressure (PNP). A high intensity pulse with a low duty cycle can cause cavitation without causing heating (shaded blue) – even a single cycle is adequate to induce cavitation. This is the regime in which therapies like extracorporeal shock wave lithotripsy (ESWL) and sonothrombolysis (not yet approved) operate.

On the other hand, raising the temperature in tissue to a point where there is significant cell death requires the deposition of a considerable amount of energy. One way to achieve this without causing cavitation (shaded red) is to use continuous-wave ultrasound with a low intensity. This is the regime in which HIFU likes to operate in. A high intensity combined with a high duty cycle will cause both cavitation and heating. A complexity arises in the interdependency of cavitation and heating, since they both facilitate each other[108]. Specifically, the cavitation threshold decreases with increasing temperature, due to an increase in the vapor pressure and the presence of bubbles formed through cavitation causes an increase in the local acoustic absorbance, which accelerates tissue heating[109]. To circumvent this problem, the “off” time between ultrasound pulses can be adjusted to allow time for the heat to subside or the vapor bubbles to dissolve back into the liquid[110].

Figure 1.1 Four general ultrasound pulsing regimes. At a constant temperature and frequency, the production of cavitation or appreciable heat by ultrasound is a function of the acoustic pressure and duty cycle of the ultrasound. Achieving either heating, or cavitation, or both, or neither are all possible by tailoring the pulsing scheme. The independent parameters are frequency, pressure, pulse length (# cycles), and duty cycle (% time on).

The threshold at which cavitation occurs is a function of the peak-negative pressure (PNP) and the frequency of the ultrasound[111]. The FDA has safety limits in place for diagnostic ultrasound based on these two parameters. To be a safe distance from the cavitation regime, the mechanical index (MI) must be below 1.9. In order to prevent appreciable heating, the spatial peak temporal average intensity (I_{SPTA}) must be below 720 mW/cm^2.

$$I = \frac{p^2}{2Z}$$

$$MI = \frac{PNP}{\sqrt{f}}$$

, where I is the intensity, p is the pressure amplitude, and Z is the acoustic impedance.

1.11 Scope of Dissertation

The work presented in this dissertation is based on acoustic phenomena which occur in the non-thermal ultrasound regimes (green and blue in Fig 1.1). Chapters 2-4 cover cavitation-driven carrier delivery systems. Chapter 5 presents a novel cavitation-driven propulsion mechanism which may also in the future be used as a delivery vehicle. Chapter 6 presents a fluorescent microbubble contrast agent which operates in the regime absent of cavitation. Instead, the microbubble fluctuates in size similar to clinically-used ultrasound contrast agents[112]. The continued oscillation of a bubble is sometimes referred to as "stable" cavitation, in which case the terminal collapse mode discussed earlier is differentiated by the term "inertial" cavitation.

1.12 References

1. Hanash, S.M., Baik, C.S. & Kallioniemi, O. Emerging molecular biomarkers--blood-based strategies to detect and monitor cancer. *Nature reviews. Clinical oncology* **8**, 142-150 (2011).

2. Konforte, D. & Diamandis, E.P. Is Early Detection of Cancer with Circulating Biomarkers Feasible? *Clinical chemistry* (2012).

3. Chen, J., Li, J. & Sun, Y. Microfluidic approaches for cancer cell detection, characterization, and separation. *Lab on a chip* **12**, 1753-1767 (2012).

4. Smith, R.A. et al. Cancer screening in the United States, 2011: A review of current American Cancer Society guidelines and issues in cancer screening. *CA: a cancer journal for clinicians* **61**, 8-30 (2011).

5. Shi, L. et al. Exploring the uncertainties of early detection results: model-based interpretation of mayo lung project. *BMC cancer* **11**, 92 (2011).

6. Benedict, W.F., Baker, M.S., Haroun, L., Choi, E. & Ames, B.N. Mutagenicity of cancer chemotherapeutic agents in the Salmonella/microsome test. *Cancer research* **37**, 2209-2213 (1977).

7. Marquardt, H., Philips, F.S. & Sternberg, S.S. Tumorigenicity in vivo and induction of malignant transformation and mutagenesis in cell cultures by adriamycin and daunomycin. *Cancer research* **36**, 2065-2069 (1976).

8. Adamson, R.H. & Seiber, S.M. Chemically induced leukemia in humans. *Environmental health perspectives* **39**, 93-103 (1981).

9. Papahadjopoulos, D. et al. Sterically stabilized liposomes: improvements in pharmacokinetics and antitumor therapeutic efficacy. *Proceedings of the National Academy of Sciences of the United States of America* **88**, 11460-11464 (1991).

10. Craig, J.B. & Powell, B.L. The management of nausea and vomiting in clinical oncology. *The American journal of the medical sciences* **293**, 34-44 (1987).

11. Bonadonna, G., Monfardini, S., De Lena, M. & Fossati-Bellani, F. Clinical evaluation of adriamycin, a new antitumour antibiotic. *British medical journal* **3**, 503-506 (1969).

12. Beck, A., Wurch, T., Bailly, C. & Corvaia, N. Strategies and challenges for the next generation of therapeutic antibodies. *Nature reviews. Immunology* **10**, 345-352 (2010).

13. Weiner, L.M. & Borghaei, H. Targeted therapies in solid tumors: monoclonal antibodies and small molecules. *Human antibodies* **15**, 103-111 (2006).

14. Pietras, K. et al. STI571 enhances the therapeutic index of epothilone B by a tumor-selective increase of drug uptake. *Clinical cancer research : an official journal of the American Association for Cancer Research* **9**, 3779-3787 (2003).

15. Junutula, J.R. et al. Site-specific conjugation of a cytotoxic drug to an antibody improves the therapeutic index. *Nature biotechnology* **26**, 925-932 (2008).

16. Kerns, E.H. & Di, L. Pharmaceutical profiling in drug discovery. *Drug discovery today* **8**, 316-323 (2003).

17. Wistuba, II, Gelovani, J.G., Jacoby, J.J., Davis, S.E. & Herbst, R.S. Methodological and practical challenges for personalized cancer therapies. *Nature reviews. Clinical oncology* **8**, 135-141 (2011).

18. Abramson, V. & Arteaga, C.L. New strategies in HER2-overexpressing breast cancer: many combinations of targeted drugs available. *Clinical cancer research : an official journal of the American Association for Cancer Research* **17**, 952-958 (2011).

19. Shah, N.P. et al. Overriding imatinib resistance with a novel ABL kinase inhibitor. *Science* **305**, 399-401 (2004).

20. Montemurro, F. et al. Outcome of patients with HER2-positive advanced breast cancer progressing during trastuzumab-based therapy. *The oncologist* **11**, 318-324 (2006).

21. Slamon, D.J. et al. Human breast cancer: correlation of relapse and survival with amplification of the HER-2/neu oncogene. *Science* **235**, 177-182 (1987).

22. Gullick, W.J. et al. c-erbB-2 protein overexpression in breast cancer is a risk factor in patients with involved and uninvolved lymph nodes. *British journal of cancer* **63**, 434-438 (1991).

23. Swanton, C., Burrell, R.A. & Futreal, P.A. Breast cancer genome heterogeneity: a challenge to personalised medicine? *Breast cancer research : BCR* **13**, 104 (2011).

24. Ellis, L.M. & Hicklin, D.J. Resistance to Targeted Therapies: Refining Anticancer Therapy in the Era of Molecular Oncology. *Clinical cancer research : an official journal of the American Association for Cancer Research* **15**, 7471-7478 (2009).

25. Lo, H.W. EGFR-targeted therapy in malignant glioma: novel aspects and mechanisms of drug resistance. *Current molecular pharmacology* **3**, 37-52 (2010).

26. Nahta, R., Yu, D., Hung, M.C., Hortobagyi, G.N. & Esteva, F.J. Mechanisms of disease: understanding resistance to HER2-targeted therapy in human breast cancer. *Nature clinical practice. Oncology* **3**, 269-280 (2006).

27. Peggs, K. & Mackinnon, S. Imatinib mesylate--the new gold standard for treatment of chronic myeloid leukemia. *The New England journal of medicine* **348**, 1048-1050 (2003).

28. Deininger, M., Buchdunger, E. & Druker, B.J. The development of imatinib as a therapeutic agent for chronic myeloid leukemia. *Blood* **105**, 2640-2653 (2005).

29. Oravecz-Wilson, K.I. et al. Persistence of leukemia-initiating cells in a conditional knockin model of an imatinib-responsive myeloproliferative disorder. *Cancer cell* **16**, 137-148 (2009).

30. von Mehren, M. Targeted therapy with imatinib: hits and misses? *Journal of clinical oncology : official journal of the American Society of Clinical Oncology* **23**, 8-10 (2005).

31. Pommier, Y. Topoisomerase I inhibitors: camptothecins and beyond. *Nature reviews. Cancer* **6**, 789-802 (2006).

32. Nitiss, J.L. Targeting DNA topoisomerase II in cancer chemotherapy. *Nature reviews. Cancer* **9**, 338-350 (2009).

33. Davis, M.E., Chen, Z.G. & Shin, D.M. Nanoparticle therapeutics: an emerging treatment modality for cancer. *Nature reviews. Drug discovery* **7**, 771-782 (2008).

34. Kukowska-Latallo, J.F. et al. Nanoparticle targeting of anticancer drug improves therapeutic response in animal model of human epithelial cancer. *Cancer research* **65**, 5317-5324 (2005).

35. Kawasaki, E.S. & Player, A. Nanotechnology, nanomedicine, and the development of new, effective therapies for cancer. *Nanomedicine : nanotechnology, biology, and medicine* **1**, 101-109 (2005).

36. Cho, K., Wang, X., Nie, S., Chen, Z.G. & Shin, D.M. Therapeutic nanoparticles for drug delivery in cancer. *Clinical cancer research : an official journal of the American Association for Cancer Research* **14**, 1310-1316 (2008).

37. Brannon-Peppas, L. & Blanchette, J.O. Nanoparticle and targeted systems for cancer therapy. *Advanced drug delivery reviews* **56**, 1649-1659 (2004).

38. Peer, D. et al. Nanocarriers as an emerging platform for cancer therapy. *Nature nanotechnology* **2**, 751-760 (2007).

39. Schmidt, M.M. & Wittrup, K.D. A modeling analysis of the effects of molecular size and binding affinity on tumor targeting. *Molecular cancer therapeutics* **8**, 2861-2871 (2009).

40. Li, S.D. & Huang, L. Pharmacokinetics and biodistribution of nanoparticles. *Molecular pharmaceutics* **5**, 496-504 (2008).

41. Choi, H.S. et al. Tissue- and organ-selective biodistribution of NIR fluorescent quantum dots. *Nano letters* **9**, 2354-2359 (2009).

42. Choi, H.S. et al. Renal clearance of quantum dots. *Nature biotechnology* **25**, 1165-1170 (2007).

43. Bareford, L.M. & Swaan, P.W. Endocytic mechanisms for targeted drug delivery. *Advanced drug delivery reviews* **59**, 748-758 (2007).

44. Gan, Q. et al. Effect of size on the cellular endocytosis and controlled release of mesoporous silica nanoparticles for intracellular delivery. *Biomedical microdevices* **14**, 259-270 (2012).

45. Wang, S.H., Lee, C.W., Chiou, A. & Wei, P.K. Size-dependent endocytosis of gold nanoparticles studied by three-dimensional mapping of plasmonic scattering images. *Journal of nanobiotechnology* **8**, 33 (2010).

46. Varkouhi, A.K., Scholte, M., Storm, G. & Haisma, H.J. Endosomal escape pathways for delivery of biologicals. *Journal of controlled release : official journal of the Controlled Release Society* **151**, 220-228 (2011).

47. Paillard, A., Hindre, F., Vignes-Colombeix, C., Benoit, J.P. & Garcion, E. The importance of endo-lysosomal escape with lipid nanocapsules for drug subcellular bioavailability. *Biomaterials* **31**, 7542-7554 (2010).

48. Moghimi, S.M., Hunter, A.C. & Murray, J.C. Long-circulating and target-specific nanoparticles: theory to practice. *Pharmacological reviews* **53**, 283-318 (2001).

49. Nobs, L., Buchegger, F., Gurny, R. & Allemann, E. Current methods for attaching targeting ligands to liposomes and nanoparticles. *Journal of pharmaceutical sciences* **93**, 1980-1992 (2004).

50. Liu, Y., Miyoshi, H. & Nakamura, M. Nanomedicine for drug delivery and imaging: a promising avenue for cancer therapy and diagnosis using targeted functional nanoparticles. *International journal of cancer. Journal international du cancer* **120**, 2527-2537 (2007).

51. Ruoslahti, E., Bhatia, S.N. & Sailor, M.J. Targeting of drugs and nanoparticles to tumors. *The Journal of cell biology* **188**, 759-768 (2010).

52. Cirstoiu-Hapca, A., Bossy-Nobs, L., Buchegger, F., Gurny, R. & Delie, F. Differential tumor cell targeting of anti-HER2 (Herceptin) and anti-CD20 (Mabthera) coupled nanoparticles. *International journal of pharmaceutics* **331**, 190-196 (2007).

53. Wang, M. & Thanou, M. Targeting nanoparticles to cancer. *Pharmacological research : the official journal of the Italian Pharmacological Society* **62**, 90-99 (2010).

54. Byrne, J.D., Betancourt, T. & Brannon-Peppas, L. Active targeting schemes for nanoparticle systems in cancer therapeutics. *Advanced drug delivery reviews* **60**, 1615-1626 (2008).

55. Maeda, H., Wu, J., Sawa, T., Matsumura, Y. & Hori, K. Tumor vascular permeability and the EPR effect in macromolecular therapeutics: a review. *Journal of controlled release : official journal of the Controlled Release Society* **65**, 271-284 (2000).

56. Greish, K. Enhanced permeability and retention (EPR) effect for anticancer nanomedicine drug targeting. *Methods in molecular biology* **624**, 25-37 (2010).

57. Maeda, H. Tumor-selective delivery of macromolecular drugs via the EPR effect: background and future prospects. *Bioconjugate chemistry* **21**, 797-802 (2010).

58. Fang, J., Nakamura, H. & Maeda, H. The EPR effect: Unique features of tumor blood vessels for drug delivery, factors involved, and limitations and augmentation of the effect. *Advanced drug delivery reviews* **63**, 136-151 (2011).

59. Maruyama, K. Intracellular targeting delivery of liposomal drugs to solid tumors based on EPR effects. *Advanced drug delivery reviews* **63**, 161-169 (2011).

60. Danquah, M.K., Zhang, X.A. & Mahato, R.I. Extravasation of polymeric nanomedicines across tumor vasculature. *Advanced drug delivery reviews* **63**, 623-639 (2011).

61. Perrault, S.D., Walkey, C., Jennings, T., Fischer, H.C. & Chan, W.C. Mediating tumor targeting efficiency of nanoparticles through design. *Nano letters* **9**, 1909-1915 (2009).

62. Jain, R.K. & Stylianopoulos, T. Delivering nanomedicine to solid tumors. *Nature reviews. Clinical oncology* **7**, 653-664 (2010).

63. Cheng, C.J. & Saltzman, W.M. Nanomedicine: Downsizing tumour therapeutics. *Nature nanotechnology* **7**, 346-347 (2012).

64. Chauhan, V.P. et al. Normalization of tumour blood vessels improves the delivery of nanomedicines in a size-dependent manner. *Nature nanotechnology* **7**, 383-388 (2012).

65. Lammers, T., Kiessling, F., Hennink, W.E. & Storm, G. Drug targeting to tumors: Principles, pitfalls and (pre-) clinical progress. *Journal of controlled release : official journal of the Controlled Release Society* **161**, 175-187 (2012).

66. Cheung, A.Y. & Neyzari, A. Deep local hyperthermia for cancer therapy: external electromagnetic and ultrasound techniques. *Cancer research* **44**, 4736s-4744s (1984).

67. Shenoi, M.M., Shah, N.B., Griffin, R.J., Vercellotti, G.M. & Bischof, J.C. Nanoparticle preconditioning for enhanced thermal therapies in cancer. *Nanomedicine (Lond)* **6**, 545-563 (2011).

68. Huff, T.B. et al. Hyperthermic effects of gold nanorods on tumor cells. *Nanomedicine (Lond)* **2**, 125-132 (2007).

69. Lu, W. et al. Targeted photothermal ablation of murine melanomas with melanocyte-stimulating hormone analog-conjugated hollow gold nanospheres. *Clinical cancer research : an official journal of the American Association for Cancer Research* **15**, 876-886 (2009).

70. Peng, X.H. et al. Targeted magnetic iron oxide nanoparticles for tumor imaging and therapy. *International journal of nanomedicine* **3**, 311-321 (2008).

71. Mehlen, P. & Puisieux, A. Metastasis: a question of life or death. *Nature reviews. Cancer* **6**, 449-458 (2006).

72. Hanahan, D. & Weinberg, R.A. The hallmarks of cancer. *Cell* **100**, 57-70 (2000).

73. DeSantis, C., Siegel, R., Bandi, P. & Jemal, A. Breast cancer statistics, 2011. *CA: a cancer journal for clinicians* **61**, 409-418 (2011).

74. Mortensen, M.B. et al. Prospective evaluation of patient tolerability, satisfaction with patient information, and complications in endoscopic ultrasonography. *Endoscopy* **37**, 146-153 (2005).

75. Di Martino, E. et al. Diagnosis and staging of head and neck cancer: a comparison of modern imaging modalities (positron emission tomography, computed tomography, color-coded duplex sonography) with panendoscopic and histopathologic findings. *Archives of otolaryngology--head & neck surgery* **126**, 1457-1461 (2000).

76. Gould, M.K., Maclean, C.C., Kuschner, W.G., Rydzak, C.E. & Owens, D.K. Accuracy of positron emission tomography for diagnosis of pulmonary nodules and mass lesions: a meta-analysis. *JAMA : the journal of the American Medical Association* **285**, 914-924 (2001).

77. Kubota, K. et al. FDG-PET delayed imaging for the detection of head and neck cancer recurrence after radio-chemotherapy: comparison with MRI/CT. *European journal of nuclear medicine and molecular imaging* **31**, 590-595 (2004).

78. Denecke, T. et al. Comparison of CT, MRI and FDG-PET in response prediction of patients with locally advanced rectal cancer after multimodal preoperative therapy: is there a benefit in using functional imaging? *European radiology* **15**, 1658-1666 (2005).

79. Antoch, G. et al. Whole-body dual-modality PET/CT and whole-body MRI for tumor staging in oncology. *JAMA : the journal of the American Medical Association* **290**, 3199-3206 (2003).

80. Dimitrakopoulou-Strauss, A. et al. The role of quantitative (18)F-FDG PET studies for the differentiation of malignant and benign bone lesions. *Journal of nuclear medicine : official publication, Society of Nuclear Medicine* **43**, 510-518 (2002).

81. Vaupel, P., Kallinowski, F. & Okunieff, P. Blood flow, oxygen and nutrient supply, and metabolic microenvironment of human tumors: a review. *Cancer research* **49**, 6449-6465 (1989).

82. Picano, E. Risk of cancer from diagnostic X-rays. *Lancet* **363**, 1909-1910; author reply 1910 (2004).

83. Wall, B.F. & Hart, D. Revised radiation doses for typical X-ray examinations. Report on a recent review of doses to patients from medical X-ray examinations in the UK by NRPB. National Radiological Protection Board. *The British journal of radiology* **70**, 437-439 (1997).

84. Hall, E.J. & Brenner, D.J. Cancer risks from diagnostic radiology. *The British journal of radiology* **81**, 362-378 (2008).

85. Huang, B., Law, M.W. & Khong, P.L. Whole-body PET/CT scanning: estimation of radiation dose and cancer risk. *Radiology* **251**, 166-174 (2009).

86. Plathow, C. et al. [Cost considerations for whole-body MRI and PET/CT as part of oncologic staging]. *Der Radiologe* **48**, 384-396 (2008).

87. Rudmik, L. et al. Clinical utility of PET/CT in the evaluation of head and neck squamous cell carcinoma with an unknown primary: a prospective clinical trial. *Head & neck* **33**, 935-940 (2011).

88. Hellman, L.M., Duffus, G.M., Donald, I. & Sunden, B. Safety of diagnostic ultrasound in obstetrics. *Lancet* **1**, 1133-1134 (1970).

89. Reece, E.A., Assimakopoulos, E., Zheng, X.Z., Hagay, Z. & Hobbins, J.C. The safety of obstetric ultrasonography: concern for the fetus. *Obstetrics and gynecology* **76**, 139-146 (1990).

90. Duck, F.A. Physical Properties of Tissue. (Academic Press, London; 1990).

91. Goss, S.A., Frizzell, L.A. & Dunn, F. Ultrasonic absorption and attenuation in mammalian tissues. *Ultrasound in medicine & biology* **5**, 181-186 (1979).

92. D'Astous, F.T. & Foster, F.S. Frequency dependence of ultrasound attenuation and backscatter in breast tissue. *Ultrasound in medicine & biology* **12**, 795-808 (1986).

93. Plesset, M.S.P., A. Bubble Dynamics and Cavitation. *Ann. Rev. Fluid Mech.* **9**, 145-185 (1977).

94. Matula, T.J. & Roy, R.A. Comparisons of sonoluminescence from single-bubbles and cavitation fields: bridging the gap. *Ultrasonics sonochemistry* **4**, 61-64 (1997).

95. Neppiras, E.A. Acoustic Cavitation. *Physics Reports* **61**, 159-251 (1980).

96. Flint, E.B. & Suslick, K.S. The temperature of cavitation. *Science* **253**, 1397-1399 (1991).

97. Lohse, D. Sonoluminescence: cavitation hots up. *Nature* **434**, 33-34 (2005).

98. Gaitan, D.F. et al. Spectra of single-bubble sonoluminescence in water and glycerin-water mixtures. *Physical review. E, Statistical physics, plasmas, fluids, and related interdisciplinary topics* **54**, 525-528 (1996).

99. Riesz, P. & Kondo, T. Free radical formation induced by ultrasound and its biological implications. *Free radical biology & medicine* **13**, 247-270 (1992).

100. Pecha, R. & Gompf, B. Microimplosions: cavitation collapse and shock wave emission on a nanosecond time scale. *Physical review letters* **84**, 1328-1330 (2000).

101. Lifshitz, D.A. et al. Quantitation of shock wave cavitation damage in vitro. *Ultrasound in medicine & biology* **23**, 461-471 (1997).

102. Prat, F. et al. Hepatic lesions in the rabbit induced by acoustic cavitation. *Gastroenterology* **100**, 1345-1350 (1991).

103. Carstensen, E.L. et al. Lysis of erythrocytes by exposure to CW ultrasound. *Ultrasound in medicine & biology* **19**, 147-165 (1993).

104. Delius, M., Enders, G., Xuan, Z.R., Liebich, H.G. & Brendel, W. Biological effects of shock waves: kidney damage by shock waves in dogs--dose dependence. *Ultrasound in medicine & biology* **14**, 117-122 (1988).

105. Parsons, J.E., Cain, C.A., Abrams, G.D. & Fowlkes, J.B. Pulsed cavitational ultrasound therapy for controlled tissue homogenization. *Ultrasound in medicine & biology* **32**, 115-129 (2006).

106. Prabowo, F. & Ohl, C.D. Surface oscillation and jetting from surface attached acoustic driven bubbles. *Ultrasonics sonochemistry* **18**, 431-435 (2011).

107. Ohl, C.D. et al. Sonoporation from jetting cavitation bubbles. *Biophysical journal* **91**, 4285-4295 (2006).

108. Miller, D.L. & Gies, R.A. The interaction of ultrasonic heating and cavitation in vascular bioeffects on mouse intestine. *Ultrasound in medicine & biology* **24**, 123-128 (1998).

109. Holt, R.G. & Roy, R.A. Measurements of bubble-enhanced heating from focused, MHz-frequency ultrasound in a tissue-mimicking material. *Ultrasound in medicine & biology* **27**, 1399-1412 (2001).

110. Miller, D.L. & Song, J. Tumor growth reduction and DNA transfer by cavitation-enhanced high-intensity focused ultrasound in vivo. *Ultrasound in medicine & biology* **29**, 887-893 (2003).

111. Apfel, R.E. & Holland, C.K. Gauging the likelihood of cavitation from short-pulse, low-duty cycle diagnostic ultrasound. *Ultrasound in medicine & biology* **17**, 179-185 (1991).

112. Santin, M.D. et al. Encapsulated contrast microbubble radial oscillation associated with postexcitation pressure peaks. *The Journal of the Acoustical Society of America* **127**, 1156-1164 (2010).

Chapter 2:

A Novel Nested Liposome Drug Delivery Vehicle Capable of Ultrasound Triggered Release of its Payload

Abstract

The use of focused ultrasound can be an effective method to locally highlight tumor tissue and specifically trigger the activation of echogenic drug delivery vehicles in an effort to reduce systemic chemotherapy side effects. Here we demonstrate a unique ultrasound triggered vehicle design and fabrication method where the payload and a perfluorocarbon gas microbubble are both encapsulated within the internal aqueous space of a liposome. This nested lipid shell geometry both stabilized the microbubble and ensured it was spatially close enough to interact with the liposome membrane at all times. The internal microbubble was shown to fragment the outer liposome membrane upon exposure to ultrasound at intensities of 1 - 1.5 MPa. The focused ultrasound allowed the release of the internal payload to localized regions within tissue phantoms. The vehicles showed high payload loading efficiency of 16%, stability in blood of several hours, and low level macrophage recognition in vitro. High speed fluorescent videos present the first optical images of such vehicles interacting with ultrasound. This ability to open the outer membrane in small regions of deep tissue could provide a second level of spatial and temporal control beyond biochemical targeting, making these particles promising for in vivo animal studies.

2.1 Introduction

Indiscriminate exposure of all cells in the body to a systemically administered chemotherapy drug is the main cause of harmful toxic side effects[113]. Certain drug delivery vehicles such as Abraxane for delivery of paclitaxel and liposomal Doxil for doxorubicin[114, 115] reduce exposure of non-targeted cells to the drug while accumulating a therapeutic dose within the tumor. Passive accumulation in the tumor tissue due to the enhanced permeation and retention of the vasculature[114] coupled with slow drug release limits the bioavailability to non-tumor

organs[116]. However, this slow release also limits the maximum levels of drug in the tumor[117], and nonspecific accumulation in healthy tissue remains a major hurdle[114].

The use of tumor targeting ligands has the potential to improve the preferential accumulation of these delivery vehicles in tumor tissue [118, 119]. The delivery requires endocytosis of the targeted vehicle with subsequent endosomal escape[120, 121]. However, saturation of the targetable receptors limits the targeting efficiency. Also, tumor "receptors" are rarely unique to the tumor [122] and the targeted particles accumulate in other healthy tissues, especially in the liver and spleen, causing local toxicity [48].

To address the difficulties of pure biochemical targeting, an independent non-biochemical trigger is required to cause instantaneous drug release only from the particles that have accumulated in the tumor tissue. Ultrasound is an attractive trigger candidate due to its low cost, wide availability, its generation external to the body, and its independence from biochemical or physical properties of the tumor. It can be focused to small volumes of deep tissue on the order of several cubic millimeters[123] to avoid healthy tissue. It is non-ionizing, and does not damage tissue as long as the exposure is kept below 720 mW/cm^2 [124, 125].

The best particles to respond to ultrasound at safe exposure levels are gas-filled microbubbles[126] already approved for human use as ultrasound contrast agents [127, 128]. Ultrasound causes large size fluctuations in microbubbles due to the large density difference between the compressible gas and the surrounding water, which induces microstreaming of fluid around the microbubble and disrupts nearby membranes [129]. Microbubbles can also adiabatically implode (cavitate) producing a shockwave and water jets which can penetrate nearby membranes. This causes sonoporation and can facilitate delivery of DNA or drugs into cells[128, 130-132]. Significant work has been done to employ microbubbles as delivery vehicles in vivo [130, 132] without much success [133]. This is likely attributed to extremely short circulation times of microbubbles in vivo (3-15 min half-life [133]) and to limited payload capacity.

Surface loading of a hydrophilic payload, such as DNA, is limited by the surface area of the microbubble[134-137] and leaves it exposed to degradation and potential immune system recognition. Hydrophobic payloads are carried in limited volumes of thickened lipid, polymer, or oil surrounding the microbubble [136, 138] but when fragmented the hydrophobic drug will be contained in relatively large lipid particles reducing diffusion rates.

Drug loaded liposomes have been attached to the surface of microbubbles[139], however the points of attachment can concentrate shear stress during transport through the microvasculature and destabilize the entire particle. Separate drug-loaded liposomes and microbubbles can be targeted to the same tissue, but successful delivery of the drug depends on very close co-localization of both particles because the cavitation shockwave is only effective at disrupting membranes within a few tens of microns. It is unlikely that both particles would be present in sufficient proximity and concentration to deliver a therapeutic dose.

To protect the microbubble and address the challenges described above, the microbubble and the payload can be encapsulated together within a protective outer liposome membrane shell. Previous efforts to incorporate gas bubbles into liposomes have used freeze drying techniques[140] or chemical reactions that create CO_2 microbubbles[141], but have very low yields. They also lack sufficient control over gas and payload entrapment, stability, and internal geometry, resulting in a large distribution of properties. Such distributions reduce the effectiveness of ultrasound to activate the entire population. Premade microbubbles stabilized with a lipid monolayer can be made independently using standard probe sonication techniques which increases bubble half-life in storage and *in vivo*. Microbubbles of desired size ranges can be collected and subsequently encapsulated in liposomes.

The most common methods of liposome encapsulation involve exposure to vacuum, sonication, heating, and/or extrusion, all of which destroy microbubbles. Ethanol injection is gentle enough to allow the microbubbles to survive the encapsulation process but produces

liposomes too small to encapsulate a microbubble[142]. Detergent dialysis methods[143] can make liposomes large enough to encapsulate microbubbles and are gentle enough to not destroy them in the process.

Here we demonstrate a new manufacturing method to reproducibly encapsulate and protect premade microbubbles in a liposome as shown schematically in Fig. 2.1a. This method is similar to detergent dialysis but uses organic solvents to dissolve the lipids. A slow diffusive introduction of water allows the lipid membranes to seal and encapsulate the large microbubbles. We refer to these malleable nested structures as SHockwavE-Ruptured nanoPayload cArriers (SHERPAs).

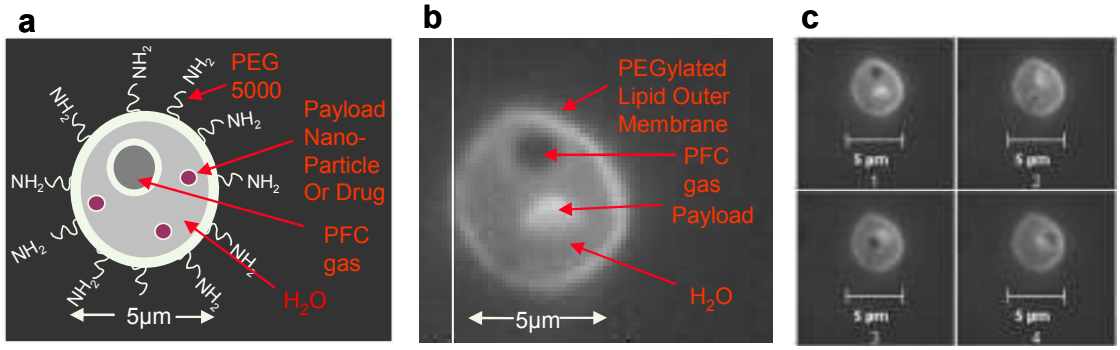

Figure 2.1 SHERPA nested structural design (a) A schematic of the nested liposome SHERPA design. (b) Fluorescent image of a SHERPA resulting from the described manufacturing process. The payload is a small fluorescently labeled lipid membrane. (c) A series of sequential pictures taken of the SHERPA showing the microbubble and fluorescent lipid payload moving around inside due to Brownian motion. This confirms that the microbubble and payload were internal to the outer membrane and not just attached to the outside.

2.2 Materials and Methods

2.2.1 Materials

L-α-phosphatidylcholine (EPC) from chicken eggs, distearoyl phosphatidylcholine (DSPC), distearoyl phosphatidylethanolamine-methyl poly(ethylene glycol) MW5000 (mPEG-DSPE), and cholesterol were purchased from Avanti Polar Lipids, Inc. (Alabaster, AL). 1,2-propanediol, glycerol, ethanol, and perfluorohexane were purchased from Sigma-Aldrich. All

water was purified using the Milli-Q Plus System (Millipore Corporation, Bedford, USA). DiO was purchased from Biotium, Inc. CA. The PBS was purchased from Hyclone Laboratories Inc. (Logan, UT).

2.2.2 SHERPA Production

2.2.2.1 Lipid Preparation

The SHERPAs were manufactured in a two step procedure with the microbubbles being formed through a probe sonication process and subsequently encapsulated in the outer liposome. The desired payload of nanoparticles or water soluble drug can be introduced in Solution 1, Solution 2, or in the PBS used for the final encapsulation step.

Solution 1: Outer Liposome Lipid Solution

A 1.5 mL eppendorf tube was filled with 76 µL of EPC in chloroform (26 mM)(20 mg mL^{-1}) and 10 µl of cholesterol in chloroform (100 mM)(387 mg mL^{-1}). The chloroform was removed by evaporation while vortexing under an argon stream. 125 µL of ethanol was then added and the solution was vortexed at 3200 rpm for 30 sec. To visualize lipid membranes, 5 µL of 1 mM DiO (Biotium, Hayward, CA) in ethanol was added.

Solution 2: Microbubble Solution

A 1.5 mL eppendorf tube was filled with 25 µL of DSPC in chloroform (51 mM) (40 mg mL^{-1}) and 20 µL mPEG5000-DSPE in chloroform (8.6 mM) (50 mg mL^{-1}). The chloroform was removed by evaporation while vortexing under an argon stream. Then 450 µL of 1,2-propanediol was added. The solution was vortexed at 3200 rpm for 30 sec, and then placed in a heating block at 60 °C.

After 10 minutes, the solution was vortexed at 3200 rpm for 10 sec, and 150 µL glycerol was added. The solution was gently vortexed for 30 sec, and then placed back into the 60 °C heating block. The heating, vortexing cycle was repeated until the glycerol was fully mixed in

and the solution was homogeneous. This solution was then transferred to a 4 ml glass vial with a narrow neck. The neck of the glass vial was covered with parafilm to create a barrier and prevent loss of PFH gas during the violent sonication process.

The headspace of the container was filled with perfluorohexane gas using the method shown in Fig. 2.2 at 25 °C. 0.5 ml of the PFH liquid was first drawn into a 5 ml syringe. The plunger was then pulled all the way to the back of the syringe leaving 4.5 ml of air space. The syringe was rotated to coat all the walls of the syringe with the PFH several times to encourage fast vaporization of the PFH into the air. The metal needle of the syringe was bent at 130° from vertical and the syringe held upright as shown in Fig. 2.2A. The needle of the syringe was then inserted through the parafilm barrier and 4 ml of PFH/air mixture inside the syringe was injected into the air space as seen in Fig 2.2B. Care was taken to not inject any liquid PFH into the vial. The air that was originally in the vial head space was forced out of the vial through the needle track hole made in the parafilm.

As shown in Fig. 2.2C the tip of the probe sonicator (Fisher Scientific Model 100 Sonic Membrane Disruptor) was then inserted through the parafilm and positioned 1 mm below the surface of the lipid solution. The sonication power used was 25 W for 20 seconds. The temperature of the solution began at 25 °C but increased to approximately 40 °C at the end of the soniction. This bubble solution was put immediately on ice.

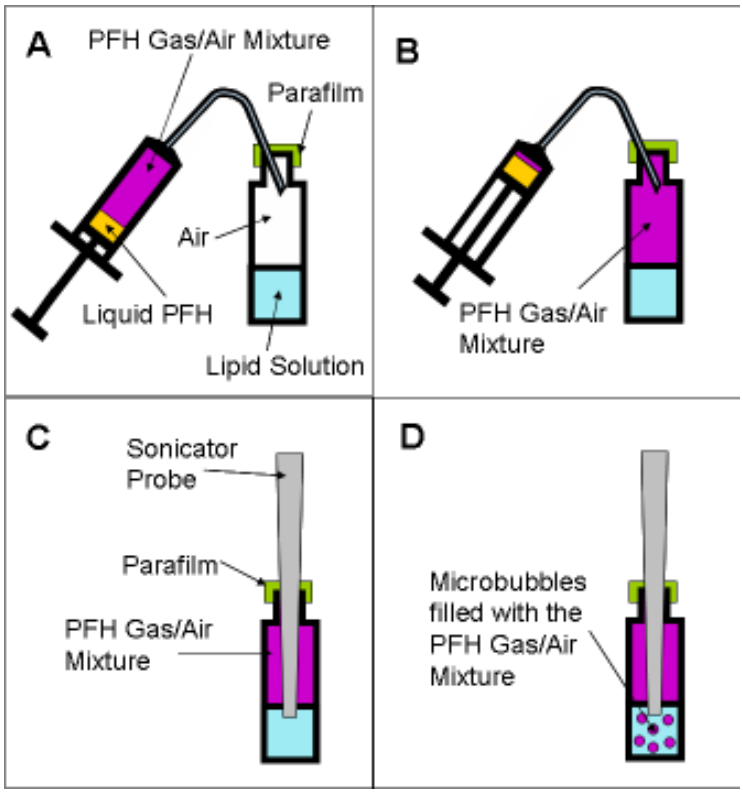

Figure 2.2 Schematic representation of the manufacturing process for the PFH/air mixture filled microbubbles. (a) A 5 ml syringe is filled with 0.5 ml of liquid PFH. The PFH is allowed to evaporate and mix with the air in the syringe until it reaches equilibrium. The top of the glass vial containing the lipid solution is covered with parafilm to reduce gas exchange from within the vial to the atmosphere (b) The PFH/air mixture is injected into the head space of the vial containing the lipid solution. Care is taken to prevent injection of any liquid PFH. The original air that was in the vial is displaced through the needle track hole made in the parafilm (c) The probe sonicator tip is inserted through the parafilm into the vial and the tip is positioned 1 mm below the surface of the lipid solution. (d) The probe sonicator is turned on and creates microbubbles which incorporate the PFH/air gas mixture in the headspace. These microbubbles are coated with the lipids from the solution.

2.2.2.2 Microbubble Encapsulation and SHERPA Formation

After allowing Solution 2 to cool to room temperature, Solution 1 was added drop wise to Solution 2 under vortex at 3200 rpm. This new solution was Solution 3.

1.5 mL Eppendorf tubes were each filled with 200 µL of Solution 3. 100 µL of PBS was gently added to the bottom of each tube to initiate the closing of the lipid sheets and formation of

the SHERPA. After 10 min, the tubes were rotated gently at an angle until the bubbles mixed thoroughly throughout the solution.

2.2.2.3 Microbubble Stability

Fig. 2.2D shows that once the sonication process began the only gas that could have been incorporated into the forming microbubbles was the PFH/air mixture. Control experiments showed greater long term stability for microbubbles made with the PFH gas and air mixture over those made with just pure air.

Allowing the PFH liquid to evaporate into the airspace of the syringe allowed the PFH gas to naturally come to equilibrium with the liquid PFH and the atmospheric gasses at atmospheric pressure. This process ensured that the PFH gas was present in a concentration that provided stability to the microbubble at atmospheric pressure and gas composition. Microbubbles made with no PFH would simply dissolve away and collapse. If the PFH gas concentration was too high then the PFH would recondense into a liquid droplet collapsing the microbubble. If the PFH gas concentration was too low then there would be a driving force for nitrogen to leave the microbubble and shrink its size to the collapse radius [144, 145].

For the purpose of these observational experiments the SHERPA were not stabilized with a PFH gas concentration against arterial pressure like the microbubbles used for ultrasound contrast imaging. The microbubbles described here were stabilized for atmospheric pressure and gas composition because these were the conditions they were exposed to while being tested in the ultrasound microscope setup. The microbubbles needed to be stabilized only against atmospheric pressure because the Laplace pressures on the microbubbles were greatly reduced due to the reduction of interfacial tension caused by the lipid coating [146]. For in vivo experiments the microbubble manufacturing process described here could be easily modified to have the same PFH mixture already developed to stabilize for in vivo pressure conditions [144].

2.2.2.4 Purification

The desired microbubble-containing liposomes were separated from the empty liposomes by gentle centrifugation. The positive buoyancy of the entrapped microbubbles caused the actual SHERPAs to rise to the top of the reaction solution allowing them to concentrate. A Beckman Coulter Allegra X-15R Centrifuge was used at 524 g. The purification was done in an inverted syringe inside a 50 ml tube oriented so the SHERPA would rise against the plunger. The subnatant, containing mostly empty liposomes, could be expressed and replaced with fresh solution to purify the SHERPAs as well as wash them from any unreacted materials or unencapsulated payloads.

2.2.3 Retention Time of Doxorubicin

A sample of doxorubicin-loaded SHERPAs (.37 mg/mL DOX) was prepared, by dissolving 0.4 mg of doxorubicin hydrochloride (Jinan Wedo Industrial Co., Ltd. Shandong Province, China) in the bubble solution. The sample was diluted 1:20 by volume in PBS to improve dialysis performance. One sample of SHERPAs without DOX was prepared to determine the background fluorescence, and one solution of just the equivalent solvents and DOX was used to determine the dialysis rate of DOX.

Each sample (250 μL) was dialyzed against 1 L PBS using Spectra/Por cellulose ester membrane tubing with a molecular weight cutoff of 1MDa. The 1 MDa pore size was chosen because it was much larger than the DOX molecule, allowing unrestricted diffusion across the membrane. The smallest liposomes manufactured were too large to pass through these membrane pores so all of the liposomes were retained. When measuring drug retention time it was crucial that the dialysis rate was much faster than the SHERPA leakage rate, so the DOX would not build up in the fluid surrounding the liposomes inside the dialysis tubing. For each measurement, the relative concentration of doxorubicin within the dialysis tubing was determined by measuring the

fluorescence with the TECAN Infinite 200 plate reader (Männedorf, Switzerland). The excitation and emission wavelengths were 475 and 595 nm respectively. The DOX-loaded SHERPA were analyzed at times 0, 0.5 hrs, 2 hrs, 6 hrs, and 24 hrs. For each time point, a separate sample was dialyzed.

2.2.4 Encapsulation Efficiency of IgG

To load the SHERPAs, mouse IgG was dissolved into the microbubble solution (solution 2) before the addition of water caused outer membrane sealing. A sandwich ELISA was used to assay the amount of free IgG. The background signal was determined by an identical sample with no IgG. For a positive control, IgG was added to the outside of this sample. Alternate liposomes were prepared by hydrating a lipid film with a solution containing IgG.

The difference between the sample and the positive control was taken to be the amount encapsulated. The percent encapsulation was calculated by dividing the difference by the background-adjusted positive control.

2.2.5 SHERPA characterization

2.2.5.1 Ultrasound microscope equipment

A custom system was developed to characterize the interaction of these SHERPAs with ultrasound. A water tank was used to couple the ultrasound to the SHERPA samples. Ultrasound was generated with a submersible Panametrics 2.25 MHz transducer (V305-Su, 1" spherical-focus) using a Panametrics BCU -58 - 6W waterproof connector cable. A needle hydrophone from Onda Corporation (HNP-0400 Broadband Needle Hydrophone AH - 2020-100 with hydrophone pre amp, 50kHz - 100 MHz, 0 +20 db.) was used to measure the sound field, and a Photron FASTCAM 1024 PCI acquired the image sequences. The National Instruments PCI 5412 arbitrary waveform generator was used to create different waveforms and was controlled using a

custom designed LabVIEW 8.2 program. A 300 W amplifier from Vox Technologies (model number VTC2057574) was used to create acoustic intensities at the focal region of up to 1.6 MPa.

The samples being analyzed were held in a custom fabricated microwell chamber comprised of a coverslip and a slab of Polydimethylsiloxane (PDMS) with a 15 μm-deep molded well. The microwell was placed halfway in the water, with the coverslip above the surface for fluorescent imaging with a Nikon 100X oil objective. The PDMS served as a coupling medium for the ultrasound between the water bath and the sample well.

2.2.5.2 Stability in blood

Blood was obtained from a healthy female mouse. All animal work was reviewed and approved by the Burnham Institute's Animal Research Committee. The sample was centrifuged to isolate the erythrocytes, which were then recombined with the remaining serum. 80μL of this sample was added to 20μL of SHERPAs and gently mixed. The SHERPA outer membrane integrity was inspected for stability by fluorescent microscopy 2, 30, and 120 minutes after the addition of blood.

2.2.5.3 Phagocyte uptake experiments

2.2.5.3.1 Macrophage Culture

J774A.1 mouse macrophages were purchased from American Type Culture Collection (ATCC) Manassas, VA, USA. Cells were cultured in a 75 cm^2 flask with DMEM containing 10% Fetal Bovine Serum, glutamate and penicillin-streptomycin antibiotics (all purchased from Gibco, Invitrogen, Carlsbad, CA). SHERPAs and fluorescent beads (FluoSpheres, Invitrogen, Carlsbad, CA) were incubated with the macrophages for 1 hr.

2.2.5.3.2 Dendritic Cell Culture

Peripheral Blood Mononuclear Cells (PBMCs) were isolated from the blood of normal volunteers (San Diego Blood Bank) over a Ficoll-Hypaque (Amersham Biosciences, Uppsala, Sweden) density gradient. To generate dendritic cells (DCs), PBMCs were allowed to adhere to culture plates for 1h. The non-adherent cells were washed off and the adherent cells were cultured in RPMI 1640 medium supplemented with 2 mM L-glutamine (GIBCO-BRL Life Technologies; Grand Island, NY, USA), 50 mM 2-mercaptoethanol (Sigma, St. Louis, MO, USA), 10 mM HEPES (GIBCO-BRL), penicillin (100 U/mL),streptomycin (100mg/mL) (GIBCO-BRL) and 5% human AB serum (Gemini Bio Products West Sacramento, CA, USA), supplemented with 1000 U GM-CSF/mL (Cardinal Health, Dublin, OH, USA) and 200U IL-4/mL (R&D Systems, Minneapolis, MN) at days 0, 2, and 4. Immature DCs were harvested on days 5-7. These N178 human dendritic cells were incubated with SHERPAs for 1 hr, and FITC-dextran (IVGND1845, Invitrogen, Carlsbad, CA) was used as a positive control. Results were analyzed with FACS using the FACSCalibur system (BD Biosciences, San Jose, CA) and fluorescence microscopy.

2.3 Results

2.3.1 SHERPA Structure

The dialysis-based manufacturing process described above produced the desired SHERPA structure consisting of a nested 5 μm liposome containing a 1 μm microbubble as shown schematically in Fig. 2.1a and with fluorescence microscopy in Fig. 2.1b. The Brownian motion of the microbubble and payload of the SHERPA was contained entirely within the outer membrane as shown in a series of sequential pictures in Fig. 2.1c. These structures were observed to be stable for several days.

2.3.2 SHERPA Production

2.3.2.1 Microbubble Formation

The probe sonication of the heated glycerol and 1,2-propanediol mixture containing dissolved DSPC and mPEG5000-DSPE successfully created microbubbles coated with a stabilizing lipid monolayer. This increased their resistance to the subsequent introduction of ethanol. DSPC was chosen because its long saturated tails result in a high T_c of 55 ºC. The brush layer created by the mPEG5000-DSPE helped increase SHERPA stability by preventing microbubbles from merging with each other and the outer liposome membrane. Perfluorohexane was chosen as the gas due to its established biocompatibility and low water solubility which increased the microbubble stability[137]. The high viscosity environment of the glycerol and 1,2-propanediol increased the concentration of microbubbles (~10^8/mL) by reducing their direct physical contact until they reached a more stable state.

2.3.2.2 Microbubble Encapsulation

The addition of the ethanol solution containing the egg PC lipid, cholesterol, and the lipophilic dye DiO to the microbubble solution drop wise under high vortex created lipid structures that intermixed with the microbubbles as shown in Fig. 2.3a. These structures appear to be unclosed lipid sheets whose free ends were stable under these solvent conditions. The viscosity of the solvent was important because it slowed the diffusion of added water into the region of these lipid sheets, making their free ends slowly unstable over several minutes. The increasing instability of the free ends caused the sheets to seal with themselves and neighboring sheets encapsulating the intervening microbubbles to form SHERPAs as shown in Fig. 2.3b. Fig. 2.3c shows a magnified view with several SHERPAs present. Egg PC was chosen because its very low transition temperature (T_c) of -15 ºC increased the flexibility and fluidity of the outer membrane, allowing the lipid sheets to seal. The flexibility could also help increase particle circulation time

by allowing easier passage through the microvasculature. The cholesterol amount was optimized to increase stability of the outer liposome and improve drug retention time. Some of the mPEG5000-DSPE from the microbubble solution was also incorporated into the outer membrane. This was demonstrated by preventing charge interactions between SHERPAs doped with positively charged DOTAP lipid and cell surfaces. SHERPAs that were doped with DOTAP but did not have mPEG5000-DSPE attached readily to the surface of HUVEC cells. This indicates that the external surface of the SHERPAs were PEGylated and able to maintain a steric separation from the cells. This property is crucial to prolonging in vivo circulation time.

The large microbubbles shown in Fig. 2.3a disappeared in Fig. 2.3b and 2.3c because the added water made the solution less viscous. The larger bubbles floated quickly to the top, where they aggregated and destabilized. The 1-2 μm diameter microbubbles of choice rose more slowly and were much more stable when exposed to increasing concentrations of water in the formation process.

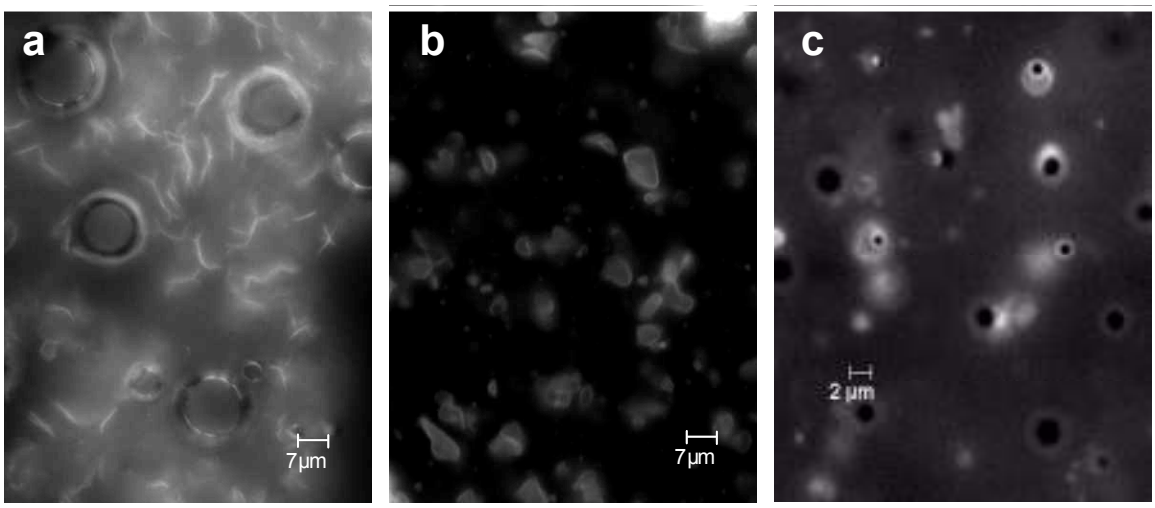

Figure 2.3 SHERPA formation. (a) The fluorescently labeled lipid structures mixed with the microbubbles shown before the final water addition step during SHERPA formation. The lipid structures appear to be open sheets whose free ends are stable under these mixed solvent conditions of glycerol, 1,2-propanediol, and ethanol. (b) After addition of water to the microbubble and ethanol mixture shown in Fig. 2.3a, the open free ends of the lipid sheets become energetically unstable and they seal with themselves and with the free ends of surrounding sheets encapsulating the intervening microbubbles. This magnification level is the same as in Fig. 2.3a. (c) This shows a close up of the SHERPAs just after formation.

2.3.3 Encapsulation and Retention Time of Doxorubicin

One fundamental property of a drug delivery vehicle is its ability to contain its payload while in transit. The outer lipid membrane sheets of the SHERPA which close around the microbubble must seal to encapsulate a drug such as doxorubicin (DOX). DOX is currently dose limited by its cardiotoxic side effects, especially when administered systemically in free form[147-149]. DOX can be incorporated into the SHERPAs by its addition to the bubble solution, or to the water during the final formation step. The concentration of the DOX inside the SHERPA is the same as the concentration of the drug in these preparation solutions because this solution is encapsulated within the SHERPA along with the microbubbles. The SHERPA can be loaded with higher concentrations of DOX by using higher concentrations in the preparation solutions.

The encapsulation of DOX is shown in Fig. 2.4a. The retention time of free DOX was determined by dialyzing DOX-loaded SHERPAs against PBS, and measuring the DOX

concentration over time from the fluid within the dialysis tubing. For passively loaded DOX, the release followed an exponential decay with tight correlation. The retention half-life was 4.74 hours, and is in good agreement with the literature for other liposomes loaded with free DOX [150]. In the future, the retention time of DOX can be increased 10 times or more from this value by inducing the DOX to form crystals inside the liposomes by using proper pH gradients [150].

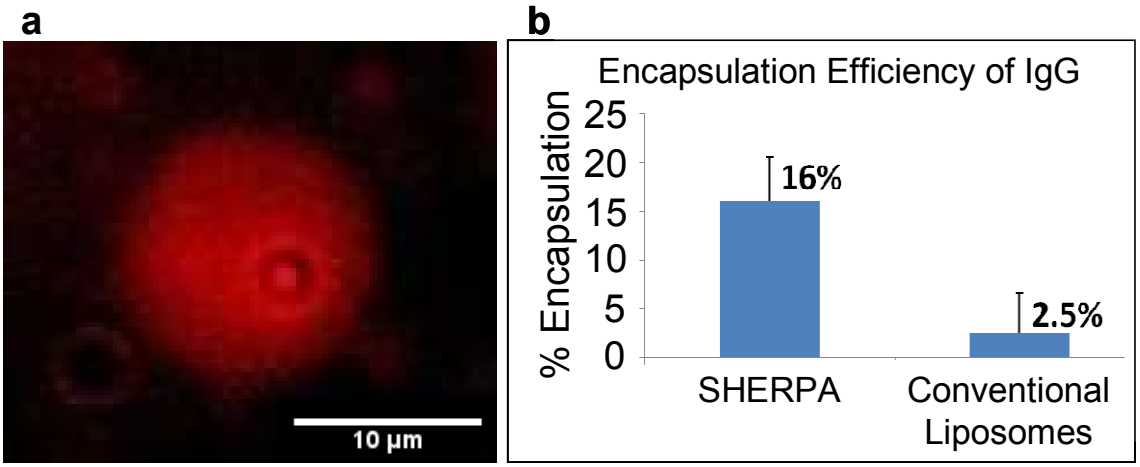

Figure 2.4 SHERPA payload loading. (a) Demonstration of doxorubicin loading. Red fluorescence from entrapped doxorubicin can be seen as a diffuse sphere. This liposome also contains a microbubble shown by the dark inner circle. (b) Efficient loading of a macromolecule, IgG, was demonstrated and quantified using ELISA. Other liposomes were prepared by standard methods for comparison.

2.3.4 Encapsulation Efficiency of Microbubbles and Biomolecules

To evaluate the encapsulation efficiency of the SHERPA, mouse IgG was used as a model large biomolecule payload. An ELISA was performed to calculate the percent loading of IgG (150 kD, ~5 nm) into the SHERPAs. The samples were added directly to capture antibodies after formation, to minimize experimental error. Only free IgG was accessible to bind capture antibodies and contributed to the ELISA signal. The mean percentage of the entire volume of the preparation solution that was encapsulated within the SHERPA outer liposome was 16%. This was high for passive entrapment and much higher than the 2.5% measured for the liposomes

prepared by thin film hydration [151] as shown in Fig. 2.4b. This is likely due to the larger size of the SHERPA liposomes and the fact that the lipids sheets are well suspended with the payload before sealing.

The encapsulation efficiency of the microbubbles into the SHERPA outer liposomes was lower (1-5%) because the IgG was small enough to fit into any sized SHERPA but the microbubbles were on the micron size and could only fit into the larger liposomes. However, these microbubble-containing SHERPAs were easily separated from the empty liposomes by buoyancy driven methods, since the microbubble inside reduces the overall density of the SHERPA compared to empty liposomes and bulk solution.

2.3.5 SHERPA Interaction with Ultrasound

2.3.5.1 Ultrasound Intensity Level of 1.5 MPa

The custom built high speed ultrasound microscope setup described in the methods section was used to observe the interaction of the fluorescently labeled SHERPA with ultrasound. Cavitation of the internal microbubble was observed at ultrasound intensity levels of 1.5 MPa as shown in Fig. 2.5a. Here the microbubble underwent a violent implosion producing a shockwave that fragmented the fluorescent lipid outer membrane into a cloud of fine debris. It is important to note that an empty liposome was present right next to the SHERPA as shown in Fig. 2.5a frame 1. This empty liposome contained no microbubble and was exposed to the same ultrasound pulse that cavitated the SHERPA, but had no visible reaction or disruption of the membrane. This shows that the ultrasound exposures required to cavitate the microbubbles would not harm the membranes of cells even in the focal zone. This localized effect of the cavitation on surrounding membranes illustrates the importance of the co-localization of the liposome and microbubble. A jet of debris material was also ejected from the site of cavitation as seen in frame 3 of the sequence. Fluid ejection is a well documented mode of microbubble cavitation[152].

2.3.5.2 Ultrasound Intensity Levels Below 1 MPa

A second mode of interaction between SHERPAs and ultrasound at levels below 1 MPa was observed in which the microbubble did not undergo cavitation, but instead had a less violent response. The size modulation of the bubble initiated an opening and unfolding of the SHERPA outer membrane as shown in Fig. 2.5b, probably due in part to microstreaming[152]. These free ends made the open membrane an unstable high energy structure.

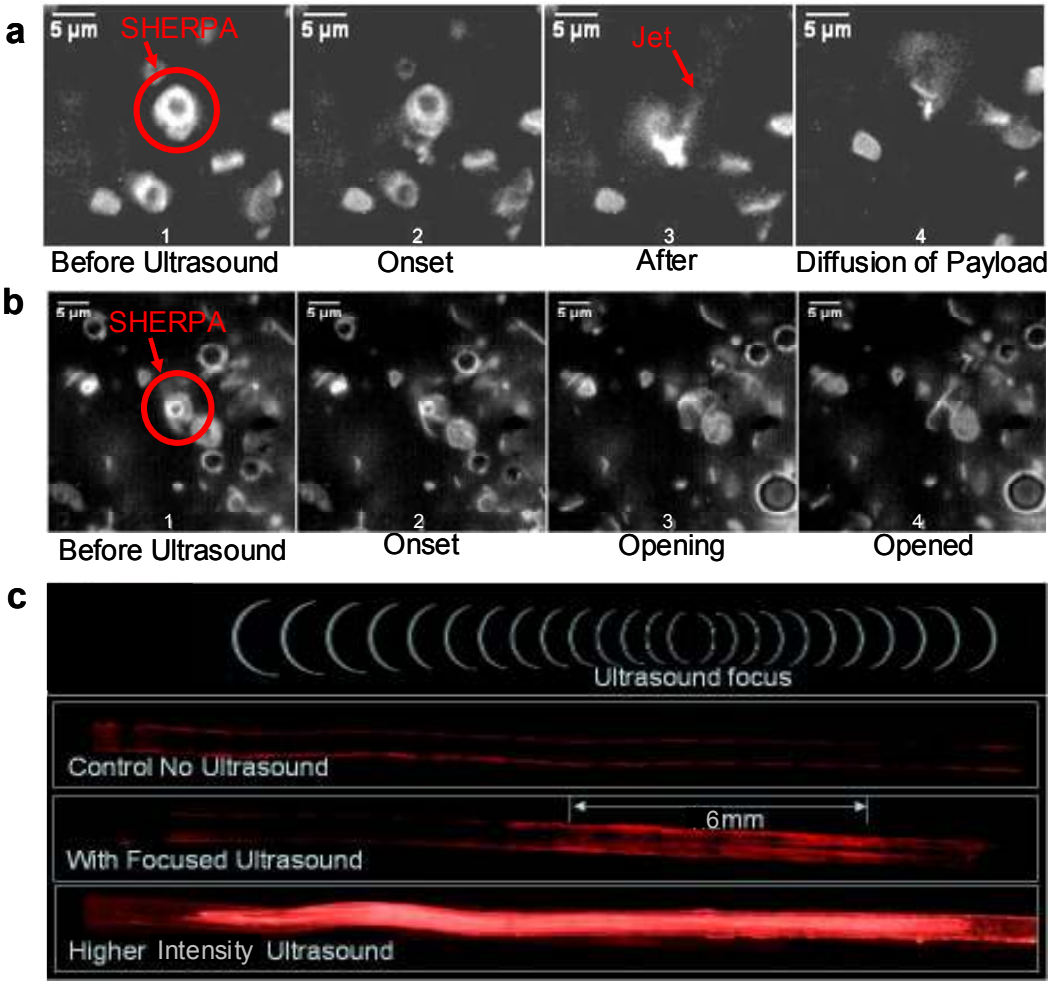

Figure 2.5 Interaction of SHERPA with Ultrasound. (a) Sequence of images showing a cavitation mode of ultrasound interaction with a SHERPA. Frame 1 shows the SHERPA before ultrasound exposure. Frame 2 shows the very onset of ultrasound exposure. Frame 3 shows the results just after the microbubble cavitation event creating a cloud of fluorescent debris. A jet of material has shot out from the main debris cloud. Frame 4 shows the diffusion of the membrane fragments 1.2 seconds after the cavitation event. (b) Sequence of images showing a popping type mode of SHERPA interaction with ultrasound. Frame 1 shows the SHERPA with its fluorescent outer membrane before exposure to ultrasound. Frame 2 shows the very onset of ultrasound exposure. Frame 3 shows the SHERPA membrane popping open on the lower right hand side and beginning to open up. Frame 4 shows the SHERPA fully opened up. (c) Images of ultrasound activation of SHERPA in simulated blood vessel channel within an agar block. The channel was coated with avidin and the SHERPA were functionalized with biotin. The biotin on the outside of the SHERPA was blocked with free avidin The control showed very little nonspecific binding of the fluorescently labeled SHERPA to the surface of the channel. Insonification with focused ultrasound ruptured SHERPA in the focal region allowing the biotin on the inside to bind to the surface of the channel. Higher intensity focused ultrasound created more activation and widened the range of SHERPA rupture causing larger deposition.

2.3.5.3. Localized SHERPA Activation

The localized activation of SHERPA only near the focal region of the ultrasound was demonstrated in an agar tissue phantom using a biotin/avidin binding scheme. An agar gel was prepared with a 1 mm diameter channel molded through the center to simulate a blood vessel which was coated with avidin. SHERPAs were made with DSPE-PEG2000-Biotin so the biotin was present on both the inner and outer surface of the SHERPA outer membrane. Biotins on the outside of the SHERPA were blocked by incubation with an excess of free avidin. The outer membrane was stained with DiO for visualization and the SHERPAs were introduced into the channel. The agar blocks were then insonified with focused ultrasound of various intensities. The control agar block showed very little nonspecific binding of the SHERPA to the walls of the channel after being washed with water as shown in Fig. 2.5c. Low intensity ultrasound ruptured the SHERPA only in the focal region, creating fluorescent membrane fragments with exposed free biotin that was originally on the inner leaflet of the SHERPA membrane. These fragments were then able to bind to the avidin coated walls of the channel allowing them to remain on the channel surface after it was flushed with water. Higher intensity ultrasound ruptured a larger number of SHERPA resulting in a higher fluorescent signal as well as creating a larger region of activation.

2.3.6 SHERPA Stability in Biological Fluids

SHERPA stability was evaluated by dilution into a blood sample followed by fluorescent microscopy. Intact SHERPAs were observed for up to two hours. Brownian motion caused the SHERPAs to interact with the surrounding red blood cells (RBCs), demonstrating their membrane flexibility. Much like the cells, they appeared to change their shape to pack closely with neighboring groups of RBCs a shown in Fig. 2.6a. The flexibility can potentially help reduce

uptake from the spleen by mimicking the ability of RBCs to squeeze through the filtration system. No attachment or clotting induction of the SHERPAs on the RBCs was observed.

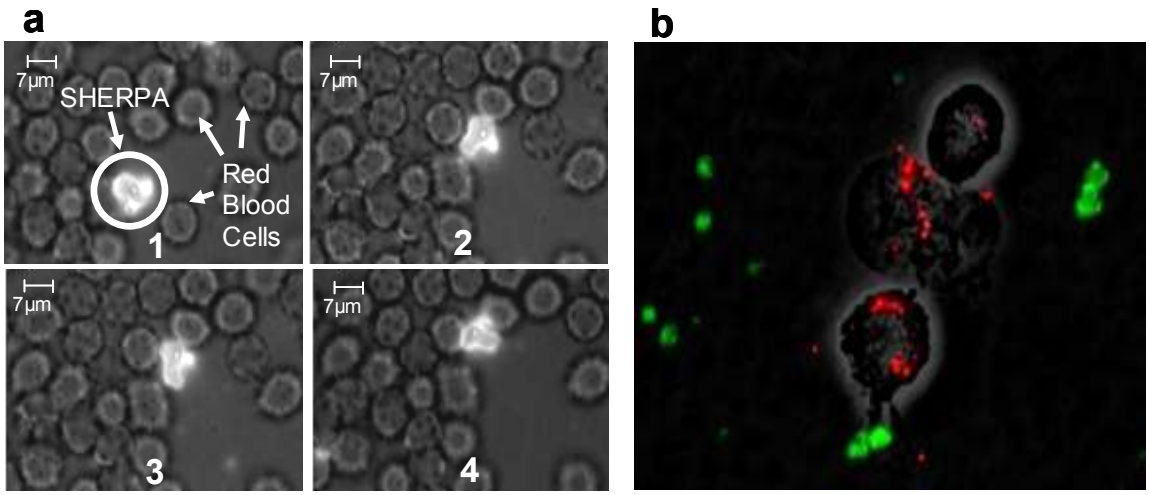

Figure 2.6 SHERPA in vitro behavior. (a) SHERPA interaction with red blood cells. The outer membrane of the SHERPA is very flexible and allows it to change shape so as to achieve close packing with surrounding red blood cells as shown through this sequence of pictures. The only driving force for this is Brownian motion. (b) Three J774 macrophages have engulfed nearly all the fluospheres (red). No liposomes (green) can be seen inside the macrophages.

2.3.7 Macrophage Uptake of SHERPA

An effective drug carrier must be able avoid clearance by phagocytes for a sufficient period of time to reach its target. This nested design has a smooth PEG coated outer surface which presents less of a target for the immune system. J774 mouse macrophages were used to model the uptake of particles and liposomes fabricated by our method. SHERPA membranes were labeled green, and red Fluosphere beads were used as a positive control to show that the incubation solution did not inhibit the function of the macrophage. After 1 hr of incubation, macrophages were inspected by fluorescence microscopy. Fig. 2.6b shows strong macrophage uptake of red Fluospheres with no visible phagocytosis of SHERPAs.

SHERPAs were also incubated with N178 human dendritic cells and analyzed by FACS and fluorescence microscopy. The FITC-dextran control was contained within 96.9% of cells,

whereas only 3.49% of cells contained fluorescently labeled SHERPAs. Scatter data showed no evidence of cell death. This indicates the possibility that the SHERPAs will have a low clearance rate from the immune system.

2.3.8 In Vivo Circulation and Biodistribution

To test the in vivo behavior of the SHERPA, a mouse was injected i.v. with a sample, and blood was sampled periodically in order to estimate the circulation half-life. Organs were frozen and sectioned (Fig. 2.7a) to look at the retention of liposomes and/or membrane fragments which were labeled with a red fluorescent lipophilic dye. Uptake is dominant in the spleen, and other uptake can be seen in the liver. The lack of red fluorescence in the other samples indicates a low level of uptake. The blood clearance of the SHERPA liposomes had an excellent fit to an exponential curve. When extrapolated, the clearance half-life was calculated to be 91 minutes.

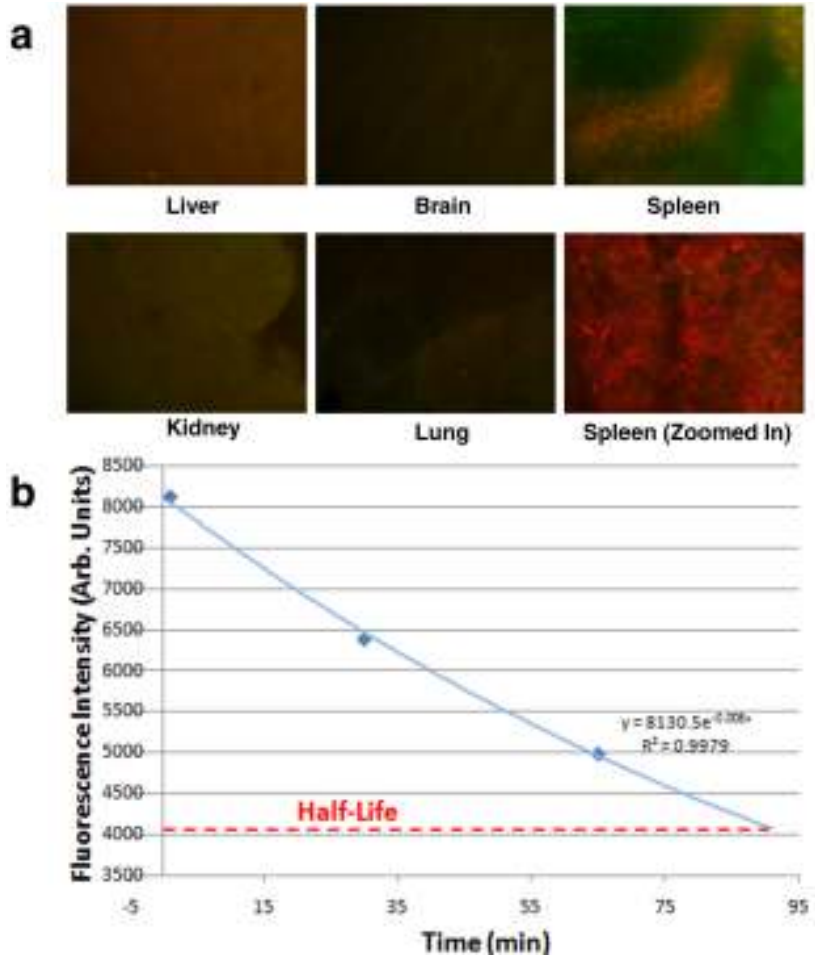

Figure 2.7 SHERPA in vivo biodistribution and circulation. SHERPA were labeled with DiI in order to track their fate and blood clearance. (a) Tissue sections show relative accumulation of the SHERPA in various key organs. The liver and especially spleen showed a high level of accumulation. (b) SHERPA blood clearance was determined by measuring fluorescence intensity from blood samples taken at different time points. Extrapolation of the exponential fit suggests a blood clearance half-life of 91 minutes.

2.4 Discussion

The SHERPA nested geometry has several attractive features as a drug delivery vehicle. The smooth continuous outer liposome with its PEG coating protects the internal microbubble and payload from degradation, reduces immune system recognition, and creates far greater loading capacity than microbubbles alone. The surface-to-volume ratio is far less than that of nanoliposomes which allows higher surface densities of targeting ligands to be used to increase

targeting efficiency without the risk of receptor saturation. The materials used in the construction of SHERPAs are bioresorbable and the perfluorocarbon gas can be cleared through exhalation.

The SHERPA are intended for intravenous injection which allows the SHERPA and the payload to penetrate every region of the tumor where the vasculature reaches, as opposed to an intratumoral injection where the SHERPA would be limited in their mobility from the injection site. The flexibility of the outer membrane can mimic the flexibility of red blood cell membranes and could help to increase circulation time of the SHERPA by allowing easier passage through the microvasculature. The SHERPA drug delivery vehicles themselves are not meant to extravasate from circulation into the tumor tissue. The main role of the SHERPA is to bring a highly concentrated payload into the tumor region through the vasculature. The payloads consisting of therapeutic nanoparticles or drug molecules are capable of extravasation once released from the SHERPA, especially inside the tumor region due to the "leaky" vasculature. The release of payload from the SHERPA located in the vasculature of the tumor will expose both the endothelial cells and the tumor tissue itself to the payload. Future work will explore the circulation time of these particles and the effect of focused ultrasound on payload delivery from the circulating particles to selected tissue regions.

The nested SHERPA structure always keeps the microbubble, large payload, and cell membrane in close proximity, increasing the chance for sonoporation[153] which is initiated by the cavitation event. Simultaneous pore formation in the cell membrane and release of high concentrations of payload in the same region could allow payload to travel down its concentration gradient into the cells, bypassing the need for endocytosis, and endosomal escape. With the resolution of focused ultrasound on the order of several cubic millimeters, SHERPAs residing in surrounding healthy tissue will be unaffected. They will break down gradually, diluting their payloads into the blood stream, making cellular delivery much less effective, and preventing accumulation of the drug[153]. This sonoporation effect may also occur during non-cavitation

microbubble interactions from the microstreaming of fluid around the microbubble[152]. Transient holes formed in the cell surface can be on the order of 100 nm in diameter and allow for payload uptake to occur over several minutes[154].

2.5 Conclusions

Here we have demonstrated a process for consistent production of liposomes containing stabilized microbubbles. Though the overall structure is new, the outer liposome is amenable to standard functionalization and modifications well documented in the literature. These can increase their preferential accumulation in tumor sites to achieve maximum SHERPA concentration at the moment when the region is selectively insonified with ultrasound. This allows for both spatial and temporal control over activation with a burst release of a highly concentrated payload making these particles promising for in vivo studies.

The present structure is able to circulate in the bloodstream of a mouse, and the liposomes mostly end up in the spleen. Certain in vivo delivery applications may require a longer circulation time to maximize the chance that the SHERPA will pass through the region of interest before being cleared from the circulation. Scaling down the particle size may enable a longer circulation by preventing size-dependent splenic filtration.

2.6 Acknowledgements

This chapter contains materials from Ibsen, Stuart; Benchimol, Michael; Simberg, Dmitri; Schutt, Carolyn; Steiner, Jason; Esener, Sadik. “A novel nested liposome drug delivery vehicle capable of ultrasound triggered release of its payload”, Journal of Controlled Release, vol. 155, 2011.

2.7 References

113. Shapiro, C. & Recht, A. Side Effects of Adjuvant Treatment of Breast Cancer. *The New England journal of medicine* **344**, 1997 - 2008 (2001).

114. Gabizon, A.A. Pegylated Liposomal Doxorubicin: Metamorphosis of an Old Drug into a New Form of Chemotherapy. *Cancer Investigation* **19**, 424-436 (2001).

115. Miele, E., Spinelli, G.P., Miele, E., Tomao, F. & Tomao, S. Albumin-bound formulation of paclitaxel (Abraxane® ABI-007) in the treatment of breast cancer. *International journal of nanomedicine* **4**, 99–105 (2009).

116. Gabizon, A., Shmeeda, H. & Barenholz, Y. Pharmacokinetics of pegylated liposomal Doxorubicin: review of animal and human studies. *Clin Pharmacokinet* **42**, 419-436 (2003).

117. Cheong, I. et al. A bacterial protein enhances the release and efficacy of liposomal cancer drugs. *Science* **314**, 1308-1311 (2006).

118. Karmali, P.P. et al. Targeting of albumin-embedded paclitaxel nanoparticles to tumors. *Nanomedicine : nanotechnology, biology, and medicine* **5**, 73-82 (2009).

119. Murphy, E.A. et al. Nanoparticle-mediated drug delivery to tumor vasculature suppresses metastasis. *Proceedings of the National Academy of Sciences of the United States of America* **105**, 9343-9348 (2008).

120. Allen, T. Ligand-Targeted Therapeutics in Anticancer Therapy. *Nature Reviews Cancer* **2**, 750-763 (2002).

121. Ulrich, A.S. Biophysical Aspects of Using Liposomes as Delivery Vehicles. *Bioscience Reports* **22**, 129-150 (2002).

122. Park, J. et al. Anti-HER2 Immunoliposomes: Enhanced Efficacy Attributable to Targeted Delivery. *Clinical Cancer Research* **8**, 1172–1181 (2002).

123. Zanelli, C.I., DeMarta, S., Hennige, C.W. & Kadri, M.M. Beamforming for Therapy with High Intensity Focused Ultrasound (HIFU) Using Quantitative Schlieren. *IEEE Ultrasonics Symposium*, 1233-1238 (1993).

124. Wojcik, G. et al. Nonlinear Modeling of Therapeutic Ultrasound. *1995 IEEE Ultrasonics Symposium Proceedings*, 1617-1622 (1995).

125. Barnett, S. et al. International Recommendations and Guidelines for the Safe Use of Diagnostic Ultrasound in Medicine. *Ultrasound in Medicine and Biology* **26**, 355-366 (2000).

126. Stride, E. & Saffari, N. Microbubble ultrasound contrast agents: a review. *Proc. Instn Mech. Engrs Part H: J. Engineering in Medicine* **217**, 429-447 (2003).

127. de Jong, N., Bouakaz, A. & Frinking, P. Basic acoustic properties of microbubbles. *Echocardiography* **19**, 229-240 (2002).

128. Von Bibra, H. et al. Interaction of Microbubbles with Ultrasound. *Echocardiography* **16**, 733-741 (1999).

129. Katherine Ferrara, R.P., Mark Borden Ultrasound Microbubble Contrast Agents: Fundamentals and Application to Gene and Drug Delivery. *Annu. Rev. Biomed. Eng* **9**, 415-447 (2007).

130. Gao, Z., Kennedy, A.M., Christensen, D.A. & Rapoport, N.Y. Drug-loaded nano/microbubbles for combining ultrasonography and targeted chemotherapy. *Ultrasonics* (2007).

131. Sun, Y., Zhao, S., Dayton, P.A. & Ferrara, K.W. Observation of contrast agent response to chirp insonation with a simultaneous optical-acoustical system. *IEEE Trans Ultrason Ferroelectr Freq Control* **53**, 1130-1137 (2006).

132. Zhao, Y.Z. & Lu, C.T. [Recent advances in the applications of ultrasonic microbubbles as gene delivery systems]. *Yao Xue Xue Bao* **42**, 127-131 (2007).

133. Willmann, J.K. et al. Targeted microbubbles for imaging tumor angiogenesis: assessment of whole-body biodistribution with dynamic micro-PET in mice. *Radiology* **249**, 212-219 (2008).

134. Kheirolomoom, A. et al. Acoustically-active microbubbles conjugated to liposomes: characterization of a proposed drug delivery vehicle. *Journal of controlled release : official journal of the Controlled Release Society* **118**, 275-284 (2007).

135. Klibanov, A. Microbubble Contrast Agents Targeted Ultrasound Imaging and Ultrasound Assisted Drug-Delivery Applications. *Investigative Radiology* **41**, 354-362 (2006).

136. Liu, Y., Miyoshi, H. & Nakamura, M. Encapsulated ultrasound microbubbles: Therapeutic application in drug/gene delivery. *Journal of Controlled Release* **114**, 89–99 (2006).

137. Lentacker, I. et al. Ultrasound-Responsive Polymer-Coated Microbubbles That Bind and Protect DNA. *Langmuir* **22**, 7273-7278 (2006).

138. Unger, E., McCreery, T., Sweitzer, R., Caldwell, V. & Wu, Y. Acoustically Active Lipospheres Containing Paclitaxel: A New Therapeutic Ultrasound Contrast Agent. *Investigative Radiolog* **33**, 886-892 (1998).

139. Kheirolomoom A., D., P., Lum, A., Little, E., Paoli, E., Zheng, H., Ferrara, K. Acoustically-active microbubbles conjugated to liposomes: Characterization of a proposed drug delivery vehicle. *Journal of Controlled Release* **118**, 275–284 (2007).

140. Huang, S. & MacDonald, R. Acoustically active liposomes for drug encapsulation and ultrasound-triggered release. *Biochemica et Biophysica Acta* **1665**, 134- 141 (2004).

141. Liu, R. et al. The preparation and characterization of gas bubble containing liposomes. *Proceedings of the 2005 IEEE Engineering in Medicine and Biology 27th Annual Conference Shanghai, China* (2005).

142. Domazou, A. & Luisi, P. Size Distribution of Spontaneously Formed Liposomes by the Alcohol Injection Method. *Journal of Liposome Research* **12**, 205-220 (2002).

143. Hosaka, Y., Semba, T. & Fukai, K. Artificial Assembly of Envelope Particles of HVJ (Sendai Virus). Fusion Activity of Envelope Particles. *J Gen Virol* **25**, 391-404 (1974).

144. Schutt, E., Pelura, T. & Hopkins, R. Osmotically-stabilized microbubble ultrasound contrast agents. *Acad Radiol* **3**, S188–S190 (1996).

145. Schutt, E., Klein, D., Mattrey, R. & Riess, J. Injectable Microbubbles as Contrast Agents for Diagnostic Ultrasound Imaging: The Key Role of Perfluorochemicals. *Angew. Chem. Int. Ed.* **42**, 3218 – 3235 (2003).

146. Borden, M.A., Pu, G., Runner, G.J. & Longo, M.L. Surface phase behavior and microstructure of lipid/PEG-emulsifier monolayer-coated microbubbles. *Colloids and Surfaces B: Biointerfaces* **35**, 209–223 (2004).

147. Singal, P.K. & Iliskovic, N. Doxorubicin-Induced Cardiomyopathy. *The New England journal of medicine* **339**, 900-905 (1998).

148. Olson RD, M.P. Doxorubicin cardiotoxicity: analysis of prevailing hypotheses. *FASEB J.* **4**, 3076-3086 (1990).

149. Minotti, G., Menna, P., Salvatorelli, E., Cairo, G. & Gianni, L. Anthracyclines: Molecular Advances and Pharmacologic Developments in Antitumor Activity and Cardiotoxicity. *Pharmacological reviews* **56**, 185–229 (2004).

150. Mayer, L.D., Bally, M.B. & Cullis, P.R. Strategies for Optimizing Liposomal Doxorubicin. *Journal of Liposome Research* **1**, 463-480 (1990).

151. Berger, N., Sachse, A., Bender, J., Schubert, R. & Brandl, M. Filter extrusion of liposomes using different devices: comparison of liposome size, encapsulation efficiency, and process characteristics. *International journal of pharmaceutics* **223**, 55-68 (2001).

152. Young, F. Cavitation (Imperial College Press London; 1999).

153. Ohl, C.-D. et al. Sonoporation from Jetting Cavitation Bubbles. *Biophysical journal* **91**, 4285–4295 (2006).

154. Zarnitsyn, V., Rostad, C. & Prausnitz, M. Modeling Transmembrane Transport through Cell Membrane Wounds Created by Acoustic Cavitation. *Biophysical journal* **95**, 4124-4138 (2008).

Chapter 3:

An Ultrasound-Ruptured Liposome Using Nanoparticle Cavitation Nucleation Sites

Abstract

Externally-triggered delivery of therapeutics provides a compelling means to control drug release profiles and localize exposure. Previously developed delivery vehicles have used microbubbles or phase-shifting emulsions as the foundation for an ultrasound-sensitive carrier. Here we demonstrate a liposome structure whose exterior is similar to clinically used liposomal formulations, but with an interior containing components for ultrasound sensitivity. Stable nanoparticle nucleation sites for acoustic cavitation were incorporated to reduce the intensity of ultrasound needed to rupture the membrane and cause payload release. High-speed fluorescence microscopy showed the efficient fragmentation of liposomes and release of calcein restricted to the ultrasound focal region. Release was quantified for different nucleation sites as a function of peak negative pressure. The dependence of release on particle size and core material indicates a presence of multiple nucleation mechanisms. This novel liposome has the structure, biocompatibility, and functional versatility necessary to be an effective delivery platform for cancer and other local diseases.

3.1 Introduction

The advent of nanomedicine has promised to bring new therapeutic delivery systems capable of improved precision and external control. Ultrasound (US) has been looked at as a means to achieve this external control, due to its deep penetration, low scattering through tissue, and its non-ionizing nature which results in minimal secondary effects[155]. In addition, the ability to focus ultrasound waves offers spatial specificity needed to fight local diseases like many cancers. The body's weak interaction with US waves accounts for its safety, but the lack of inherent contrast presents a challenge in discriminating tissues. To overcome this, particles can be engineered to have this sensitivity that the body lacks.

Gas-filled microparticles known as microbubbles (MB) have excellent acoustic responsiveness, or echogenicity, which explains their long clinical history as the main contrast agent for diagnostic ultrasound[156]. Their intrinsic property of concentrating acoustic energy through resonance has enabled the direct addressing of specific deep tissues, remotely. The destructive nature of a MB collapsing under pressure has encouraged much research into therapeutic applications including drug delivery[157]. One approach has been to facilitate diffusion of a payload into cells by sonoporation, a consequence of nearby MB cavitation[158]. The resulting transient holes in cell membranes allow rapid diffusion of a payload into the cytoplasm and passage of macromolecules like nucleic acids which are too large and polar to cross the cell membrane under normal circumstances[159].

Other approaches have ensured colocalization of the payload and MB by attaching the desired payload to the MB shell. The payload can be conjugated to a stabilizing monolayer or hidden in a thickened shell of lipids or polymer[160, 161]. The payload can also be contained in liposomes attached to the bubble surface[162], or the MB can be encapsulated inside of a liposome[163, 164]. In addition to increasing the likelihood of the payload to enter a cell, focused ultrasound activation can also enable control over the biodistribution of a drug by altering its pharmacokinetics[165]. The loaded shell of a MB, normally too large to leave the vascular space[166], can be fragmented into small nanoparticles capable of extravasation and being endocytosed or individual molecules which can cross the cell membrane[167, 168]. The high concentration gradient of payload generated at the US focus can increase the chance of the payload to interact with the local environment and diffuse into nearby cells.

MBs can be ruptured at low ultrasound pressures, including FDA-approved formulations used in routine US imaging[169]. While the MB has excellent sensitivity, stability is the main limitation for in vivo efficacy. Commercial MB formulations can have long shelf-lives, but the blood circulation half-life is typically less than 10 minutes[170, 171]. Inert and minimally soluble

perfluorocarbon (PFC) gases are often used to minimize reactivity and dissolution. Still, MBs have difficulty retaining their gas while passing through the lung, and the fate of the shell materials is often the liver and spleen[172, 173]. This is adequate for imaging applications, but for localized delivery of a therapeutic, long circulation is critical to ensure that a significant amount of material passes through the target region and off-target toxicity is minimized[174, 175].

Compared to MBs described in the previous chapter, PFC nanoemulsions have better pharmacokinetics, owing to their stable liquid state and smaller size. This allows significantly longer circulation than MBs and the potential to extravasate and accumulate passively in tumors via the enhanced permeation and retention (EPR) effect[176, 177]. Phase-shifting nanoemulsions combine these benefits with the excellent contrast enhancement of MBs. The rarefaction from US causes a liquid droplet to convert to the gaseous state in a process called acoustic droplet vaporization (ADV)[178-180]. Since the insolubility of liquid PFCs prevents the incorporation of virtually all compounds without modification, the surface is again utilized to contain a payload[181, 182]. The lack of an aqueous compartment to contain a freely dissolved payload means that at best the shell can be fragmented into small nanoparticles to increase the surface and enhance extravasation. The property of slow degradation which is desirable for a long-circulating carrier conflicts with the need for the nanoparticles to release their contents once they have reached their destination.

If we were able to impart ultrasound-sensitivity to a carrier containing an aqueous compartment, we could create a powerful delivery platform for freely dissolved payloads which could diffuse across cell membranes immediately following their release. This vehicle would also have the versatility to carry other biomolecules which are most stable in polar solvents. To accomplish this, we have developed a new ultrasound-sensitive liposome which operates without the need for MBs or low-boiling-point liquid PFCs. Instead, we use pressure- and temperature-stable nanoparticles which act as nucleation sites for acoustic cavitation. This enables cavitation

to be induced with lower US intensities than those which cause cavitation in bulk tissue[183]. In addition, the high loading capacity interior of the liposome can contain free solute which allows the rapid release of individual molecules, a function not possible in the shell-loaded geometries. The development of this vehicle will create for the first time an ultrasound-triggered delivery platform capable of carrying and releasing a broad array of therapeutic payloads.

3.2 Results and Discussion

Non-gaseous nanoparticles can also act as nucleation sites for acoustic cavitation of water and PFC emulsions[184-187]. In addition to the aforementioned ADV mechanism, the surface tension and cohesive force between liquid molecules is modulated at the surface of the particles and allows for efficient seeding of a gas cavity[188]. The extent to which a particle will exhibit this effect is determined by surface geometry, hydrophobicity, and the entrapment of gas pockets in hydrophobic crevices.

In this work, we investigated the use of high boiling point PFC nanoemulsions as cavitation nucleation sites for liposome disruption. These molecules are only stable in the liquid state at physiological and room temperatures and cannot undergo conversion into a stable gas bubble like other lower boiling point PFCs used in ADV. The use of higher boiling point PFCs is beneficial due to their slowed elimination and reduced bio-effects such as pulmonary gas trapping[189, 190]. These adverse effects are likely to become more pronounced as emulsion size decreases, due to increasing surface-to-volume ratio, accelerating dissolution. Increasing Laplace pressure can also result in a higher degree of blood saturation, though these effects can be limited with the use of surfactants to reduce the surface tension.

In addition to having a strong effect of reducing cavitation threshold, the consistent production of these nanoemulsions made it easy to compare different liquid cores. It was possible to produce emulsion solutions at up to 40 vol% PFC, which resulted in droplet concentrations

near 10^{16} ml^{-1}, orders of magnitude higher than most commercially available nanoparticles. This ensured the greatest possible number of nanodroplets encapsulated in each liposome.

3.2.1 High Boiling-Point PFC Droplets as Cavitation Nucleation Sites

Though the nanoemulsions used throughout this study were too small to image in real-time, the source of their nucleation effect is believed to be based on previously proposed mechanisms. One potential mode by which PFC nanoemulsions nucleate cavitation is a transient ADV from the internal volume instead of a surface nucleation of water cavitation. This concept was demonstrated by real-time observations of the US response of perfluorononane (PFN) droplets acquired at 45,000 fps as shown in Figure 3.1b. Micron scale droplets were produced in order to be clearly visible under an optical microscope. When insonated with US, cavitation nucleated from the PFN droplet, as seen in frame 2. Immediately after, a gas MB is clearly visible within the liquid volume of the droplet. In the following 62 ms, the MB condenses or dissolves back into the PFN droplet until it is no longer visible. This effect was repeatable through many cycles, in contrast with droplets of lower boiling point PFCs, which can convert into MBs which persist for minutes[191].

This MB persistence time is important for repeatedly pulsed US, where the transient microbubble could efficiently nucleate further cavitation at even lower intensities. One cavitation event is capable of initiating a chain reaction, rapidly producing a cluster of bubbles and broadening the observed region of cavitation[**192**]. This may explain the observation of decreased cavitation thresholds for longer pulse lengths, since a short pulse may not be long enough to create a chain reaction[193].

While persistent MBs are ideal for contrast-enhanced US, the short lifespan of transient MBs is enough for them to also serve as spatial indicators by increasing backscatter[194, 195]. Additionally, the generation of these MBs produces a broadband acoustic emission which can be

imaged with arrays of passive cavitation detectors[196]. Thus, the described particles coupled with the appropriate imaging system could enable an image-guided delivery system. The bubble produced in Figure 3.1b is assumed to originate from the PFN and not the surrounding water, judging from its affinity for the interior of the droplet. Higher frame-rate videos may provide more information as to the exact cavitation mechanism. It has been shown that the pressure required to induce ADV increases with decreasing droplet diameter[197]. Since the large size of these emulsion droplets would likely facilitate ADV, further experiments have been conducted to demonstrate the ability of nanodroplets to also be efficient cavitation nucleation sites.

Table 3.1 Perfluorocarbon Properties[198]

Molecule Name	Chemical Formula	Chemical Structure	Molecular Weight (Daltons)	Boiling Point (ºC)
Perfluoroheptane	C_7F_{16}	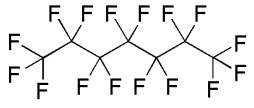	388.05	82
Perfluorooctane	C_8F_{18}	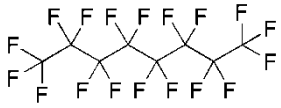	438.06	104
Perfluorononane	C_9F_{20}	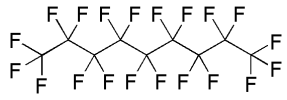	488.07	119
Perfluorodecalin	$C_{10}F_{18}$	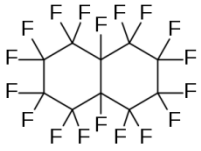	462.08	140

If transient ADV does not account for the decreased cavitation threshold, the nucleation property of the nanodroplets may be due to surface nucleation of water cavitation (Fig. 3.1a Left Panel). The sharp curvature of surfactant molecules around an emulsion droplet can create substantial disorder of the surrounding water. Additionally, if US were able to temporarily displace surfactant molecules, the extremely hydrophobic PFC core, now exposed to water, could then serve as an efficient nucleation site. The shear forces resulting from cavitation could cause such a destabilization of the emulsion shell which could rapidly "activate" droplets in the vicinity by exposing their PFC core (Fig. 3.1a Right Panel). Thus, a rare cavitation event, which might otherwise completely subside in between ultrasound pulses could instead have a cascading effect in the presence of nucleation sites.

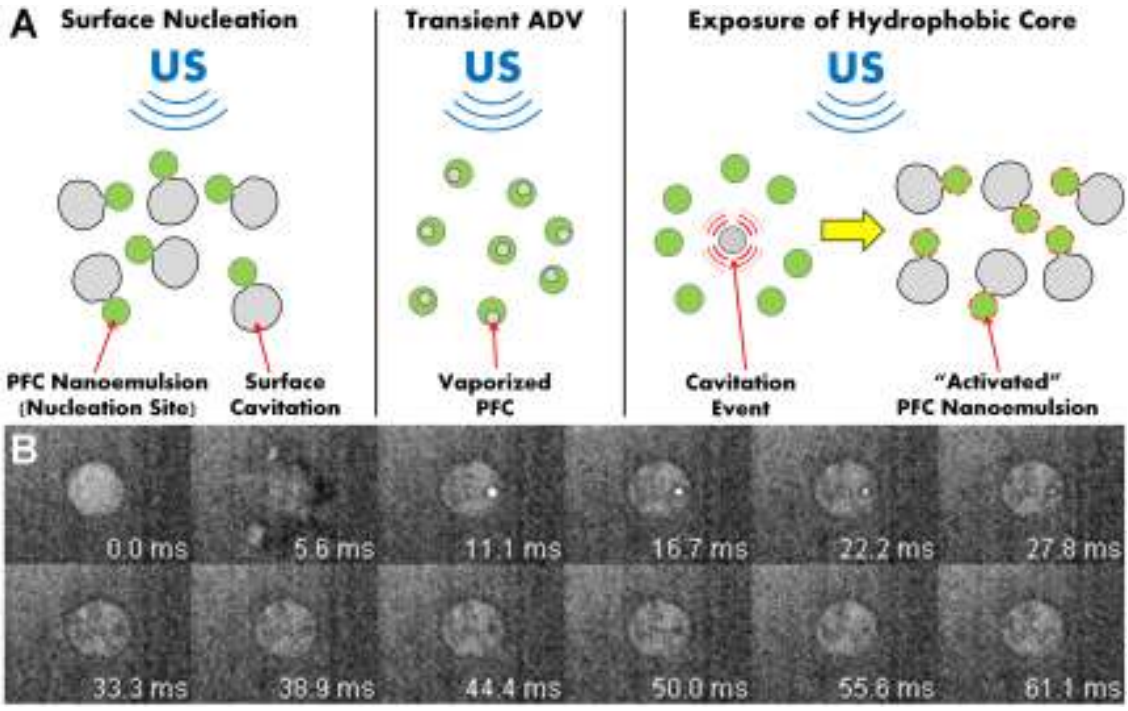

Figure 3.1 Cavitation nucleation by high boiling point perfluorocarbon (PFC) nanoemulsion droplets. a) Possible nucleation mechanisms. In the left panel**,** cavitation is nucleated at the interface of the droplet surface and the surrounding water due to modulation of the surface tension. In the middle frame, transient acoustic droplet vaporization (ADV) causes the production of a bubble which rapidly regresses into the liquid PFC core. In the right frame, an initiating cavitation event disturbs the surfactant layer of the droplets, temporarily exposing the hydrophobic PFC core. By this mechanism, one rare cavitation event could produce many active nuclei. In all 3 cases, the gas cavities can also efficiently nucleate further cavitation. b) High speed observation of cavitation nucleating from a perfluorononane emulsion. The first frame shows the emulsion before application of ultrasound. An ultrasound pulse occurs during frame 2, which shows a violent cavitation event resulting in the production of a gas bubble seen in frame 3. Subsequent frames show the gradual condensation or dissolution of the vapor bubble into the emulsion droplet until the bubble is no longer visible, and the emulsion again appears as it did in frame 1. Because the emulsion reverts to its original state, this process was repeatable over many ultrasound pulses. Images were recorded at 45,000 fps and downsampled for better illustration. The shutter speed was 1/303,000 s.

3.2.2 Fabrication of Liposomes Containing Perfluorocarbon Nanoemulsions

Generating the desired structure required a liposome fabrication technique capable of efficient incorporation of nanoparticles. One technique which was tested was to generate semi-stable lipid sheets which would close upon the addition of an aqueous buffer. Such a technique

was recently used to form liposomes encapsulating microbubbles[163]. While this technique was able to encapsulate nanoemulsions, a large majority of the emulsions were not encapsulated, and the organic solvents involved precluded the incorporation of most biomolecules which would precipitate in their presence. Instead, we used a modification of reverse-phase evaporation (REV), a technique which templates the formation of liposomes onto aqueous emulsion droplets. REV, originally developed in the 1970's[199], is capable of producing liposomes with high encapsulation efficiencies, and is compatible with the encapsulation of proteins, nucleic acids, and other biomolecules due to the minimal exchange of the immiscible solvents[199]. By altering which solvent is used, a broad selection of polar molecules can be encapsulated. To achieve efficient incorporation, the encapsulant should be more soluble in the aqueous phase to prevent extraction into the organic phase. Nonpolar molecules can be encapsulated into nanoparticles, which can then be incorporated into the liposomes after the addition of a hydrophilic passivation layer. Such is the case for the PFC emulsions used here, which without the appropriate surfactant would be extracted into the organic phase. Emulsion size was reduced as much as possible, so as not to limit the overall size of the URL. Nanoemulsions were stabilized by a PFC-PEG block copolymer, which granted a very low surface tension, and allowed for the production of 20 nm emulsions. Additionally, the minimal droplet size resulted in a very high particle concentration, and high surface area to maximize surface effects. The PFC emulsions produced here are some of the smallest yet reported, and the size was very consistent from batch to batch and had little dependence on the specific PFC which was used for the core.

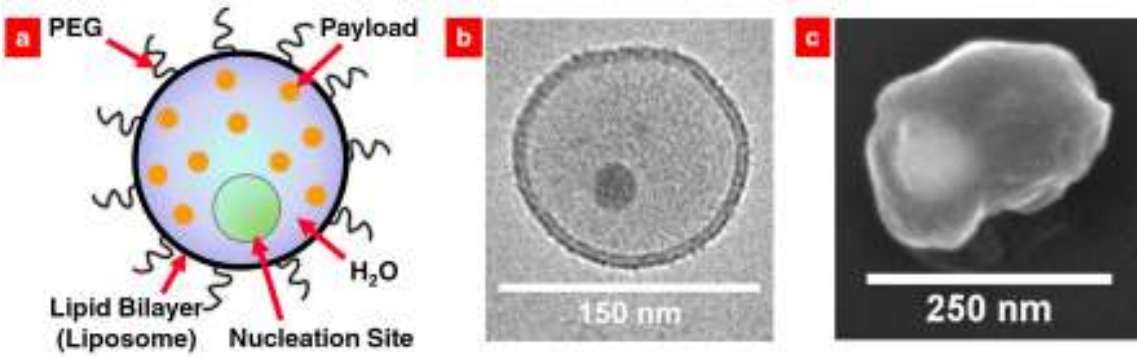

Figure 3.2 The Ultrasound-Ruptured Liposome (URL). a) Schematic of the described vehicle. The incorporation of a nucleation site for acoustic cavitation renders the liposome responsive to ultrasound**.** b) Cryo-transmission electron micrograph of a 140 nm liposome containing a 30 nm perfluorononane emulsion. c) Scanning electron micrograph of a liposome containing one gold nanoparticle (bright sphere). This structure demonstrates that fabrication by reverse-phase evaporation/extrusion can produce liposomes as small as 250nm containing nucleation sites as large as 90nm.

3.2.3 Electron Microscopy Imaging of Ultrasound-Ruptured Liposomes

Cryo-transmission electron microscopy confirmed the URL structure of 100-400 nm liposomes containing 15-30 nm PFN droplets (Figure 3.3d). The liposome and emulsion structure, preserved by the imaging method, clearly displays efficient encapsulation of a highly concentrated emulsion. Reconstructed tomograms showed the spatial distribution of PFN droplets and verified their volumetric encapsulation as opposed to surface adherence. Due to extrusion, liposomes were mostly unilamellar and some multilamellar (Fig 3.3c). Imaging of the PFN emulsion alone (Figure 3.3d) showed the occasional presence of larger (30-60 nm) droplets which were not observed in the liposome samples.

The increased size of the liposomes relative to free emulsions allowed for separation by centrifugation despite the higher density of the perfluorocarbon. However, the higher density of liposomes containing encapsulated PFN (ρ_{PFN} = 1.799 g/ml) allowed the URL to be pelleted at lower speeds than empty liposomes, although some empty liposomes were still observed. In the URL sample for which the free emulsions were not removed (Figure 3.3b), the encapsulated

emulsions were on average larger than the free emulsions. This could be a result of the liposome restriction, preventing dilution of the emulsion, thereby accelerating droplet coalescence.

Scanning electron microscopy verified the efficient encapsulation of 90-100 nm gold nanoparticles inside liposomes (Fig. 3.2c). Numerous images also confirmed the efficacy of the removal of free nanoparticles by dialysis with a .2 μm polycarbonate membrane. Greater than 99% of the observed gold nanoparticles were entrapped.

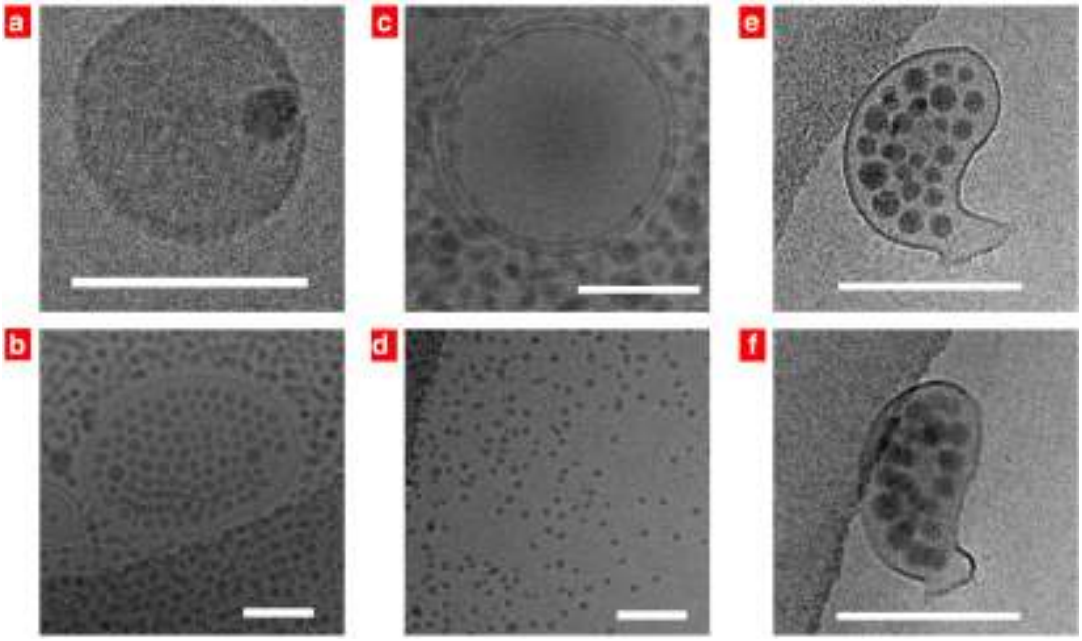

Figure 3.3 Cryo-TEM of ultrasound-ruptured liposomes (URL) containing perfluorononane (PFN) emulsion droplets. a) 100nm URL from a sample purified by dialysis and centrifugation. b) URL which have been dialyzed to remove trace solvents, but not purified by centrifugation. Although most of the droplets are originally encapsulated inside liposomes, after extrusion the inner and outer droplet concentration appears to be comparable. c) A sample of empty liposomes also fabricated by reverse-phase evaporation (REV) and mixed with PFN emulsions. The emulsion droplets are unable to penetrate the lipid membrane. d) The PFN emulsion before liposome processing. Most of the droplets were on the 15-20 nm size range. e,f) A liposome from the purified sample viewed at 2 different tilt angles. The acquired tilt sequence demonstrates the concentrated of droplets are contained within the liposome volume as opposed to positioned on the membrane surface. The scale bar in all images represents 100 nm.

3.2.4 Ultrasound-Triggered Membrane Fragmentation

Giant URL (2-5 μm) were fabricated in order to observe liposomal membrane fragmentation upon exposure to focused ultrasound. The lipid bilayers stained with DiO were clearly visible under high magnification in a fluorescent microscope. For the submerged geometry, a 60X water dipping objective with a working distance of 2 mm was used for a cleaner sound field. To acquire higher frame-rate videos and slightly higher resolution, a 100X oil immersion objective was used which had a higher numerical aperture. Real-time observation of the URL response to focused US was possible with the use of a combined US-optical microscope system described elsewhere[204]. In immediate response to the applied US, the glowing membranes shattered into sub-micron fragments as shown in Figure 3.4a. With liposomes containing no nucleation sites, the rupture threshold was significantly higher, and below the threshold only jolting or translation of liposomes was observed (Fig. 3.4b).

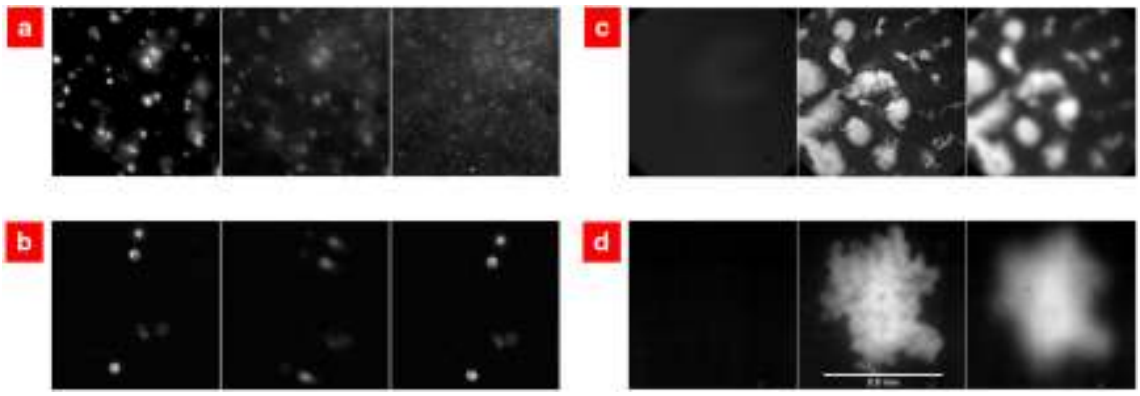

Figure 3.4 Real-time observation of focused ultrasound liposome rupture with high speed fluorescent microscopy. a,b) Giant (2-5 μm) liposomes were prepared with fluorescently labeled membranes to show the fragmentation of the lipid structures. Ultrasound-ruptured liposomes (URL) shown in (a) were fragmented with 1000 cycles of 2.25 MHz US (1.3 MPa), whereas normal liposomes (b) did not respond to the same settings. Only a "jolting" motion is visible due to a vibrational response of the sample holder. c,d) Release and dequenching of calcein dye contained in nanoliposomes. The first frame is dark due to efficient quenching of the dye, highly concentrated in the liposomes. The 2nd frame in which the US pulse occurs shows nearly instantaneous release and dilution of the dye, resulting in bright regions. The final frame shows the rapid diffusion of the small molecule dye. c) Bright plumes, presumably occurring near cavitation events, can be seen in high resolution images, at the expense of a reflecting sound field which produces hexagonal acoustic interference. d) In a cleaner sound field completely submerged, there is no observed acoustic interference, and the release is restricted to the focal region of the US, which is approximately 1 mm at this frequency.

3.2.5 Ultrasound-Triggered Calcein Release

To demonstrate ultrasound-triggered release of a hydrophilic small molecule payload, the self-quenching dye calcein was used. This showed the destruction of much smaller nanoliposomes which would be expected to function better in vivo. Liposomes encapsulating the dye and nanoparticles were extruded, and free dye and nanoparticles were removed by dialysis. The extruded liposomes had a mean diameter of 500 nm and a polydispersity index of 0.21 as measured by dynamic light scattering. US-induced cavitation ruptured the liposomes, releasing the calcein and rapidly mixing it with the surrounding liquid. The nearly instantaneous dilution of the dye caused the calcein to be less quenched and the fluorescence intensity to increase by more than 10-fold in some cases. Thus, the fluorescence intensity was an indicator for payload release

and more generally failing of the lipid bilayer. Though calcein is an appropriate model for small molecules, it is possible that the release characteristics will be dependent on size and hydrophobicity and is thus a topic of future work.

At an ultrasound pressure slightly above the cavitation threshold, the resulting fluorescent spot was confined to a sub-millimeter focal region (Fig 3.4c). Calcein release was also observed at the air/water interface, which allowed for higher resolution imaging of the kinetics, at the cost of a less characterized sound field. Figure 3.4d clearly shows bright regions where cavitation nucleated and streamlines where microstreaming caused shearing of the sub-micron liposomes or mixing of the released dye. Acoustic interference in the sample caused cavitation to nucleate in discrete spots, creating bright plumes throughout the focal region. The smaller fishtail streaks are presumed to be caused from secondary cavitation nucleated by projected MBs.

The required ultrasound pressure to release the calcein was recorded for each type of nanoparticle loaded inside of the liposomes and the control sample which contained no additional nanoparticles. In the submerged geometry, the control never showed any calcein release from the 10 ms continuous burst of 2.25 MHz US at the maximum pressure of 1.6 MPa. At the same US settings, liposomes loaded with perfluorononane nanoemulsions and Au nanoparticles nucleated cavitation, causing release of the calcein. There was a sharp pressure threshold centered at 1.3 MPa below which cavitation was never observed. For perfluorononane emulsions, the measured threshold at the air/water interface was slightly lower (1.1 MPa), due to regions of constructive interference in the sample. Since microscopy allows us to observe very isolated cavitation events and generate a cumulative fluorescence signal, the measured threshold is likely to be lower than those measured by many acoustic methods.

3.2.6 Quantification of Ultrasound-Triggered Calcein Release

The efficiency of calcein release in a bulk liposome solution was quantified by fluorescence intensity. Since particle size and concentration can affect the threshold and amount of cavitation[200, 201], these parameters must be well controlled to allow a direct comparison of different particle cores. For this reason URLs containing calcein and equal concentrations of either perfluoroheptane, perfluorooctane, perfluorononane, or perfluorodecalin emulsions were prepared. Pulsed US was applied from a 3.3 MHz focused transducer onto the sample for 1 minute in order to induce liposome rupture. The sample was diluted 100-fold to mimic dilution into the bloodstream. The fluorescence intensity of aliquots was taken as a measure of total release, when compared with an untreated and fully lysed sample. The encapsulation of PFC nanoemulsions was able to reduce the US intensity needed to cause release of the calcein. A 1000-cycle sine wave pulse was applied and repeated at a 1 or 10% duty cycle (Figure 3.5a) (Pulse repetition frequency 33 or 330 Hz) for 1 to 5 minutes. For URL containing perfluorononane nanoemulsions at 3.3 MHz, there was greater than 40% release at a peak-negative pressure (PNP) of 2.3 MPa.

A sharp rupture threshold of the URL was observed at a PNP near 2 MPa. At a PNP of 2.3 and 2.9 MPa, liposomes containing PFC nanoemulsions released 30-50% of their calcein, whereas the liposomes containing no nanoparticles showed less than 5% release until a PNP of greater than 3 MPa. Thus, at a PNP of 2.3 MPa, cavitation could be produced and URLs were ruptured with great selectivity over conventional liposomes, about 30-fold when Perfluorononane was used. The choice of PFC had little effect on the rupture threshold, which is evidence that for these formulations, the mechanism of cavitation nucleation is more dependent on the particle size and structure than the core material.

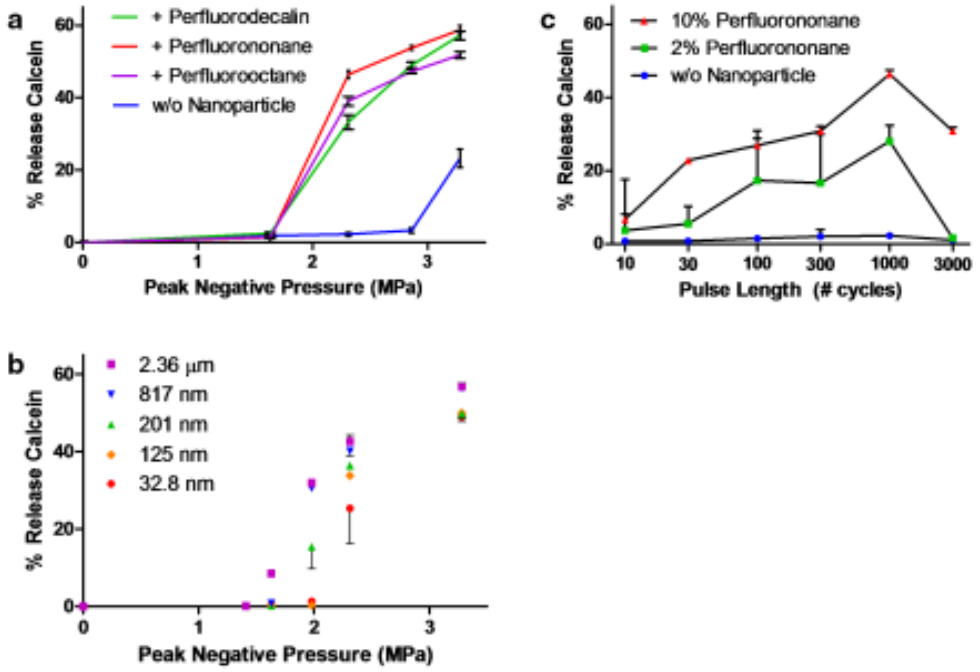

Figure 3.5 Quantification of payload release from URL containing self-quenched calcein. Using a fluorescence plate reader, release of calcein was measured as a function of nucleation site **a)** composition and **b)** size and of **c)** pulse length. a) Liposomes were prepared containing 4 different perfluorocarbon emulsions (10% v/v). A sharp threshold was observed between a peak negative pressure (PNP) of 1.6 and 2.3 MPa, where there was a 20-fold increase in calcein release. For the control liposomes containing no nucleation sites, the threshold occurred between a PNP of 2.9 and 3.3 MPa. b) The observed release threshold decreased with increasing droplet size, an effect which has been previously documented for ADV. For this experiment, droplets were not loaded into liposomes, but instead added to the outside to neglect a confounding effect of size-dependent loading efficiency.

To test the dependence of droplet size on cavitation nucleation, PFN emulsions of 5 different sizes were prepared. Encapsulation efficiency of emulsions inside liposomes is size-dependent, so emulsions were added to the outside of the liposomes to negate this effect. Since the concentration of PFN was held constant, emulsion samples with a larger mean diameter had a lower droplet concentration. ADV theory and experiments agree that conversion threshold decreases for increasing diameter, due to a reduction in surface tension and Laplace pressure. Smaller emulsion samples, however, have a higher particle concentration and a greater exposed surface area, thus surface effects should be most pronounced in these samples. Calcein release

was observed at a lower PNP for larger emulsion samples (Figure 3.5b), indicating a lower activation threshold. This result, which is seemingly evidence for an ADV-like mechanism, conflicts with the finding of a weak dependence of calcein release on PFC boiling point. This could be explained by the presence of both a transient ADV and a surface nucleation effect, where the ADV effect becomes insignificant for the smaller emulsions used in Figure 3.5a

While ADV and liposome rupture may be facilitated with the use of larger emulsions, for use in the URL, the encapsulating liposome size must be increased accordingly and could result in a liposome too large to have desirable in vivo circulation properties. To improve tumor specificity through EPR, the liposome size should be reduced to maximize leakage out of the vasculature. One mode of delivery may be to allow the URL to accumulate passively, and subsequently induce rupture with US to release their contents in the extracellular space. This could allow small molecules entrapped in liposomes to rapidly release, and diffuse down their concentration gradient into nearby cells, bypassing endocytosis. Alternatively, US-induced rupture could be used to release URLs that have been taken up by cells and are trapped in the endosome. Thirdly, liposomes may be ruptured as they pass through the target tissue, creating a high local payload concentration, or releasing a payload modified to be adherent to aid in remaining localized. Even without modifying the payload, this system could function like a local injection in the microvasculature, where placing the source near many surfaces and many sinks (drug targets) has the potential to lead to a local enhancement in delivery.

While passive targeting via EPR has been shown to increase tumor concentrations[61], inter- and intratumor heterogeneity are still obstacles to the development of an effective generalized treatment[202]. The application of US causes a structural change which can increase the likelihood of local cell interaction. This property could be exploited to enhance local delivery. The shear forces present during cavitation are capable of creating unclosed membrane fragments which are thermodynamically unstable and fusogenic[203]. It is this mechanism that is responsible

for the formation of liposomes from lipid solutions by probe sonication. Since these fragments will rapidly reform into more stable liposomes or micelles, their fusion should remain localized to the region of cavitation.

3.2.7 In Vivo Local Delivery of Fluorescent Membrane

In order to test this hypothesis in vivo, URL were fabricated with fluorescently tagged membranes. A near-infrared lipophilic dye, DiR was used to minimize the autofluorescent background. Since the local delivery mechanism proposed here is independent of EPR, the ear of a mouse was chosen as the target. The ear is well vascularized, easy to access and position with a transducer, and the contralateral ear can control for liposome accumulation in the absence of ultrasound.

After intravenous injection of extruded URL, pulsed focused ultrasound applied to the ear was able to cause cavitation, and significantly increase the deposition of fluorescent membrane. Immediately after insonation, a large background of liposomes remaining in circulation made the two ears indistinguishable. However, after 24 hours, a notable difference in fluorescence was observed between the insonated and not insonated ears, as seen in the whole ear scans shown in figure 3.6a,b. The exposed ear showed fluorescence extending outside of the ultrasound focus, possibly due to lipid fragments flowing away before fusing with the blood vessel wall. The intensities used for this experiment (2.3 MPa PNP) did not cause any observable tissue damage. However, at a slightly higher intensity (2.9 MPa PNP), cavitation damage was observed at the ultrasound focus. This produced a much more dramatic accumulation of liposomes confined to the 1 mm diameter ultrasound focal region (figure 3.6c). This ability could be exploited as a local

delivery mechanism which synergizes with therapeutic ultrasound modalities like HIFU.

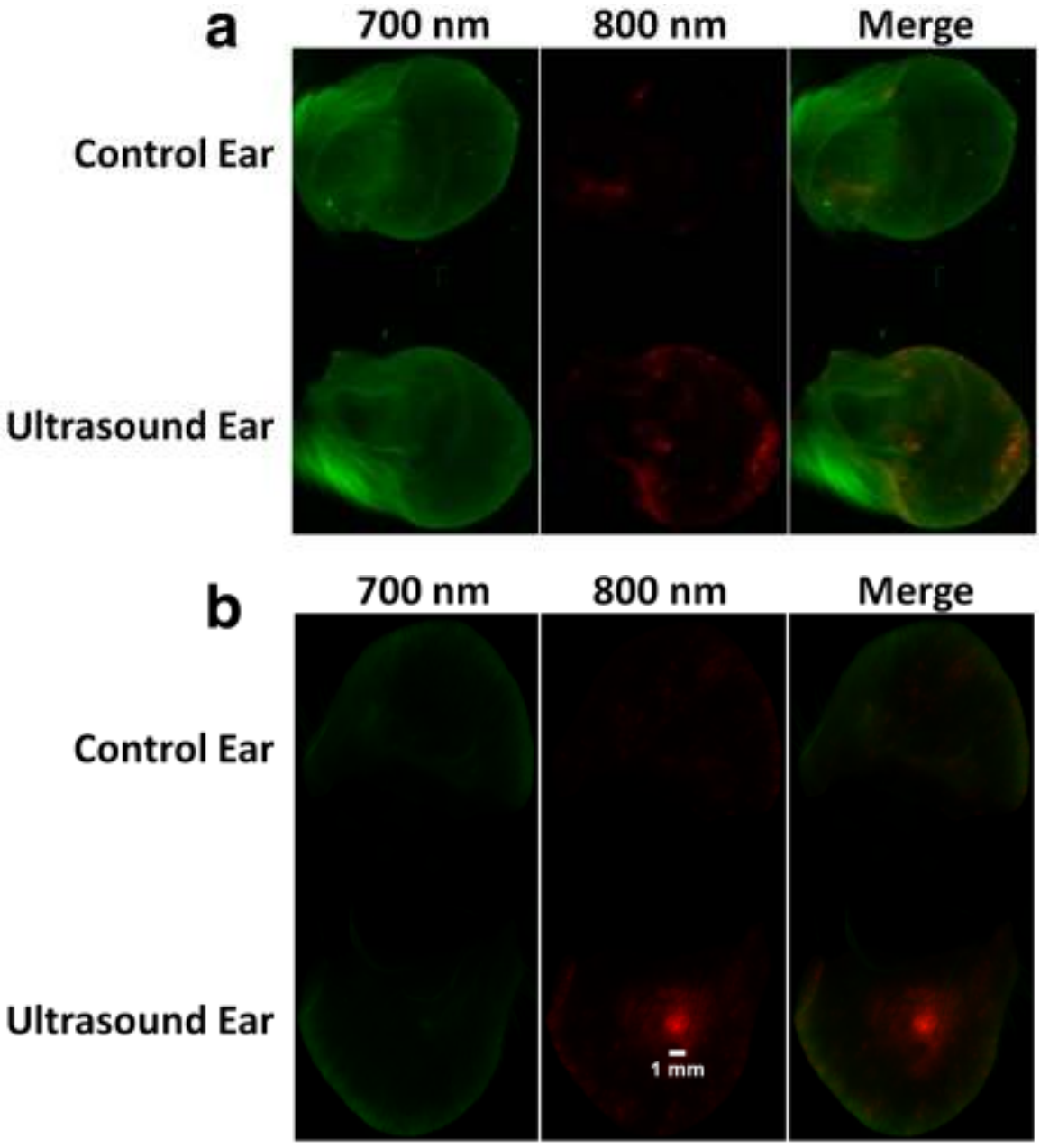

Figure 3.6 Delivery if DiR labeled lipid membranes to a mouse ear using focused ultrasound. a) Fluorescent scan showing ultrasound-induced membrane deposition. Autofluorescence at 700 nm provides a reference and outlines the ear. The 800 nm channel shows the fluorescence of DiR, which corresponds to the location of lipid membranes. a) Exposure to 2.3 MPa US results in a speckled deposition of membrane distant from the ultrasound. b) Exposure to 2.9 MPa US results in cavitation damage localized to a 1 mm region, corresponding to the US focus. There is significant accumulation, which has a fluorescent intensity approximately 14-fold greater than the control ear.

3.2.8 In Vivo Delivery of Calcein to a HT1080 Xenograft

To test the hypothesis that local US-triggered release enhances local concentrations, calcein-loaded liposomes were prepared and delivered to a mouse bearing 2 HT1080 xenograft tumors on either flank. After IV injection of the liposomes, one tumor was insonated with focused ultrasound, resulting in local calcein release. The mouse was euthanized immediately after insonation to ensure visualization of the dye. Calcein is a small polar molecule which cannot diffuse into cells, therefore its residence time in the tumor is not expected to be very long. A 5-fold greater fluorescence intensity was observed in the tumor exposed to ultrasound (figure 3.7a). Membranes were also dyed with DiR to see the fate of the lipids. Since no time was waited to allow clearance of the liposomes from the bloodstream, there was no observed difference in the DiR fluorescence between the insonated and not insonated tumors (figure 3.7a).

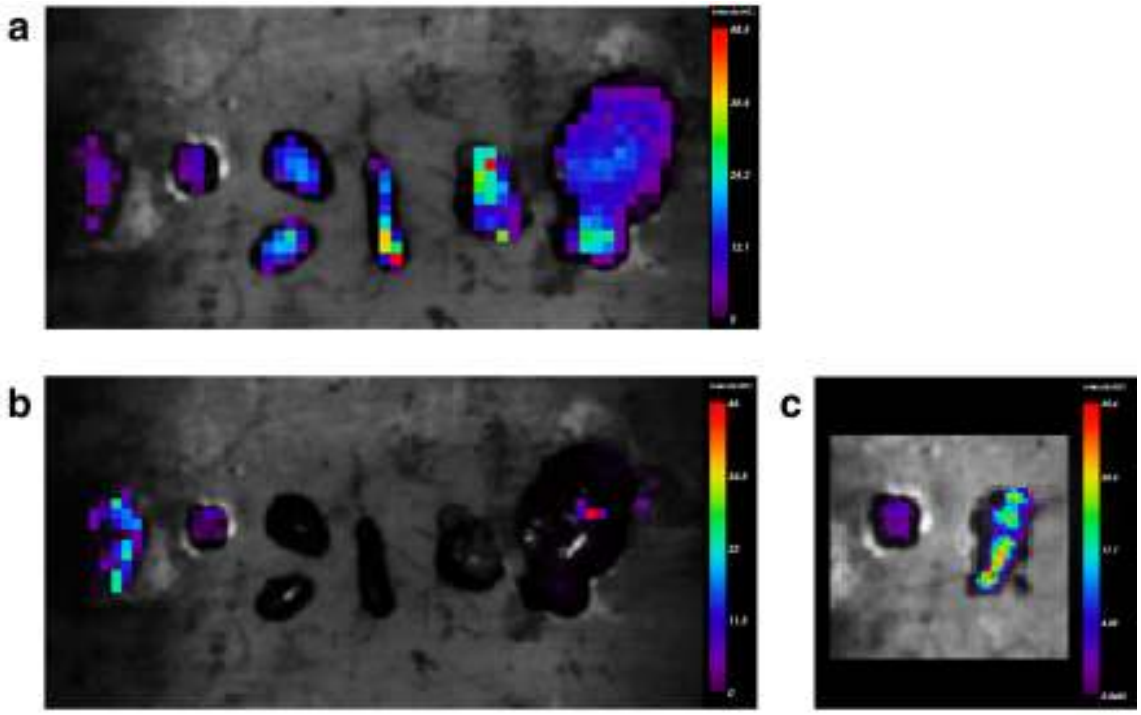

Figure 3.7 Fluorescent imaging of tumors organs from a mouse injected with dual-labelled liposomes, with 1 tumor insonated. a,b) From left to right, insonated tumor, not-insonated tumor, kidneys, spleen, heart and lungs, and liver. a) DiR fluorescence shows an indistinguishable intensity between the two tumors, and an accumulation in the spleen and liver. The heart also shows a high intensity, possibly due to the large blood volume and the liposomes remaining in circulation. b) Calcein fluorescence is only detectable in the tumors and part of the liver. c) High resolution calcein image of the tumors. The insonated tumor was moved to the right side for better imaging. The calcein fluorescence intensity of the insonated tumor was 4-fold greater than the not-insonated tumor.

Fluorescence lifetime imaging (FLIM) allows the determination of the degree of quenching, in an intensity-independent manner. Since the calcein liposomes used here exhibit a dynamic self-quenching, their fluorescence lifetime is significantly shorter in the quenched state (figure 3.8b). Thus, FLIM can aid in determining the fraction of entrapped and released calcein using dual exponential regression analysis. Figure 3.8c shows two tumors from a replicate experiment to figure 3.7. The insonated tumor (shown on the right) has a longer average lifetime from the tumor which was not exposed to ultrasound (shown on the left). This technique may be further used to study the release and breakdown of liposomes containing calcein.

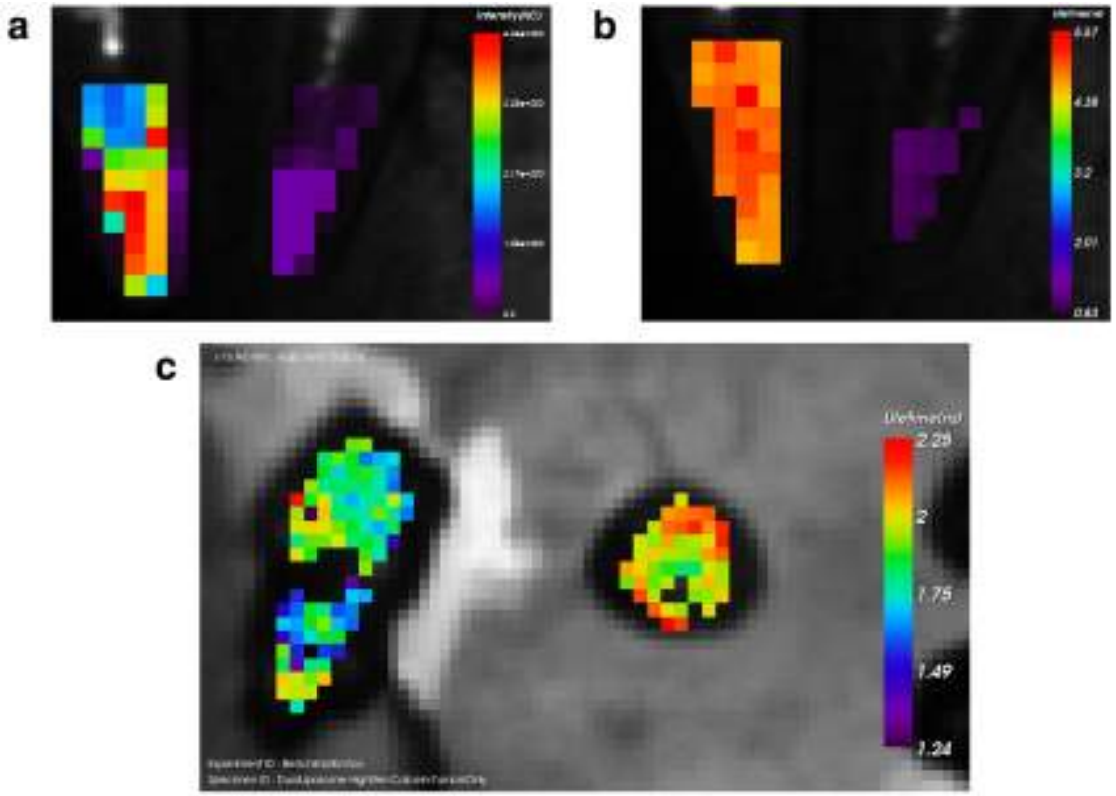

Figure 3.8 Fluorescence lifetime imaging of calcein liposomes in vitro and in vivo. a,b) 2 tubes were filled with either calcein liposomes lysed by probe sonication (left), or unlysed calcein liposomes (right). a) Fluorescence intensity of calcein liposomes shows approximately a 10-fold increase in intensity after lysis. The inhomogeneity of the intensity distribution due to volume and depth dependence illustrates a key challenge in fluorescence intensity imaging. b) The fluorescence lifetime calcein increases approximately 5-fold from the quenched to the free state. The in vitro lifetime may not be representative of the in vivo lifetime, since lifetime is strongly dependent on environment. c) Tumors from a mouse injected with calcein liposomes. The tumor on the right was insonated with ultrasound resulting in release and dilution of the calcein. The fluorescence lifetime of the insonated tumor is significantly greater, in a similar trend to the in vitro results.

3.3 Methods

3.3.1 Preparation of Perfluorocarbon Emulsions

A surfactant solution was prepared by heating 720uL PBS to 85ºC in a 1.5 mL microcentrifuge tube and adding 240uL Zonyl FSO-100 (Sigma Aldrich, St. Louis, MO). This solution was vortexed,to homogenize and cooled in an ice bath. To this solution, 240uL of the appropriate perfluorocarbon was added and an XL-2000 (Misonix, Inc., Farmingdale, NY) probe

was lowered in the tube about 8 mm from the bottom. While still in the ice bath, the sonicator was operated with a LabVIEW program (National Instruments, Austin TX) interfaced with the sonicator via a foot pedal input and a reed relay board (Pencom Design, Inc., Trumbauersville, PA). The program delivered three 0.5 sec bursts and was repeated 120 times. The short bursts prevented the solution from stirring violently and producing foam, and there was a 15 sec delay between each set of 3 bursts to prevent overheating. This resulted in a 20% v/v perfluorocarbon emulsion which was yellowish and translucent in appearance. The perfluorocarbon concentration could be decreased to .1% v/v or increased to 40% v/v by scaling the concentration of the Zonyl FSO-100. Emulsion size could also be increased by decreasing the surfactant concentration. Excess surfactant was removed by dialysis against PBS using the Fast SpinDialyzer (Harvard Apparatus, South Natick, MA) combined with .03 μm track-etched polycarbonate membranes (Whatman, Maidstone, UK).

For the real-time imaging of the transient ADV, perfluorononane emulsions were prepared as described above with 20% v/v perfluorononane and .01% v/v FSO-100, which produced droplets with an average size of 2.4 μm, as observed by light microscopy.

3.3.2 Preparation of Ultrasound-Ruptured Liposomes

Liposomes containing various payloads were prepared by a modified version of the reverse-phase evaporation technique developed by Papahadjopoulos et al.[199]. 3.6 mg DSPE-PEG-5K (Laysan Bio, Inc., Arab, AL) dissolved in chloroform was added to a 1.5 mL microcentrifuge tube. The chloroform was evaporated by applying a gentle argon stream while vortexing the open vial, leaving a lipid film on the walls. To this tube, 800 μL PBS (GIBCO, Bethesda, MD) was added, and the tube was vortexed for 1 minute. To break up the lipids into small micelles, a Misonix XL-2000 (Farmingdale, NY) probe type sonicator was operated at level 10 in the liquid, near the bottom of the tube for 30 0.5 sec pulses. This solution was set aside.

2.48 mg Egg-PC and 1.24 mg Cholesterol (Avanti Polar Lipids, Inc., Alabaster, AL) dissolved in chloroform were combined in a 4 mL glass flat-bottom vial. When it was necessary to fluorescently label the lipid membrane, the lipophilic dye DiO (Biotium, Hayward, CA) was included at 0.1 mol%. The chloroform was evaporated again with the vortex argon stream method. After removing the chloroform, 1 mL of diethyl ether was added, and the vial was vortexed gently. 300 μL of an aqueous solution containing the material to be entrapped was added to the bottom of the vial. The aqueous solutions used were always adjusted to a pH 7.4 and isotonic with PBS to prevent osmotic shock.

The tip of a PowerGen 125 Homogenizer (Fisher Scientific, Pittsburgh, PA) was lowered to just above the bottom of the vial, and was operated on high speed for 1 minute. This created a stable water-in-ether emulsion. The vial was taken immediately to a rotary evaporator and attached by means of a screw-thread adapter. The vial was rotated at a constant 200 rpm and the vacuum pump pressure was set to -18 inHg. After 20 minutes, the solution began to gel as the ether was almost completely removed. For URL containing perfluorooctane nanoemulsions, the vacuum was removed as soon there was first sight of the emulsion boiling. For URL containing perfluoroheptane nanoemulsions, ether was removed with a weak stream of argon.

To the emulsion gel, the PBS solution containing DSPE-PEG-5K was added, and the vial was vortexed on the lowest speed for 1 minute. The vial was then placed under a gentle argon stream for 5 to 10 minutes to remove most of the remaining ether. This separated the closely packed emulsions and completed the liposome formation. To reduce liposome size, the solution of giant liposomes was extruded through track-etched polycarbonate membranes (Whatman, Maidstone, UK) with the appropriate pore diameter. The liposomes were then dialyzed against DPBS using the Fast SpinDialyzer (Harvard Apparatus, South Natick, MA) for 12 hours, which allowed the use of large pore membranes for the efficient removal of the free nanoparticles.

For liposomes loaded with calcein, 50% of the aqueous solution was a 47.5 mM calcein solution adjusted to be isotonic with DPBS and have a pH of 7.4. The remaining 50% was a solution of nanoparticles or DPBS for the controls. Typically, a 20% v/v PFC emulsion was used to achieve a final concentration of 10% v/v emulsion in the liposomes. After liposome fabrication, the free calcein was removed by dialysis. The buffer was changed 3 or 4 times until the fluorescence intensity of the equilibrated dialysis buffer was less than 2 times that of DPBS.

3.3.3 Fluorescent Videography of Ultrasound Response

A microscope system described elsewhere[204] was used to monitor the response of URL to focused ultrasound. Briefly, 10 ms 2.25 MHz ultrasound pulses at a peak negative pressure of 1.3 MPa were delivered with a Panametrics V305-SU (Olympus NDT Inc., Waltham, MA), 2.25 MHz transducer connected via a Panametrics BCU–58–6 W waterproof connector cable. Response was monitored in brightfield or fluorescence mode, and images were captures by a FASTCAM 1024 PCI (Photron, San Diego, CA). The transducer was submerged in a water tank and was pointing towards the air surface. The sample was either held on a glass slide under a coverslip at the air/water interface, or sandwiched between two sealed thin plastic films.

3.3.4 Calcein Release in a Transfer Pipet

Calcein-loaded liposomes were diluted 100X into DPBS. 2 mL aliquots of the diluted liposomes were loaded into standard disposable transfer pipettes (ThermoFisher Scientific, Waltham, MA). Hydrophone measurements showed that there was >95% transmission through the plastic walls of the pipet. An H-102 HIFU transducer (Sonic Concepts, Bothell, WA) was placed flat on the bottom of a water bath heated to 37°C. The pipets were held by a clamp, so that the bottom of the bulb was in the center of the transducer alignment cone. The water bath level was adjusted to be at least as high as the liquid in the pipet. The 2 mL volume contained in the

pipet filled the sample up to a height > 1.5 cm above the transducer focus. Samples were allowed to equilibrate with bath temperature for 2 minutes prior to insonation.

3.3 MHz sine wave pulses were produced by a NI-5412 arbitrary waveform generator (National Instruments, Austin, TX) and amplified by a 300 W amplifier (Vox Technologies, Richardson, TX). Pulse length was varied from 10 to 10,000 cycles (3.03 to 3,030 μs) and repeated with a duty cycle of 1 or 10%.

3.3.5 In Vivo Insonation Setup

Aquasonic ultrasound transmission gel (Parker Labs, Fairfield, NJ) was degassed by centrifugation at 4150 rpm for 10 minutes in a plastic bag. A corner of the bag was cut so that the gel could be pipetted into the transducer alignment cone and onto the ceramic ring of the transducer. The cone was then placed on the transducer, and remaining gas pockets were removed with a syringe. An elevated platform was constructed for the mouse to lay on while receiving anesthesia. A hole in the platform allowed the tip of the transducer alignment cone to protrude slightly so that the target on the mouse could be easily placed in the correct focus.

3.3.6 In Vivo Membrane Delivery to a Mouse Ear

For in vivo experiments, URL were prepared as described above, and to the lipid mixture .1 mol% DiR (Biotium, Hayward, CA) was added to fluorescently tag the liposome membranes. After preparation, the final lipid concentration was 7.32 mg/mL.

One male Swiss Webster white mouse (5-6 week old), weighing 26.0 g was anesthetized with isoflurane vapor. The mouse was then injected with 150 μL liposome solution into the tail vein, corresponding to a lipid dose of 42.2 $mg \cdot kg^{-1}$. A H-102 HIFU transducer (Sonic Concepts, Bothell, WA) was filled with degassed Aquasonic ultrasound transmission gel for efficient acoustic coupling. The mouse was positioned so that its left ear was centered over the focus of the

transducer, and excess gel was applied to minimize acoustic reflections. 10 minutes after injection, ultrasound was applied for 30 minutes. A PCI-5412 (National Instruments, Austin, TX) arbitrary waveform generator produced a 303 μsec pulse of 1000 cycle sine wave at 3.3 MHz, the 3rd harmonic of the transducer. The pulse was repeated continuously at a 1% duty cycle. The gain was adjusted on a 300 W amplifier (Vox Technologies, Richardson, TX) to produce a peak negative pressure of 2.3 MPa.

Immediately after the 30 minute duration, the mouse was euthanized by cervical dislocation. The heart, lungs, liver, spleen, and kidneys were excised and frozen in blocks of Tissue-Tek OCT (Miles Scientific, Elkhart, IN). Both ears were also harvested and imaged for fluorescence at 700 nm and 800 nm using an Odyssey scanner (LI-COR Inc., Lincoln, NB). The ears were then also frozen in OCT blocks. Cryo sections of the organs and ears were cut and imaged in brightfield and fluorescence modes using a Cy7 filter set.

3.3.7 In Vivo Delivery of Calcein to HT1080 Xenograft Tumors

Tumor Implantation

HT1080 human fibrosarcoma cells were cultured and harvested. Approximately 10^6 cells were injected subcutaneously into both flanks of a female nu/nu mouse (5-6 week old, Charles River, San Diego, CA) at day 0. At day 10, tumors had grown at the injection sites to approximately 100 mm^3.

Calcein-loaded URL for In Vivo Delivery

URL were prepared as described above, with the aqueous solution containing 42.75 mM calcein and 2% v/v perfluorononane emulsions. 0.1 mol% DiR (Biotium, Hayward, CA) was included in the lipid formulation for visualization of the lipid membranes. Final lipid concentration was 6.59 mg·ml^{-1}

Tumor Insonation

While under anesthesia, 100 µL of a URL suspension (6.59 $mg \cdot ml^{-1}$) was injected into the tail vein of a mouse. The mouse was then placed on a platform on its side with the center of one tumor over the center of the transducer alignment cone. Additional impedance-matching gel was added to the top of the tumor to limit acoustic reflections at the tumor surface. While under constant anesthesia, ultrasound was applied for 30 minutes

Fluorescence Imaging of Excised Tissues

Fluorescence of excised organs and tumors were imaged with the eXplore Optix (GE Healthcare, Giles, UK). A GFP filter set was used to visualize calcein and a Cy7 filter set was used to visualize the DiR. Fluorescence lifetime analysis of calcein images was performed with OptiView software (Advanced Research Technologies Inc., Montreal, QC, Canada) and allowed the differentiation of entrapped and free calcein.

3.3.8 Electron Microscopy

Cryo-TEM images were acquired by Nano Imaging Services (San Diego, CA). Vitrification (rapid freezing) of undiluted liposome samples was performed by plunging sample suspensions supported on a C-Flat holey carbon film (Protochips, Inc., Raleigh, NC) into ethane liquefied in a small container in a bath of liquid nitrogen. After vitrification, sample grids were maintained at a temperature below −170 °C at all times. Imaging was performed on a Tecnai T12 transmission electron microscope (FEI, Hillsboro, OR) operating at 120 keV equipped with an FEI Eagle 4K × 4K CCD camera. The images were acquired at a nominal underfocus of −5 µm (21,000×) and −4 µm (52,000×) with electron doses of approximately 10–15 $e^{-}/Å^{2}$.

3.4 Conclusions

In summary, the incorporation of cavitation nucleation sites into liposomes has yielded a platform delivery vehicle, capable of carrying and releasing a broad variety of payloads with

ultrasound. The inclusion of PFC nanoemulsions as the nucleation sites lowered the acoustic intensity threshold for cavitation, which was shown to facilitate the rupture of the liposome membrane, and release of an encapsulated small molecule. Liposome rupture was restricted to the ultrasound focus, demonstrating its potential for specific spatial control. The fabrication method was able to produce liposomes of a controllable size between 100-500 nm containing highly concentrated emulsions and 100 nm gold nanoparticles. This vehicle, by virtue of its liposomal structure, benefits from the vast knowledgebase, optimized formulations, and clinical history of liposomes such as Doxil®, Lipo-Dox®, DaunoXome®, and DepoCyt®. The unique property of rapid exposure lends itself well to the delivery of poorly circulating payloads such as transfection complexes, foreign proteins, viruses, and small molecules which can readily diffuse across the plasma membrane. When combined with the ability to increase the specificity of therapy with precisely focused ultrasound, the URL has application in many localized diseases where a systemic chemical treatment results in negative side effects.

Furthermore, the application of high boiling point liquid PFC's to nucleate cavitation is an area which merits further research. Though higher boiling point perfluorocarbons cannot produce stable bubbles, a transient ADV-like effect was observed for micron-sized PFN droplets. This might be exploited to trigger release of drugs or nucleic acids loaded on the surface of emulsion droplets. Beyond their ability to trigger release of therapeutic molecules, these stable emulsion particles could be also be used as effective sensitizers for non-thermal HIFU ablation of tumors.

3.5 Acknowledgements

This chapter, in part, is being prepared for submission for publication as Benchimol, Michael; Barback, Christopher; Ibsen, Stuart; Simberg, Dmitri; Wu, Zhe; Mattrey, Robert;

Esener, Sadik. “An Ultrasound-Ruptured Liposome Using Cavitation Threshold Reducing Nanoparticles”.

I thank NanoImaging Services, Inc. for performing the cryoTEM imaging.

3.6 References

155. Merritt, C.R., Kremkau, F.W. & Hobbins, J.C. Diagnostic ultrasound: bioeffects and safety. *Ultrasound in obstetrics & gynecology : the official journal of the International Society of Ultrasound in Obstetrics and Gynecology* **2**, 366-374 (1992).

156. Blomley, M.J., Cooke, J.C., Unger, E.C., Monaghan, M.J. & Cosgrove, D.O. Microbubble contrast agents: a new era in ultrasound. *Bmj* **322**, 1222-1225 (2001).

157. Hernot, S. & Klibanov, A.L. Microbubbles in ultrasound-triggered drug and gene delivery. *Advanced drug delivery reviews* **60**, 1153-1166 (2008).

158. Miller, D.L., Pislaru, S.V. & Greenleaf, J.E. Sonoporation: mechanical DNA delivery by ultrasonic cavitation. *Somat Cell Mol Genet* **27**, 115-134 (2002).

159. Karshafian, R., Samac, S., Bevan, P.D. & Burns, P.N. Microbubble mediated sonoporation of cells in suspension: clonogenic viability and influence of molecular size on uptake. *Ultrasonics* **50**, 691-697.

160. Cochran, M.C., Eisenbrey, J., Ouma, R.O., Soulen, M. & Wheatley, M.A. Doxorubicin and paclitaxel loaded microbubbles for ultrasound triggered drug delivery. *Int J Pharm* **414**, 161-170.

161. Carson, A.R. et al. Gene therapy of carcinoma using ultrasound-targeted microbubble destruction. *Ultrasound Med Biol* **37**, 393-402.

162. Lentacker, I., Geers, B., Demeester, J., De Smedt, S.C. & Sanders, N.N. Design and evaluation of doxorubicin-containing microbubbles for ultrasound-triggered doxorubicin delivery: cytotoxicity and mechanisms involved. *Mol Ther* **18**, 101-108.

163. Ibsen, S. et al. A novel nested liposome drug delivery vehicle capable of ultrasound triggered release of its payload. *J Control Release* **155**, 358-366.

164. Huang, S.L., McPherson, D.D. & Macdonald, R.C. A method to co-encapsulate gas and drugs in liposomes for ultrasound-controlled drug delivery. *Ultrasound Med Biol* **34**, 1272-1280 (2008).

165. Eisenbrey, J.R., Soulen, M.C. & Wheatley, M.A. Delivery of encapsulated Doxorubicin by ultrasound-mediated size reduction of drug-loaded polymer contrast agents. *IEEE Trans Biomed Eng* **57**, 24-28.

166. Calliada, F., Campani, R., Bottinelli, O., Bozzini, A. & Sommaruga, M.G. Ultrasound contrast agents: basic principles. *Eur J Radiol* **27 Suppl 2**, S157-160 (1998).

167. Postema, M. & Schmitz, G. Ultrasonic bubbles in medicine: influence of the shell. *Ultrason Sonochem* **14**, 438-444 (2007).

168. Dijkmans, P.A. et al. Microbubbles and ultrasound: from diagnosis to therapy. *European journal of echocardiography : the journal of the Working Group on Echocardiography of the European Society of Cardiology* **5**, 245-256 (2004).

169. Chen, W.S., Matula, T.J., Brayman, A.A. & Crum, L.A. A comparison of the fragmentation thresholds and inertial cavitation doses of different ultrasound contrast agents. *J Acoust Soc Am* **113**, 643-651 (2003).

170. Schneider, M. Characteristics of SonoVuetrade mark. *Echocardiography* **16**, 743-746 (1999).

171. Correas, J.M. et al. Ultrasound contrast agents: properties, principles of action, tolerance, and artifacts. *Eur Radiol* **11**, 1316-1328 (2001).

172. Lim, A.K. et al. Evidence for spleen-specific uptake of a microbubble contrast agent: a quantitative study in healthy volunteers. *Radiology* **231**, 785-788 (2004).

173. Ferrara, K.W., Borden, M.A. & Zhang, H. Lipid-shelled vehicles: engineering for ultrasound molecular imaging and drug delivery. *Acc Chem Res* **42**, 881-892 (2009).

174. Zhang, L. et al. Nanoparticles in medicine: therapeutic applications and developments. *Clinical pharmacology and therapeutics* **83**, 761-769 (2008).

175. Petros, R.A. & DeSimone, J.M. Strategies in the design of nanoparticles for therapeutic applications. *Nature reviews. Drug discovery* **9**, 615-627 (2010).

176. Pisani, E. et al. Perfluorooctyl Bromide Polymeric Capsules as Dual Contrast Agents for Ultrasonography and Magnetic Resonance Imaging. *Adv Funct Mater* **18**, 2963-2971 (2008).

177. Rapoport, N. et al. Ultrasound-mediated tumor imaging and nanotherapy using drug loaded, block copolymer stabilized perfluorocarbon nanoemulsions. *J Control Release* **153**, 4-15.

178. Kripfgans, O.D., Fowlkes, J.B., Miller, D.L., Eldevik, O.P. & Carson, P.L. Acoustic droplet vaporization for therapeutic and diagnostic applications. *Ultrasound in medicine & biology* **26**, 1177-1189 (2000).

179. Lo, A.H., Kripfgans, O.D., Carson, P.L., Rothman, E.D. & Fowlkes, J.B. Acoustic droplet vaporization threshold: effects of pulse duration and contrast agent. *IEEE transactions on ultrasonics, ferroelectrics, and frequency control* **54**, 933-946 (2007).

180. Fabiilli, M.L. et al. The role of inertial cavitation in acoustic droplet vaporization. *IEEE Trans Ultrason Ferroelectr Freq Control* **56**, 1006-1017 (2009).

181. Wang, C.H. et al. Aptamer-conjugated and drug-loaded acoustic droplets for ultrasound theranosis. *Biomaterials* **33**, 1939-1947.

182. Fabiilli, M.L. et al. Delivery of chlorambucil using an acoustically-triggered perfluoropentane emulsion. *Ultrasound Med Biol* **36**, 1364-1375.

183. Sazgarnia, A., Shanei, A., Meibodi, N.T., Eshghi, H. & Nassirli, H. A novel nanosonosensitizer for sonodynamic therapy: in vivo study on a colon tumor model. *J Ultrasound Med* **30**, 1321-1329 (2011).

184. Ho, V.H., Smith, M.J. & Slater, N.K. Effect of magnetite nanoparticle agglomerates on the destruction of tumor spheroids using high intensity focused ultrasound. *Ultrasound Med Biol* **37**, 169-175.

185. Smith, M.J., Ho, V.H., Darton, N.J. & Slater, N.K. Effect of magnetite nanoparticle agglomerates on ultrasound induced inertial cavitation. *Ultrasound Med Biol* **35**, 1010-1014 (2009).

186. Sazgarnia, A., Shanei, A., Meibodi, N.T., Eshghi, H. & Nassirli, H. A novel nanosonosensitizer for sonodynamic therapy: in vivo study on a colon tumor model. *J Ultrasound Med* **30**, 1321-1329.

187. Shchukin, D.G., Skorb, E., Belova, V. & Mohwald, H. Ultrasonic cavitation at solid surfaces. *Adv Mater* **23**, 1922-1934.

188. Brennen, C.E. Cavitation and Bubble Dynamics. (Oxford University Press, New York; 1995).

189. Flaim, S.F. Pharmacokinetics and side effects of perfluorocarbon-based blood substitutes. *Artif Cells Blood Substit Immobil Biotechnol* **22**, 1043-1054 (1994).

190. Schutt, E. et al. Proposed mechanism of pulmonary gas trapping (PGT) following intravenous perfluorocarbon emulsion administration. *Artif Cells Blood Substit Immobil Biotechnol* **22**, 1205-1214 (1994).

191. Kripfgans, O.D., Fowlkes, J.B., Woydt, M., Eldevik, O.P. & Carson, P.L. In vivo droplet vaporization for occlusion therapy and phase aberration correction. *IEEE Trans Ultrason Ferroelectr Freq Control* **49**, 726-738 (2002).

192. Wagterveld, R.M., Boels, L., Mayer, M.J. & Witkamp, G.J. Visualization of acoustic cavitation effects on suspended calcite crystals. *Ultrason Sonochem* **18**, 216-225.

193. Atchley, A.A. et al. Thresholds for cavitation produced in water by pulsed ultrasound. *Ultrasonics* **26**, 280-285 (1988).

194. Roy, R.A., Madanshetty, S.I. & Apfel, R.E. An acoustic backscattering technique for the detection of transient cavitation produced by microsecond pulses of ultrasound. *J Acoust Soc Am* **87**, 2451-2458 (1990).

195. Gateau, J., Aubry, J.F., Pernot, M., Fink, M. & Tanter, M. Combined passive detection and ultrafast active imaging of cavitation events induced by short pulses of high-intensity ultrasound. *IEEE Trans Ultrason Ferroelectr Freq Control* **58**, 517-532.

196. Salgaonkar, V.A., Datta, S., Holland, C.K. & Mast, T.D. Passive cavitation imaging with ultrasound arrays. *J Acoust Soc Am* **126**, 3071-3083 (2009).

197. Kripfgans, O.D., Fabiilli, M.L., Carson, P.L. & Fowlkes, J.B. On the acoustic vaporization of micrometer-sized droplets. *J Acoust Soc Am* **116**, 272-281 (2004).

198. Le, T.D. & Weers, J.G. QSPR and GCA models for predicting the normal boiling points of fluorocarbons. *J. Phys. Chem.* **99**, 6739-6747 (1995).

199. Szoka, F., Jr. & Papahadjopoulos, D. Procedure for preparation of liposomes with large internal aqueous space and high capture by reverse-phase evaporation. *Proceedings of the National Academy of Sciences of the United States of America* **75**, 4194-4198 (1978).

200. Akulichev, V.A. Hydration of ions and the cavitation resistance of water. *Sov Phys Acoustics* **12**, 144-149 (1966).

201. Crum, L.A. Nucleation and stabilization of microbubbles in liquids, Vol. 38. (1982).

202. Bae, Y.H. Drug Targeting and Tumor Heterogeneity. *J Control Release* **133**, 2-3 (2008).

203. Xi, X. et al. A targeting drug-delivery model via interactions among cells and liposomes under ultrasonic excitation. *Physics in medicine and biology* **53**, 3251-3265 (2008).

204. Ibsen, S., Benchimol, M. & Esener, S. Fluorescent microscope system to monitor real-time interactions between focused ultrasound, echogenic drug delivery vehicles, and live cell membranes. *Ultrasonics* (2012).

Chapter 4:

Ultrasound-Directed Exposure of Asymmetric Beta-lactamase Liposomes

Abstract

Cancer enzyme-prodrug therapy has been actively explored for over two decades for its potential to produce high local concentrations of cytotoxic drugs in cancer tissues. Failed clinical trials have highlighted the need to achieve specific delivery of enzymes as well as protect exogenous enzymes from antibody responses. A recently developed liposome with ultrasound-controlled release can address both of these concerns by shielding the enzyme during transit and spatially restricting enzyme exposure using tightly focused ultrasound waves. β-lactamase has been incorporated into liposome membranes by chemical conjugation to a phospholipid. Fluorescent tagging of the enzyme demonstrated efficient partitioning into the lipid bilayer. Proteolytic degradation or cleavage of outward facing enzyme reduced activity of liposomes until ultrasound-induced lysis exposed inner enzymes to increase activity 15-fold. This system has the properties of both protection and specificity needed to make an impact in the field of enzyme-prodrug delivery.

4.1 Introduction

Among the many medicinal applications of enzymes, one has been to convert relatively benign prodrugs into their more toxic forms to treat cancer. Similar to all systemic chemotherapy approaches, specific delivery of the enzyme to the tumor determines the extent to which healthy tissues are exposed to the converted drug. The repeated activation of prodrug in regions of active enzyme provides an amplification mechanism that complements targeting mechanisms which are receptor limited and nanoparticle carriers which are cargo limited. The use of targeting ligands can improve the distribution of nanoparticles in tumor tissue [118, 119, 205], but is often non-selective and insufficient to boost the amount of drug to the tumor. In order to overcome the systemic toxicity of chemotherapy, the enzyme prodrug therapies (antibody-, gene therapy- and virus-Directed: ADEPT, GDEPT, VDEPT, respectively) have been developed, where a bacterial

enzyme is capable of converting a prodrug into the active drug and is delivered to or made to be expressed in the tumor. The biggest drawback of enzyme/prodrug therapies is that they often rely on enzymes normally absent from the host, due to the lack of enzymes uniquely present in the tumor, and not in other tissues like the liver. Thus, the careful design of a prodrug to be specific to an exogenous enzyme prevents the premature activation by endogenous enzymes, which would result in toxicity to off-target organs[206]. The downside of using such enzymes is that they are immunogenic, so that after repeated dosing, patients generate antibodies that opsonize the enzyme before it can reach the desired site of action[207]. As in ADEPT, a strong response of neutralizing antibodies would preclude extended therapy[208]. When antibodies are the targeting mechanism, an additional problem is slow clearance of antibody-enzyme conjugates from the bloodstream[209].

Antibody-directed enzyme prodrug therapy (ADEPT) is an elegant approach for targeting enzymes to convert generally less toxic prodrugs into their active form in the tumor. Clinical trials have shown two major limitations: the lack of tumor specificity and the immunogenicity of the enzymes. In many cases, the patient's own antibodies intercept the enzyme before it can reach the tumor, terminating the effectiveness of the treatment[208, 209]. Furthermore, even if these two hurdles could be overcome, this approach could only achieve the necessary specificity for a fraction of the patient population that presents the appropriate antibody receptor target.

The strategy of gene-directed enzyme prodrug therapy (GDEPT) is to deliver a gene encoding the enzyme of interest. This is accomplished using a nucleic acid combined with a method to achieve transfection in the target cells. Although efficiency of transfection may initially be low, this may be compensated by the ability for transfected cells to produce many enzymes. A similar scheme uses viruses to deliver the gene (VDEPT), and has the potential for amplification and improved tissue penetration by creating a viral infection with replicating viruses. Unfortunately, for either of these two approaches to succeed, they must first be able to

solve the challenges of viral/nucleic acid delivery, which have been some of the main hurdles to achieving effective gene therapy[210].

In chapter 3, an ultrasound-sensitive liposome has been developed as a controlled release therapeutic delivery vehicle. Here, this structure has been modified to create a novel liposomal delivery system which can shield an enzyme, allowing for long circulation to reach the tumor site. Localized exposure of the hidden enzyme can be achieved using focused ultrasound, in order to implant an enzymatically active environment in the tumor in a spatially-selective manner. Physically determining the affected region through positioning of an instrument bypasses all dependence on biochemical tissue properties.

4.2 Ultrasound-Directed Enzyme Prodrug Therapy (UDEPT) Concept

Ultrasound has the potential to scramble membrane structures in specific regions defined by an operator external to the body. This can be used to release entrapped solutes, or rearrange membrane components. In this work, liposomes containing membrane-bound enzyme asymmetrically loaded on the inner membrane leaflet exploit this property to act as an enzyme source triggerable by ultrasound. Inversion of the membranes exposes the enzyme to prodrug substrates for conversion to their cytotoxic form at the defined site. Since the biodistribution of exposed enzyme is determined by the region exposed to ultrasound, this concept has been termed ultrasound-directed enzyme prodrug therapy (UDEPT).

Previous enzyme prodrug therapies have shown the benefit of allowing a time delay between enzyme delivery and prodrug administration, to allow clearance of enzyme from healthy tissues[211]. To aid in keeping the membrane structures localized during this time, surface ligands or adhesive components can be incorporated. After administration and ultrasound activation, enzyme deposited on regions of the tumor vasculature could then convert prodrug and act as a source of active drug in the local vicinity. Converted small molecule drugs will be able to diffuse

into nearby cells, as well as into the general bloodstream. The exposure of the rest of the body to circulating drug is unavoidable. However, creating a concentrated source of the drug in the tumor volume can lead to enhanced delivery at the target, increasing the contrast to off-target areas and consequently the therapeutic index. Targeting cancer cells (which requires extravasation) could further improve the efficiency of local delivery by restricting converted drug to the vicinity of target cells, and away from the flowing bloodstream.

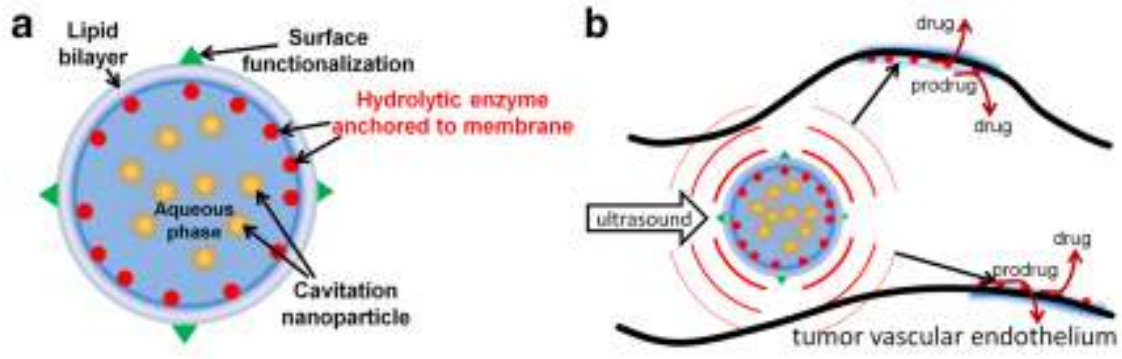

Figure 4.1 Ultrasound-Directed Enzyme Prodrug Therapy (UDEPT). a) Schematic of an Ultrasound-Ruptured Enzymatically-Active Liposome (UREAL). A liposome encapsulates one or more nanoparticle nucleation sites for acoustic cavitation to make an ultrasound-sensitive nanocarrier. A hydrolytic enzyme such as β-lactamase is attached to the inner membrane leaflet so that it is protected from degradation and immune recognition. b) UDEPT Concept. Circulating UREAL carriers are ruptured at the disease target using focused ultrasound. Membrane fragments containing now exposed enzyme incorporate with the tumor vascular endothelium through ligand attachment or membrane fusion. A separately administered prodrug is converted into its active form in the presence of enzyme, and can subsequently diffuse into nearby cells.

4.3 Results and Discussion

The wide range of methods for enzyme delivery allows tailoring to prodrugs with differing pharmacokinetic properties. Both strategies of achieving enzyme concentrations intracellular or extracellular have their respective advantages and disadvantages. With specific intracellular delivery, there is less likelihood of an activated drug product flowing away in the bloodstream. However, this limits the use of prodrugs to those whose protection mechanism is

based on blocking diffusion through the plasma membrane. Also, intracellular delivery requires carrying the enzyme into the cell via an uptake mechanism such as endocytosis, or causing the cell to produce the enzyme by transfection (also dependent on endocytosis), which is a challenge in of itself. To limit the delivery hurdles, the approach of UDEPT described here is to create an enzymatically active environment in extracellular space of the tumor, similar to if the cancer cells or their supporting endothelial cells were to express a unique surface enzyme.

Liposomes carrying the enzyme can serve as efficient delivery vehicles, with the potential for long retention at the target site. A major reason for the early adoption of liposomes as therapeutic nanocarriers for cancer (e.g. Doxil®) is their biocompatibility and similarity in composition to natural cell membranes. The goal of UDEPT is thus to leverage these properties to replace the existing cell surface with cell membrane-like liposome membranes presenting attached enzymes (Figure 4.1). To produce a liposome for this application, we have incorporated the robust and highly active enzyme, β-lactamase. β-lactamase is produced by some Gram-negative bacteria to allow them to degrade antibiotics containing a β-lactam ring structure (e.g. penicillin)[212]. Since this enzyme has been thoroughly investigated for enzyme-prodrug therapy, numerous β-lactam-modified drugs have been synthesized as prodrug candidates[211, 213]. Many of these drugs achieve the desired cytotoxicity enhancement upon cleavage by β-lactamase, but their potential has not been realized due to limitations in the delivery of the enzyme.

4.3.1 Bioconjugation of β-lactamase to a Phospholipid

To anchor β-lactamase in a liposome bilayer, the enzyme was conjugated to the hydrophilic end of a PEGylated phospholipid through one of its exposed amine groups. A disulfide linkage was included in the conjugate structure to allow for efficient detachment of exposed enzyme by exposure to a reducing agent. An alternative conjugate was also tested, where proteolysis was instead used to degrade the exposed enzyme.

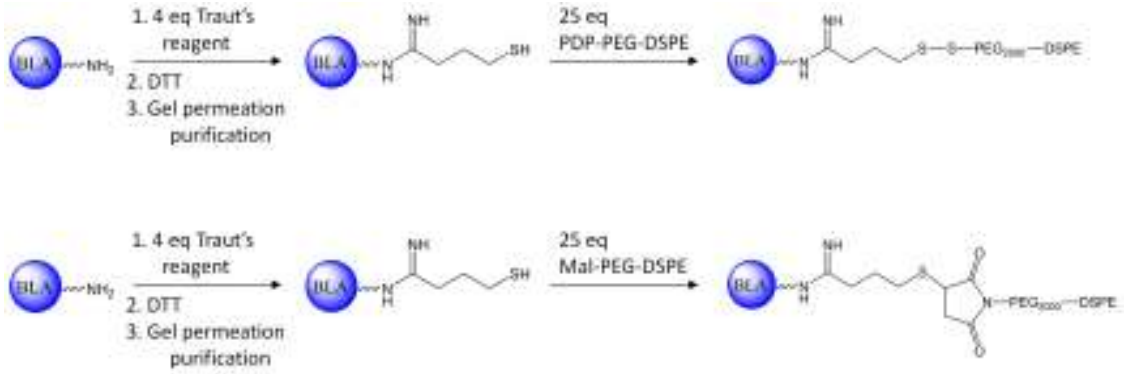

Figure 4.2 Chemical conjugation of β-lactamase to the functional phospholipids DSPE-PEG(2000)-PDP and DSPE-PEG(2000)-maleimide. Reaction of amine groups on β-lactamase with Traut's reagent produces an active thiol which is reactive to PDP and maleimide groups. The PDP-thiol reaction produces a disulfide bond which can be attacked by a reducing agent for cleavage of the β-lactamase. The maleimide-thiol reaction is more efficient, and the conjugate is more stable, so that exposed enzyme must be removed by proteolytic degradation.

In the conjugate synthesis, the number of molecular equivalents of lipid to enzyme determined the structure of the resulting conjugates. The commercially acquired β-lactamase contained two active enzymes, which differed by about 3,000 Daltons, and can be seen as the two main bands on the gel shown in figure 4.3. Since this difference was similar to the molecular weight of one lipid molecule, addition of a single lipid to the lower molecular weight form resulted in a conjugate which was indistinguishable to the higher molecular weight form. The use of 4 equivalents of Traut's reagent and 25 equivalents of DSPE-PEG-PDP for each molecule of β-lactamase resulted in labeling of nearly all enzymes with the lipid. Both a sequential and a concerted reaction were tested. The efficiency of achieving the correct product was approximately equivalent for both methods.

The PDP moiety binds thiols to produce a disulfide linkage which can be broken with a reducing agent such as DTT, or TCEP. Addition of DTT efficiently reduced the disulfide linkage, removing the attached lipids, and resulting in the original unmodified enzyme bands. To produce

a conjugate which would remain stable in reducing environments, DSPE-PEG(2000)-maleimide was reacted with the thiolated enzyme.

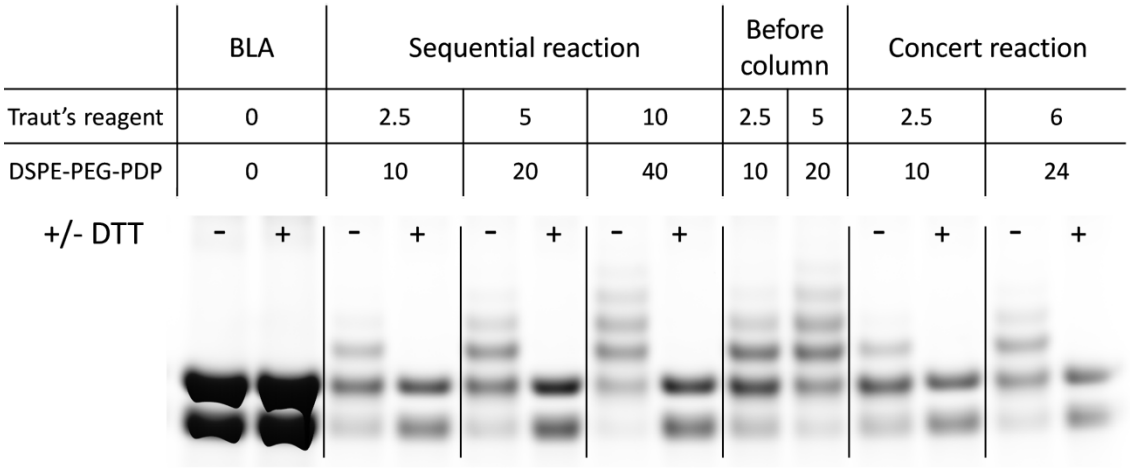

Figure 4.3 SDS gel showing optimization of lipid conjugation to fluorescent BLA. BLA fluorescently tagged with BODIPY-FL was reacted with Traut's reagent (TR) and DSPE-PEG(2000)-PDP in sequence and in concert. Number of equivalents of TR and lipid molecules were varied, keeping a constant ratio of 1:4 TR:lipid. Both the concerted and sequential reaction yielded similar results. The use of more equivalents in the sequential reaction produced more reacted enzyme, but producing higher MW bands, indicating the attachment of multiple lipid molecules. In all cases, addition of DTT reduced the disulfide linkage and produced the original enzyme bands. Samples: 4 µL water, 4 µL staining solution (4X) and 8 µL sample (20 µM), W/WO 1 µL DTT (1 M stock solution in water. Samples were loaded on a 15-well 4-12% Bis-Tris gel, 1.5 mm (Invitrogen). The gel was run with MEM-SDS, 110 V, 85 mAmp for 90 minutes. The gel was then imaged on UVP (excitation 485/20 emission 530/20).

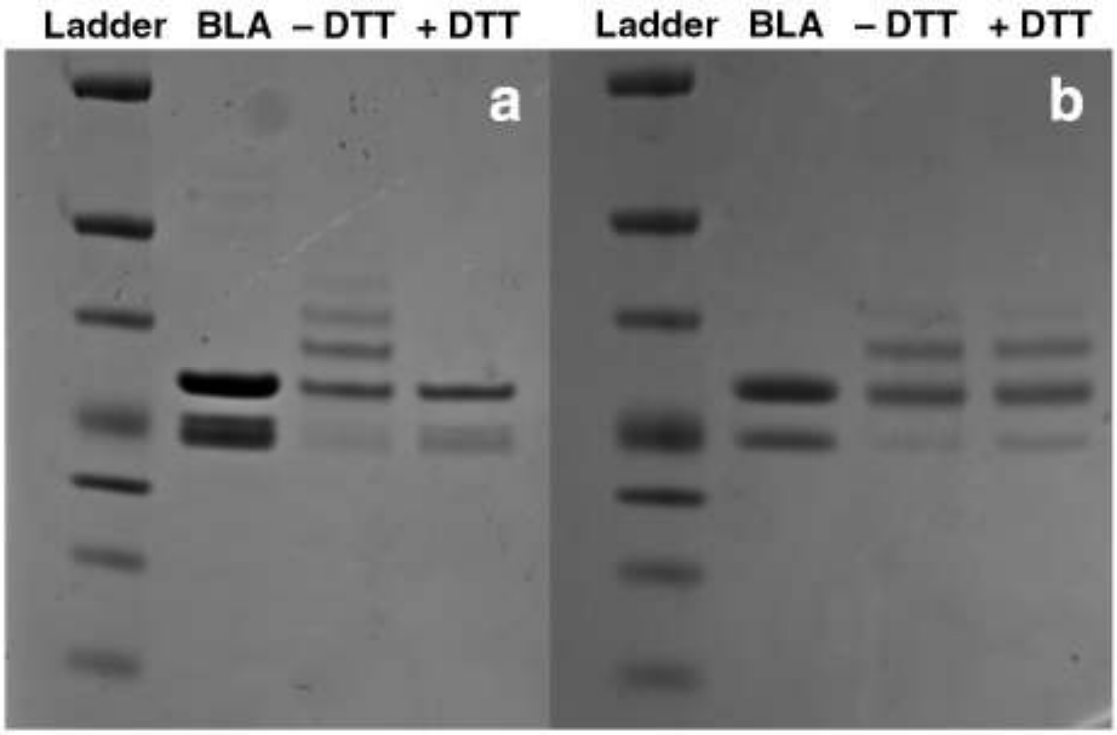

Figure 4.4 SDS gel of non-fluorescent BLA conjugated to a) PDP and b) maleimide functionalized lipids. Samples: 4 µL water, 4 µL staining solution (4X) and 8 µL sample (20 µM), W/WO 1 µL DTT (1 M stock solution in water. Samples were loaded on a 15-well 4-12% Bis-Tris gel, 1.5 mm (Invitrogen). Gels were ran with MEM-SDS, 110 V, 85 mAmp for 90 minutes. The gel was then stained with Coomassie Blue, de-stained and imaged on UVP. The conjugation protocol yielded similar results for the two functionalized lipids. However, after addition of DTT, the original enzyme bands return for the **a)** DSPE-PEG(2000)-PDP-BLA conjugate, but not for the **b)** DSPE-PEG(2000)-Mal-BLA conjugate which has no reducible linker.

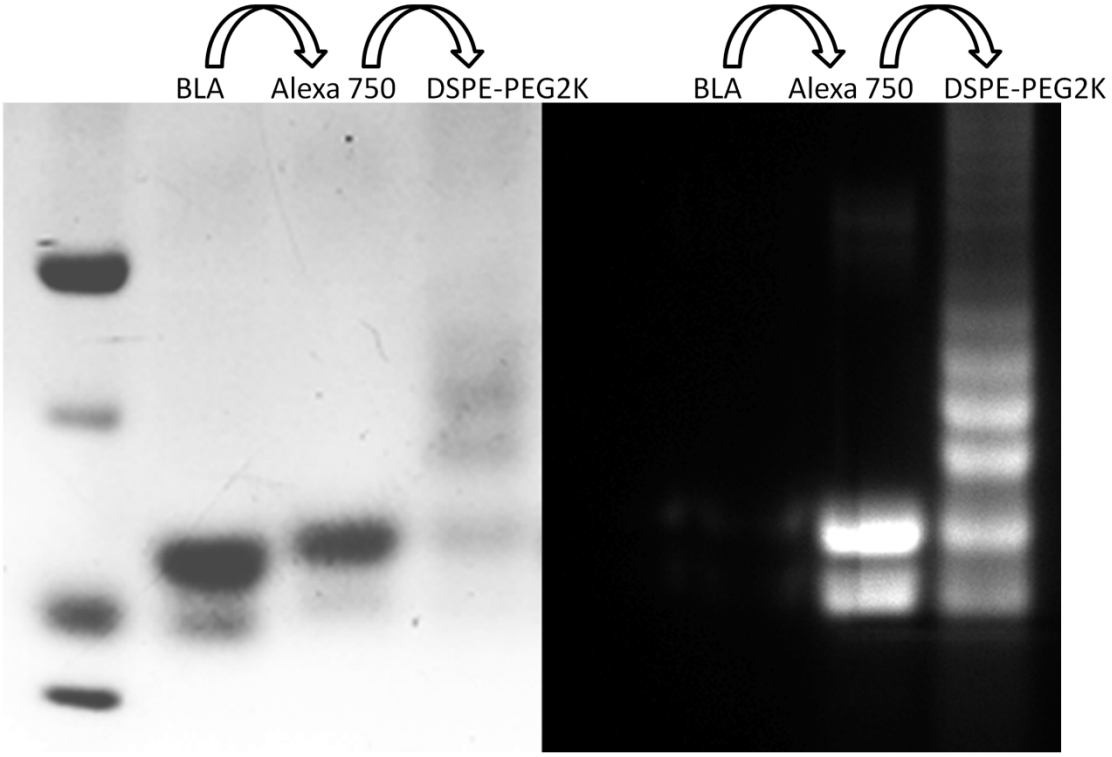

Figure 4.5 Labeling of BLA with Alexa Fluor 750 and DSPE-PEG(2000)-Mal. Using the optimal conditions identified, BLA was labeled first with a near-infrared fluorophore, and subsequently with a lipid.

4.3.2 Incorporation of BLA-Lipid Conjugate into Liposome Membranes

Reverse-phase evaporation vesicles (REV) containing the membrane-bound enzyme were fabricated with slight modifications to published procedures[199] (detailed protocol in methods section). This emulsion-based method resulted in a high entrapment efficiency of enzymes as well as cavitation nucleation sites in the liposome vesicles. β-lactamase was labeled with Alexa 750 to allow tracking of the enzyme by fluorescence microscopy. Even without conjugation of the enzyme to a phospholipid, β-lactamase was incorporated and soluble in the aqueous volume of the liposomes (figure 4.6a). However, only the lipid conjugates efficiently partitioned into the liposome membrane, as evidenced by fluorescent microscope images (figure 4.6b). Although the hydrophobic portion from the lipid comprises only a small fraction of the conjugate, it was enough alter the enzyme solubility, and make it lipophilic. Enzymes with no lipids were

uniformly contained within the aqueous volume, resulting in a sphere, brightest at the center where it is the "thickest". In contrast, enzyme-lipid conjugates stained the lipid membrane, creating a bright ring characteristic of liposomes whose membranes have been fluorescently labeled.

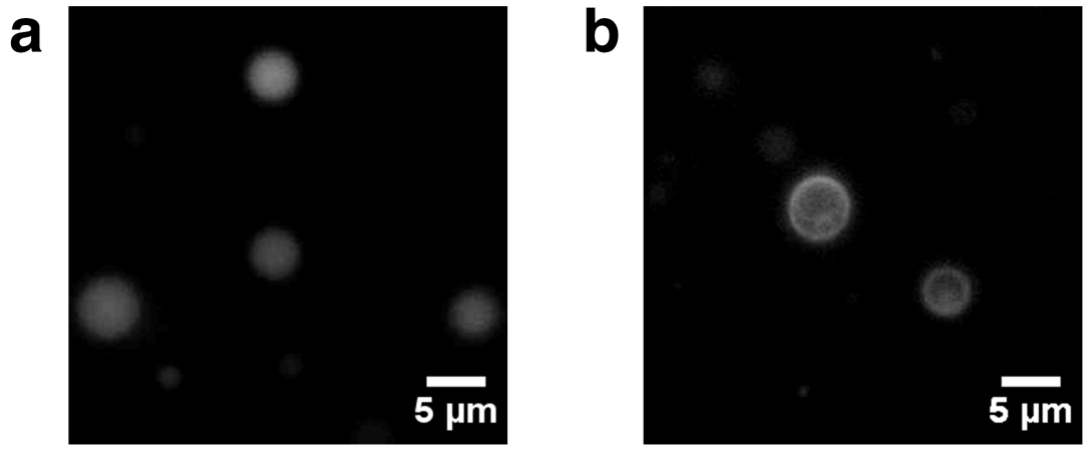

Figure 4.6 Incorporation of β-lactamase inside liposomes. β-lactamase was fluorescently labeled with Alexa Fluor 750 to visualize its location within liposomes by standard fluorescent microscopy. a) The labeled enzyme was incorporated in REV. The diffuse fluorescent spheres display the lack of visible partitioning of the enzyme within the lipid membrane, instead showing the brightest fluorescent region at the center of the spheres, corresponding to the thickest region. b) Incorporation of β-lactamase conjugated to DSPE-PEG2000 resulted in efficient partitioning of the conjugate in the liposome membrane, resulting in an image strongly resembling membrane dyed liposomes. Rupture of both structures in a) and b) result in an enzyme exposure and an increase in activity, but rupture of the structure in b) produces enzyme-containing membrane fragments which are more likely to remain localized to the site of rupture.

One underlying aspect of this approach is that the liposomes which have not been subjected to ultrasound do not have exposed β-lactamase, but should instead have an asymmetric distribution of the enzyme on the inner leaflet of the lipid bilayer. By virtue of the liposome preparation method, it was thermodynamically favorable for the enzyme-lipid conjugates to face the inside of the liposome. Still, there were outward-facing enzymes which needed to be removed. To accomplish this, two strategies were pursued, depending on which conjugate was incorporated. For the reducible conjugate, treatment with a membrane impermeable reducing agent such as TCEP detached exposed enzyme, while ensuring that inward facing enzymes

remained membrane bound. For the non-reducible conjugate, Proteolytic degradation of exposed enzyme by a protease such as Proteinase K again removed the catalytic portion of outward facing enzymes, while sparing inward facing enzymes due to impermeability of enzymes through the lipid bilayer.

It is also possible that the remaining attached protein fragments contain an immunogenic portion, so that although the catalytic site has been destroyed, the liposomes are not shielded from immune recognition. Immunization experiments will be required to determine if this is an issue going forward. The reducible conjugate solves this problem by allowing the removal of the enzyme and leaving only a thiol-terminated PEG. These thiolated lipids may be subject to dimerization. However, even if that is the case, we have seen no evidence of liposome destabilization after exposure and removal of the reducing agent.

Before rupture with US, UREAL still retained a low activity, presumably due to remaining exposed enzyme, or a non-negligible diffusion of the assaying substrate (nitrocefin) across the liposome bilayer to the internal enzymes. Unlysed liposomes displayed a lower activity when assayed with the substrate CCF2-FA, which is presumed to be membrane-impermeant. Thus, the ratio of increase in enzyme activity was greater with this substrate, and is more representative of the performance of an intended membrane-impermeant prodrug. Lysis of UREAL by US resulted in a 15.8-fold increase in activity (Figure 4.7a) and a 22.4-fold increase when lysed with a chemical detergent. Higher activity from detergent lysis compared to US lysis could be due to a more complete lysis of the liposomes, or a greater exposure of the enzyme-lipid conjugates in the micellar state, however, the detergent also increased the activity of untreated BLA. . Ultrasound-induced lysis likely produced reformed liposomes containing hidden enzyme.

A clinically relevant high-intensity focused ultrasound (HIFU) transducer was employed to trigger enzyme exposure. Although the acoustic power was significantly higher than those used in diagnostic applications, the intensity was similar to those used in clinical scanners, and was

below the mechanical index limit of 1.9. Activity increased 4.9-fold with the application of focused ultrasound at a peak negative pressure (PNP) of 2.7 MPa, with a strong dependence on applied pressure. Consistent with previous experimental results using ultrasound-ruptured liposomes, it was necessary to exceed the cavitation threshold to cause liposome rupture and payload exposure. At a PNP of 1.2 MPa, the activity was still very close to the background level, indicating minimal enzyme exposure. However, by increasing the PNP to 1.8 MPa, the cavitation threshold was exceeded, which resulted in nearly 3-fold amplification of activity. Although cavitation in high doses can be detrimental to the function of enzymes[214, 215], the amount of cavitation required to rupture liposomes was low enough to preserve much of the enzyme's activity.

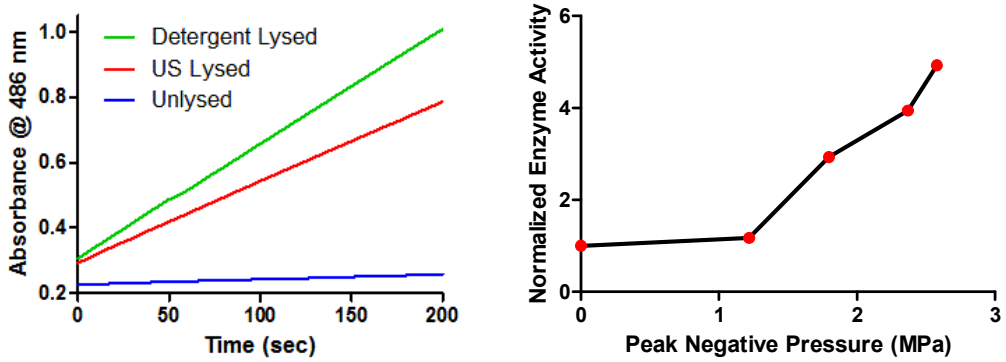

Figure 4.7 β-lactamase exposure by ultrasound to increase activity. a) The activity of UREAL, both untreated, and exposed to ultrasound was assayed using Nitrocefin. The rate at which the absorbance at 486 nm increases is proportional to the activity. Lysed UREAL showed a 15-fold higher activity than the untreated sample. b) A clinically relevant focused ultrasound transducer was used to trigger the exposure of enzyme. A threshold was observed between 1.2 and 1.8 MPa where cavitation began to occur.

4.3.3 Strategies for Ultrasound Operation

Once granted the ability to selectively expose enzyme at the correct time and place, multiple operating protocols can be envisioned. In one scheme, UREAL can be ruptured shortly after IV administration, to cause membrane deposition and enzyme exposure as they travel

through the tumor microvasculature. A continuous, pulsed application of US can lead to the constant accumulation of membrane fragments. A hidden ligand or adhesion molecule can also be exposed to enhance the retention of enzymes at the site of rupture. The efficiency of local retainment will not be 100%, which will result in exposed enzyme continuing to circulate instead of remaining localized. This will necessitate a waiting period to allow clearance of the exposed enzyme from the bloodstream, after which the prodrug can be administrated. The majority of liposomes which continue to circulate will ultimately accumulate in the spleen or the liver. If their clearance is more rapid than those at the tumor site, it may also be beneficial to further delay prodrug administration.

In a second scheme, UREAL can be allowed to accumulate passively through the enhanced permeation and retention (EPR) effect, or due to the attachment of a cancer-specific targeting ligand. In this scheme, the purpose of the US will be mainly to spatially control the exposure of enzyme, rather than to further concentrate the enzyme. Before rupture, UREAL will be unable to convert a membrane-impermeant prodrug[216, 217], which will limit the production of active drug in regions of off-target accumulation and cell uptake, such as the liver and spleen. Once accumulated, a brief pulse of US will rupture the accumulated UREAL, and create an active environment for incoming prodrug. The US could be applied immediately before or after administration of the prodrug.

Either scheme allows the enzyme to be hidden from the immune system while travelling to the tumor location. However, in the first scheme, since the enzymes will be exposed in the tumor for an extended duration, they could be prone to immune recognition, degradation, or antibody neutralization, all of which could be detrimental to the enzyme function. Such an outcome is a more likely concern for repeated treatments, which will have to overcome a mounting antibody response. In the second scheme, since the enzyme can be exposed near the time of prodrug administration, it is only necessary for the enzyme to remain active for the in

vivo lifetime of the prodrug. Thereafter, an immunostimulatory response localized to the tumor region has the potential to be beneficial to the patient[218].

4.4 Methods

4.4.1 Enzyme Labeling and Bioconjugation Protocols

Fluorescent labeling of β-Lactamase

12.5 mg BLA (13.8% protein – 1.725 mg) were dissolved in 862 µL HEPES buffer (50 mM pH 8.0; final enzyme concentration was 72 µM). 15.5 µL of BODIPY-FL (Life Technologies, Carlsbad, CA) of a 10 mM stock solution in DMSO was added (final BODIPY-FL concentration was 180 µM, 2.5 equivalents) and the solution was kept at room temperature in the dark overnight. The solution was then loaded on an ion exchange column (600 mg of Sephadex G-25) and eluted with HEPES buffer 50 mM pH 8.0.The orange color fraction was collected (1.2 mL) and the enzyme concentration in it was determined to be 50 µM (measured by UV absorption). This procedure results in an average of 2.1 BODIPY-FL molecules per enzyme.

Conjugation of lipid to fluorescently labeled BLA – sequential conjugation

3 microcentrifuge tubes were charged with 200 µL of the purified enzyme from the above procedure (50 µM in HEPES buffer 50 mM pH 8.0). Traut's reagent (TR) solutions of 2.5, 5 and 10 mM in DMSO were prepared. 10 µL from the TR solutions were added to the enzymes to make 2.5, 5 and 10 equivalents of TR to enzyme (final TR concentrations are 125, 250 and 500 µM for 50 µM of enzyme). The solutions were kept at room temperature in the dark for 2 hours. Then, 40 µL from 2.5, 5 and 10 mM solutions of DSPE-PEG_{2000}-PDP (Quanta Biodesign, Powell, OH) in DMSO were added to make 4 equivalents lipid to TR in each sample. Each reaction was then diluted with 200 µL HEPES buffer (50 mM pH 8.0) and kept at room temperature in the dark for 18 hours.

Conjugation of lipid to fluorescently labeled BLA – concerted conjugation

2 microcentrifuge tubes were charged with 150 µL of purified enzyme from the above procedure (50 µM in HEPES buffer 50 mM pH 8.0). Traut's reagent (TR) solutions of 2.5 and 5 mM in DMSO were prepared. DSPE-PEG_{2000}-PDP (Quanta Biodesign, Powell, OH) solutions of 2.5 and 5 mM in DMSO were prepared.

10 µL from the 5 mM and 8 µL from the 2.5 mM TR solutions were added to the enzymes to make 6 and 2.5 equivalents of TR to the enzyme solutions (respectively). Immediately following, 30 µL of either 5 or 2.5 mM DSPE-PEG_{2000}-PDP in DMSO was added, generating 4 equivalents of lipid to TR in each sample. The solutions were diluted with 150 µL HEPES buffer 50 mM pH 8.0 to lower DMSO content to 12%. The reactions were kept at room temperature in the dark for 18 hours.

Purification of fluorescently labeled BLA-lipid conjugates

All samples were loaded on an ion exchange resin (600 mg Sephadex G-25) and eluted with MOPS buffer 50 mM pH 7.4. The orange colored fraction was collected. The final enzyme concentration in solutions was adjusted to 20 µM (measured by UV absorption)

Lipid conjugation to BLA (not fluorescently labeled)

4.5 mg BLA (13.8% protein, 0.626 mg) was dissolved in 420 µL HEPES 50 mM pH 8.0 (final BLA concentration 50 µM). A 10 mM stock solution of TR and 20 mM stock solution of DSPE-PEG_{2000}-PDP in DMSO were prepared. To the protein solution was added 14.7 µL from TR stock and 30 µL from DSPE-PEG_{2000}-PDP stock solutions (final concentrations are: 50 µM BLA, 350 µM TR and 1.4 mM DSPE-PEG_{2000}-PDP). The reaction was kept at room temperature for 18 hours, then, loaded on an ion exchange resin (600 mg Sephadex G-25) and eluted with MOPS 50 mM pH 7.4. Fractions of 0.5 mL were collected and UV absorption of each fraction was measured to determine enzyme content. Fractions 3 and 4 contained the enzyme.

4.4.2 Preparation of UREAL

3.6 mg DSPE-mPEG(5000) (Laysan Bio, Inc., Arab, AL) dissolved in chloroform was added to a 1.5 mL microcentrifuge tube. The chloroform was evaporated by applying a gentle argon stream while vortexing the open vial, leaving a lipid film on the walls. To this tube, 800 µL PBS (GIBCO, Bethesda, MD) was added, and the tube was vortexed for 1 minute. To break up the lipids into small micelles, a Misonix XL-2000 (Farmingdale, NY) probe type sonicator was operated at level 10 in the liquid, near the bottom of the tube for five 1 second pulses. This solution was set aside.

2.48 mg Egg-PC and 1.24 mg Cholesterol (Avanti Polar Lipids, Inc., Alabaster, AL) dissolved in chloroform were combined in a 4 mL glass flat-bottom vial. The chloroform was evaporated again with the vortex argon stream method. After removing the chloroform, 1 mL of diethyl ether was added, and the vial was vortexed gently for 3 seconds to dissolve the lipids. 300 µL of an aqueous solution containing BLA or DSPE-PEG(2000)-BLA were added to the bottom of the vial to make a solution of the two immiscible phases. The aqueous solutions used were always adjusted to pH 7.4 and to be isotonic with PBS to prevent osmotic shock.

The tip of a PowerGen 125 Homogenizer (Fisher Scientific, Pittsburgh, PA) was lowered to the bottom of the vial, and was operated on high speed for 1 minute. This created a stable water-in-ether emulsion. The vial was taken immediately to a rotary evaporator and attached by means of a screw-thread adapter. The vial was rotated at a constant 200 rpm and the vacuum pump pressure was set to -18 inHg. After 20 minutes, the solution began to gel as the ether was almost completely removed.

To the emulsion gel, the PBS solution containing DSPE-mPEG(5000) was added, and the vial was vortexed on the lowest speed for 1 minute. The vial was then placed under a gentle argon stream for 5 to 10 minutes to remove most of the remaining ether. This separated the closely packed emulsions and completed the liposome formation. The resulting liposomes were about 1-5

microns in size and were expected to be multilamellar and multivesicular in structure. To reduce liposome size, the solution of giant liposomes was extruded through track-etched polycarbonate membranes (Whatman, Maidstone, UK) with the appropriate pore diameter. The liposomes were then dialyzed against DPBS using the Fast SpinDialyzer (Harvard Apparatus, South Natick, MA) for 12 hours, which allowed the use of large pore membranes for the efficient removal of the free nanoparticles.

4.4.3 Removal of Outward-Facing BLA by Proteolytic Degradation or Chemical Cleavage

In the case of UREAL prepared with the cleavable DSPE-PEG(2000)-SS-BLA conjugate, incubation with a reducing agent was able to detach the enzyme from the membrane incorporated lipid. tris-(2-carboxylethyl)-phosphine (TCEP) (Sigma, St. Louis, MO) was utilized as a reducing agent as opposed to DTT, because it is membrane impermeant which prevented cleavage of the encapsulated BLA conjugate. UREAL prepared with the non-cleavable DSPE-PEG-BLA conjugate were incubated overnight with 0.2 mg/mL Proteinase K (Sigma, St. Louis, MO) at 37°C to digest exposed enzymes. The inward-facing BLA molecules were protected, since Proteinase K is a large polar enzyme which was not able to access the liposome interior. For both methods, dialysis with large pore membranes was used to remove reducing agent and free BLA, or Proteinase K and BLA fragments.

4.4.4 BLA Exposure by UREAL Lysis

To expose BLA hidden on the inner leaflet of the UREAL, liposomes were lysed with focused US. 2 mL aliquots of the diluted liposomes were loaded into standard disposable transfer pipettes (ThermoFisher Scientific, Waltham, MA). An H-102 ultrasound transducer (Sonic Concepts, Bothell, WA), with a center frequency of 1.1 MHz and focal length of 62.6 mm was placed in a water bath heated to 37°C. The pipets were held by a clamp, so that the bottom of the

bulb was in the center of the transducer alignment cone. The water bath level was adjusted to be at least as high as the liquid in the pipet. The 2 mL volume contained in the pipet filled the sample up to a height > 1.5 cm above the transducer focus. Samples were allowed to equilibrate with the bath temperature for 2 minutes prior to insonation. A PCI-5412 (National Instruments, Austin, TX) arbitrary waveform generator produced a 303 μsec pulse (1000 cycles) sine wave at 3.3 MHz, the 3rd harmonic of the transducer. The pulse was repeated continuously at a 1 or 10% duty cycle. The gain was adjusted on a 300 W amplifier (Vox Technologies, Richardson, TX) along with the voltage output level from the waveform generator to produce a peak negative pressure of 2.3 MPa.

As positive controls, liposomes were also lysed by probe sonication, or by exposure to a detergent. For probe sonication, 300 μL of UREAL was placed in a 1.5 mL microcentrifuge tube. A Misonix XL-2000 (Farmingdale, NY) probe was lowered to just above the bottom of the tube and was pulsed 5 times for 0.5 seconds at level 2. For detergent lysis, an aliquot of a solution of *n*-Octyl-β-D-glucopyranoside (Sigma, St Louis, MO) (100 mg/mL in PBS) was diluted 10X with UREAL to achieve a final detergent concentration of 10 mg/mL, or 1% w/v. Since the presence of detergent can affect enzyme activity, enzyme + detergent controls were included in activity measurements to account for this effect.

4.4.5 BLA Activity Assay with Nitrocefin and CCF2-FA

BLA activity of UREAL samples were measured before and after the application of ultrasound, and lysis with detergents. A chromogenic substrate, nitrocefin (EMD Millipore, Billerica, MA), was used to quantify activity by monitoring the absorbance increase over time at 486 nm with an Infinite 200 Pro microplate reader (Tecan, Mannedorf, Switzerland). The samples being tested were typically diluted 10-100X to allow time for the measurement before conversion of a majority of the substrate. A non-negligible rate of diffusion of nitrocefin through liposome

membranes resulted in a higher activity, especially for unlysed samples. A FRET-based fluorogenic substrate, CCF2-FA (Life Technologies, Carlsbad, CA) was also used as an independent activity assay. Cleavage of the link between the donor and acceptor resulted in increased donor (coumarin) fluorescence at 447 nm, and decreased FRET to the acceptor (fluorescein) at 518 nm. For both wavelengths, fluorescence was excited with 409 nm and read continually for 20 minutes.

4.5 Conclusions

The enzyme delivery system developed here has the potential to address the key drawbacks of previous approaches in field of enzyme prodrug therapy, specifically the lack of immune evasion and specificity of enzyme delivery. The asymmetrically-loaded liposome contains the necessary components for effective in vivo transport and protection, as well as the biomimetic structure of phospholipid membrane-bound proteins for incorporation within endothelial walls. Focused ultrasound triggered release enables site-specific activation needed to increase the therapeutic index and limit toxicity to other accumulation sites. The results discussed here have prepared these structures for validation in animal models.

4.6 Acknowledgements

This chapter, in part, is being prepared for submission for publication as Benchimol, Michael; Weinstain, Roy; Ibsen, Stuart; Simberg, Dmitri; Tsien, Roger; Esener, Sadik. “Ultrasound-Directed Exposure of Asymmetric Beta-lactamase Liposomes”.

4.7 References

205. Choi, C.H., Alabi, C.A., Webster, P. & Davis, M.E. Mechanism of active targeting in solid tumors with transferrin-containing gold nanoparticles. *Proc Natl Acad Sci U S A* **107**, 1235-1240 (2010).

206. Chung-Faye, G. et al. Virus-directed, enzyme prodrug therapy with nitroimidazole reductase: a phase I and pharmacokinetic study of its prodrug, CB1954. *Clinical cancer research : an official journal of the American Association for Cancer Research* **7**, 2662-2668 (2001).

207. Harding, F.A. et al. A beta-lactamase with reduced immunogenicity for the targeted delivery of chemotherapeutics using antibody-directed enzyme prodrug therapy. *Mol Cancer Ther* **4**, 1791-1800 (2005).

208. Bagshawe, K.D., Sharma, S.K., Springer, C.J. & Rogers, G.T. Antibody directed enzyme prodrug therapy (ADEPT). A review of some theoretical, experimental and clinical aspects. *Ann Oncol* **5**, 879-891 (1994).

209. Bagshawe, K.D. Targeting: the ADEPT story so far. *Curr Drug Targets* **10**, 152-157 (2009).

210. Nishikawa, M. & Huang, L. Nonviral vectors in the new millennium: delivery barriers in gene transfer. *Human gene therapy* **12**, 861-870 (2001).

211. Napier, M.P. et al. Antibody-directed enzyme prodrug therapy: efficacy and mechanism of action in colorectal carcinoma. *Clinical cancer research : an official journal of the American Association for Cancer Research* **6**, 765-772 (2000).

212. Sabath, L.D. & Finland, M. Resistance of penicillins and cephalosporins to beta-lactamases from Gram-negative bacilli: some correlations with antibacterial activity. *Annals of the New York Academy of Sciences* **145**, 237-247 (1967).

213. Vrudhula, V.M., Svensson, H.P. & Senter, P.D. Cephalosporin derivatives of doxorubicin as prodrugs for activation by monoclonal antibody-beta-lactamase conjugates. *Journal of medicinal chemistry* **38**, 1380-1385 (1995).

214. Ozbek, B. & Ulgen, K.O. The stability of enzymes after sonication. *Process Biochemistry* **35**, 1037-1043 (2000).

215. Coakley, W.T., Brown, R.C. & James, C.J. The inactivation of enzymes by ultrasonic cavitation at 20 kHz. *Archives of Biochemistry and Biophysics* **159**, 722-729 (1973).

216. Wu, W. et al. Targeting cell-impermeable prodrug activation to tumor microenvironment eradicates multiple drug-resistant neoplasms. *Cancer research* **66**, 970-980 (2006).

217. Heine, D., Muller, R. & Brusselbach, S. Cell surface display of a lysosomal enzyme for extracellular gene-directed enzyme prodrug therapy. *Gene therapy* **8**, 1005-1010 (2001).

218. Dilber, M.S. et al. Gap junctions promote the bystander effect of herpes simplex virus thymidine kinase in vivo. *Cancer research* **57**, 1523-1528 (1997).

Chapter 5:

Ultrasound-Triggered Propulsion of Perfluorocarbon-Loaded Microbullets for Targeted Tissue Penetration

Abstract

Precise control over the physical interaction of particulates with biological systems can have a great impact in in vitro diagnostics and in vivo intracellular delivery. In order to produce a high enough level of energy to provide a practical motion, existing structures are fueled by biochemical or electrochemical environments which are not representative of the biological context. To avoid the dependence on fuels which often cytotoxic and restrict the use to in vitro applications, we have developed a propulsion system based on an on-board fuel system independent of chemical properties. Acoustic droplet vaporization of perfluorocarbon emulsions loaded into tapered tubular structures provides the necessary force for these "microbullets" to penetrate, cleave, and deform cellular tissue for potential targeted drug delivery and precision nanosurgery. The microbullets have an inner Au layer that allows conjugation of a monolayer of thiolated cysteamine (green in picture) for electrostatic attachment of perfluorocarbon droplets (purple droplets). A sandwiched layer of Ni allows for external magnetic control, which potentiates orientation of the microbullets for directed propulsion.

5.1 Introduction

Recent advances in micro/nanomachines have shown great promise in diverse fields[219-231]. A wide variety of chemically powered and magnetically propelled micro/nanoscale machines have been developed for specific biomedical applications ranging from lab-on-chip bioanalytical devices to site-specific drug delivery targeting. However, these micro/nanomachines lack the power and biocompatibility necessary for penetrating tissue and cellular barriers, for in vivo cargo delivery and precision nanosurgery.

Prevalent micro/nanomachine designs typically require conversion of external chemical energy, harvested from the vicinity of the machines, to promote autonomous propulsion. Several mechanisms have been developed to realize such micro/nanomachine thrust in connection to hydrogen peroxide fuel; these mechanisms include self-electrophoresis,[221, 223] self-

diffusiophoresis,[220] and bubble propulsion[225, 230, 232]. To enhance biocompatibility several groups have also explored fuel-free micro/nanomachine propulsion mechanisms, including the utilization of electrical power (i.e., diode nanowires)[233] and magnetic actuation[234-236]. Despite the inherent advantages of such externally propelled micro/nanoscale locomotion schemes, these propulsion mechanisms do not possess the thrust needed for penetrating tissue barriers and cellular membranes[237].

Herein we present a highly efficient microscale propulsion technique that utilizes ultrasound (US) to vaporize biocompatible fuel (i.e., perfluorocarbon (PFC) emulsions) bound within the interior of a micromachine for high-velocity, bullet-like propulsion. Such remarkable micro/nanomachine thrust is sufficient for deep tissue penetration and deformation. An increase in enthalpy, which accompanies vaporization, results in energy transfer. Momentum, geometrically focused by virtue of the micromachine structure, generates projectile motion. Thus, instead of creating a device that can convert a chemical fuel, we have produced a micromachine with an on-board fuel source that is capable of releasing energy as a response to an external stimulus independent of its surrounding environment as a response to an external stimulus.

Recently, gas and liquid PFC particles have received considerable attention owing to their biocompatible nature for intravenous injection and subsequent destruction upon ultrasound irradiation[238, 239]. The decreased solubility and low diffusion coefficient of these droplets and bubbles lengthens blood circulation before an incident US wave is used to induce their destruction or cavitation[240]. PFC microbubbles or emulsions are thus extremely attractive for diverse biomedical applications, such as externally triggered site-specific drug and gene delivery capsules[157, 241], molecular imaging agents[242-244], phase change contrast agents[245, 246], and blood substitutes[246-248]. However, we are unaware of earlier reports on using PFCs as an integrated fuel source for micro/nanomachine propulsion.

Similar to the externally triggered explosion experienced within a gun barrel to propel a bullet[249], these micromachines, named herein microbullets (MB), utilize for propulsion the rapid

expansion and vaporization of perfluorocarbon droplets[250] that are electrostatically bound within the machine interior and triggered by an US pulse (i.e., acoustic droplet vaporization (ADV))[178, 179]. These new US-triggered, PFC-loaded microbullets can travel at remarkably high average velocities (ca. 6.3 m s^{-1}) over 100 times faster than the micromachines published to date)[219, 226, 227, 230] and deeply penetrate and deform kidney tissue. The concomitance of powerful MB propulsion, biocompatible PFC emulsion fuel[251], and deeply penetrative, yet medically safe US[252] could lead to highly targeted in vivo drug delivery, artery cleaning, gene regulation schemes, and cancer therapeutics that require higher specificity and accuracy than the current state-of-the-art.

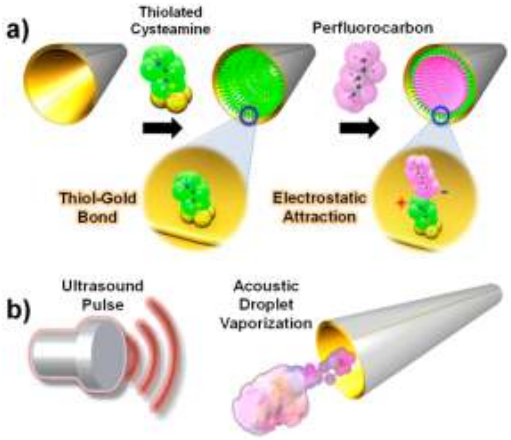

Figure 5.1 Ultrasound-triggered microbullets (MB). a) Preparation of the PFC-loaded MBs: nanofabricated MB (left), the conjugation of thiolated cysteamine to the inner Au layer of the MB (middle), electrostatic binding of the anionic PFC emulsion to the cysteamine-functionalized surface (right). Insets show magnified views of cysteamine (left) and cysteamine electrostastically bound to PFC (right). **b)** Schematic illustration of microbullet propulsion through acoustic droplet vaporization of the bound PFC triggered by an ultrasound pulse.

5.2 Results and Discussion

The choice of the specific PFC compounds is also crucial as their chemical properties have a profound effect upon the efficiency of the ADV process and hence upon the resulting propulsion performance. PFC compounds with a low boiling point, such as perfluoropropane and perfluorobutane, are stable in the gaseous state and have been extensively used for the production of microbubbles for contrast-enhanced US imaging[253]. PFC compounds with a higher boiling

point exist as liquids or solids, but two particular molecules, perfluoropentane (PFP; bp 29°C at 1 atm) and perfluorohexane (PFH; bp 56 °C at 1 atm) are liquid PFC compounds that can also persist in the gaseous state – an important property for ADV[198]. Thus, in the work described herein, we distinctly functionalize micromachines with both PFH and PFP to optimize the US-triggered propulsion strategy.

A three-step fabrication strategy (Figure 1), including nanofabrication, cysteamine functionalization, and PFC emulsion binding, was utilized for preparing the US-triggered MBs. Large MBs (length ca. 40 μm) were created by using rolled-up thin-film nanofabrication techniques[225, 227], while for fabrication of small MBs (length ca. 8 μm) membrane-template electrodeposition was utilized (see methods section)[232]. An embedded Ni layer facilitates magnetic washing and experimental alignment of the MBs before US pulsing to facilitate directed, linear motion during propulsion. The inner Au layer of these microtubes permits cysteamine monolayer conjugation for electrostatic attachment of PFC droplets. The slightly tapered conical structure of the MBs, owing to the angled physical vapor deposition fabrication process[225, 227], directs thrust from ADV while an embedded magnetic layer permits externally guided, magnetic alignment for precision steering.

To initiate this study, emulsion droplets of PFH (bp 56°C)[198], were utilized because they maintain stability under physiological conditions but enable ADV upon arrival of incident US pressure waves. Moreover, the emulsion composition was designed to have efficient matching of intermolecular forces between the PFC and the surfactant; the matching of the forces is necessary to reduce interfacial tension and facilitate the conversion of nanoscale droplets. To illustrate the selective PFH-droplet immobilization strategy developed herein, fluorescently tagged PFH emulsions, stabilized by a negatively charged surfactant, were electrostatically immobilized onto the cysteamine-modified inner gold surfaces (Figure 2). The exposed amino group (pK_a 8.6) of the cysteamine[254] is positively charged for the prescribed experimental settings (i.e., pH range 7.4-8.0) and thus electrostatically binds to emulsions stabilized with an anionic phosphate

fluorosurfactant (pK_a 7.2). Emulsions were strongly negative with a measured zeta potential of 46 mV in phosphate-buffered saline. A graphical representation of the emulsion size distribution (mean= 304.9 nm, polydispersity index = 0.144) and stability is shown in Fig. 5.10 and Fig. 5.11.

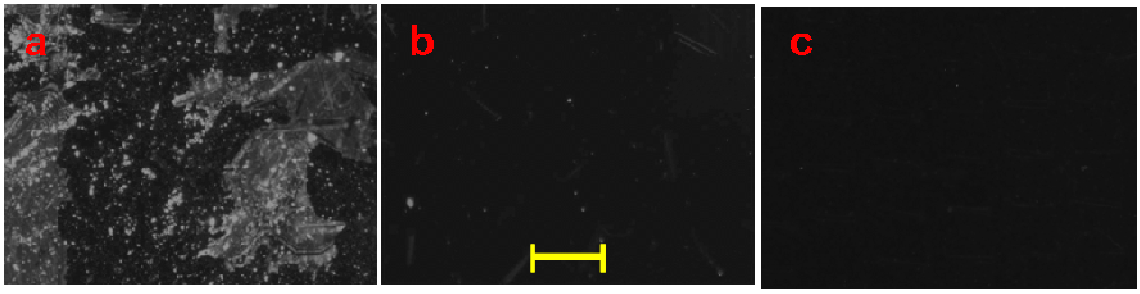

Figure 5.2 Images depict the specific binding of fluorescent emulsion particles to a Au sputtered silicon wafer containing rolled up MBs. (a) Depicts the electrostatic binding of the anionic emulsions to the free amine on the Au surface when compared to samples without cysteamine incubation (b) and without emulsion (c). Scale bar, 200 μm.

Initial US-triggered propulsion experiments reveal PFH emulsion vaporization originating from within the MBs (Figure 3a). A vaporized emulsion (i.e., bubble) extending out of the tail of the MB is clearly visible after the US pulsation (Figure 3a, right), thereby corroborating the assumption that formation of microscale gaseous bubbles is the result of sudden US-triggered, PFH droplet vaporization. The rapid emulsion expansion during the vaporization process (ca. 5-fold radial)[239] provides a sudden impulse that projects the MB out of the microscope field of view within an extremely short single image frame (ca. 55.6 μs). Control experiments over a longer period demonstrate that nonspecific adsorption of PFH was negligible as MBs functionalized without cysteamine (Figure 3c) or without the PFH emulsion failed to produce bubbles or MB movement. US pulsations therefore have minimal effect on the locomotion of nonfunctionalized MBs.

The movement of the MBs were analyzed over a series of frames (Figure 3b) in which the MB travels 350 μm from its initial location within 55.6 μs upon vaporization of the PFH emulsion (Figure 3b (left), dotted circle) triggered by an US pulse signal. Therefore, the MB traveled at a

remarkably high average velocity of 6.3 m s^{-1}, which corresponds to an ultrafast relative velocity of over 158,000 body lengths s^{-1}. The MB dynamics were analyzed with Stokes' law and experimental image analysis. The initial MB velocity (56.9 m s^{-1}), kinetic energy (0.764 nJ), and momentum (2.69×10^{-11} N s) were calculated with Equations (1)-(3) in conjunction with MB parameter values presented in Table 5.1.

$$v_0 = \frac{\Delta d}{\frac{m}{k}\left(1 - \frac{m}{k} e^{-\frac{k\Delta t}{m}}\right)} \tag{1}$$

$$E_k = \frac{1}{2} m v^2 \tag{2}$$

$$p_0 = m v_0 \tag{3}$$

where k is the drag coefficient for a cylinder, m (kg) is the mass of the hollow MB , Δd (m) is the distance traveled, t (s) is time, and E_k (J) is the kinetic energy. The remarkably high initial and average MB velocities associated with US-triggered emulsion vaporization compare favorably with velocities achieved for stochastically moving microparticles propelled by water cavitation[255].

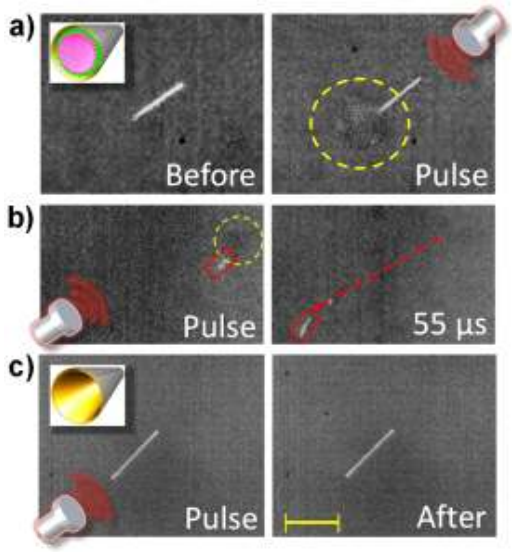

Figure 5.3 a) Still frame images illustrating the formation of a bubble cloud from the tail of a PFH-loaded MB upon firing of an US pulse signal. **b)** The trajectory (dotted arrow; right) of a PFH-loaded microbullet is imaged 55 µs after an (left) US pulse signal. A dotted circle accents the emerging vaporized PFH while boxes highlight the location of the MB. **c)** A MB incubated with PFH emulsion but not conjugated with cysteamine displays no emulsion expansion nor movement after a US pulse signal. Inset images show the (a) PFH-loaded MB and the (c) control MB (i.e. without cysteamine) while the US icon represents a US-triggered pulse signal (44 µs, 1.6 MPa). The images were obtained at a frame rate of 18,000 frames per second (fps) using a 40X objective. Scale bar, 40 µm (a,c) and 120 µm (b).

To promote highly efficient, single-shot, and controllable MB firings, the US trigger settings (i.e., transducer pressure and pulse length) and MB fabrication (i.e., size, shape, thickness) were optimized at distinct settings. The combination of low pressure (1.6 MPa)/medium pulse length (44 µs) and high pressure (3.8 MPa)/short pulse length (4.4 µs) produced efficient linear MB locomotion from ADV without external water cavitation, while other combinatorial changes in pulse pressure and length produced water cavitation and/or sporadic MB movement (Fig. 5.7, Fig. 5.8).

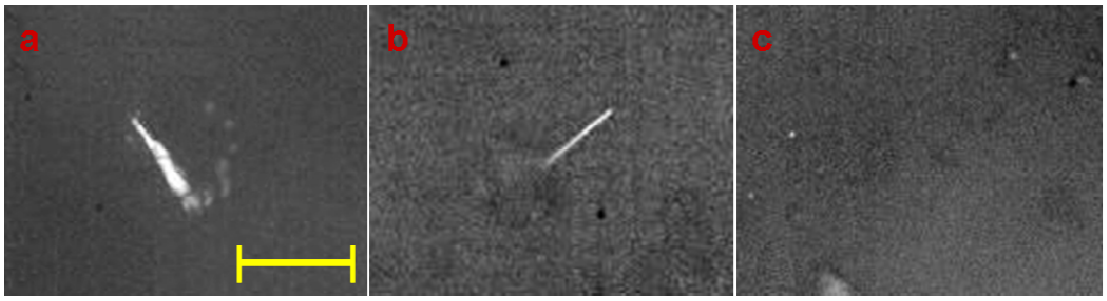

Figure 5.4 Still frame images (frame time: 1/18000 s) displaying three distinct bubble emissions from the MBs modified with PFH emulsion after different US pulses. Bubble emission patterns include (a) streaming bubbles that generally cause spinning MB motion after a long (444 µsec)),/low pressure (1.6 MPa) pulse, (b) optimal bubble formation that propels MBs in a semi-linear trajectory medium pulse (44 µsec))/low pressure (1.6 MPa), and (c) diverse bubble formations that are associated with general water cavitation and are not associated with perfluorohexane emulsions long pulse (>=44 µsec))/high pressure (3.8 MPa).

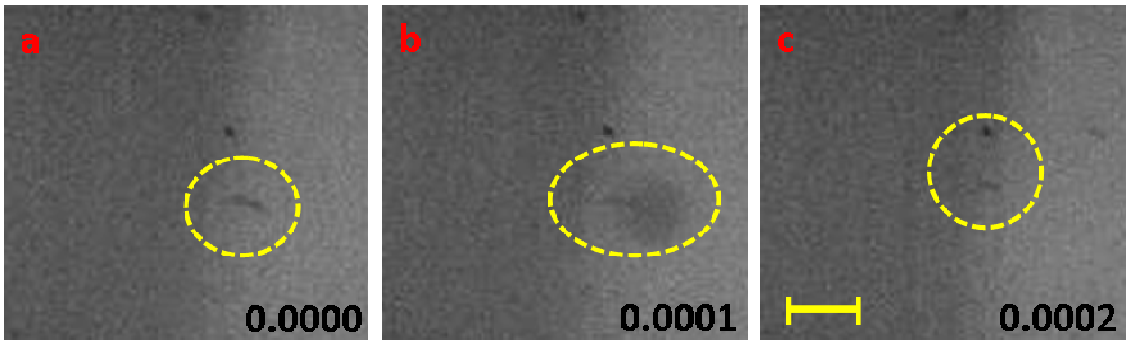

Figure 5.5 Figure depicts the before (a), during (b) and after (c) images of an MB piercing lamb kidney tissue after a short 4.4 µsec, 3.8 MPa US pulse. A dotted yellow circle is added to help track the position of the MB during locomotion. Images were captured sequentially at a frame rate of 10,000 fps. Scale bar, 60 µm while black numbers are time (s).

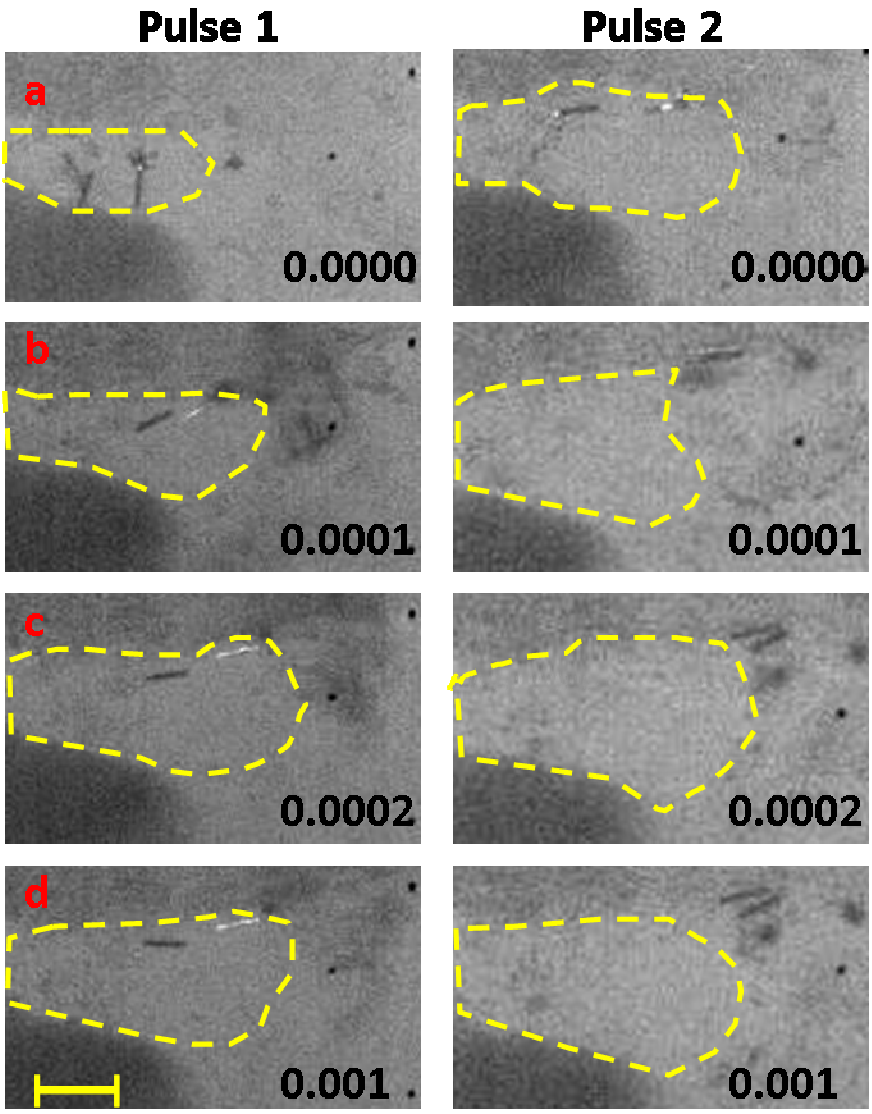

Figure 5.6 Images depict the power of multiple MBs and their ability to drastically increase the opening of a tissue after two short 4.4 µsec, 3.8 MPa US pulses. Sequential images with yellow accented lines show the effect of the MB's on the tissue opening before (a), during (b-c) and after the tissue recoiled (d) for each pulse. Images were taken at a frame rate of 10,000 fps. Scale bar = 60 µm while black numbers are time (s).

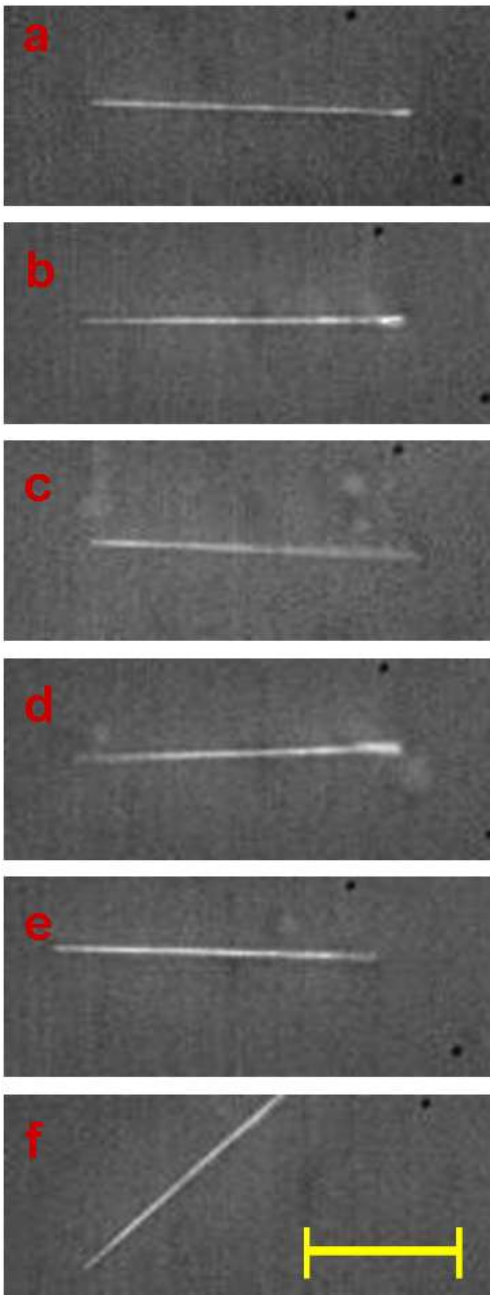

Figure 5.7 Still frame images (1/18000 s) displaying bubble emission from both ends of large length (100 µm) MBs functionalized with PFH emulsion. The (a) first frame displays a quiescent MB before a 44 µsec, 1.6 MPa US pulsing. Bubble formation begins in the (b) second frame after an US pulse and continues to progress in (c-e) subsequent frames. The dual bubble emission from both ends of the MB induces (f) spinning motion.

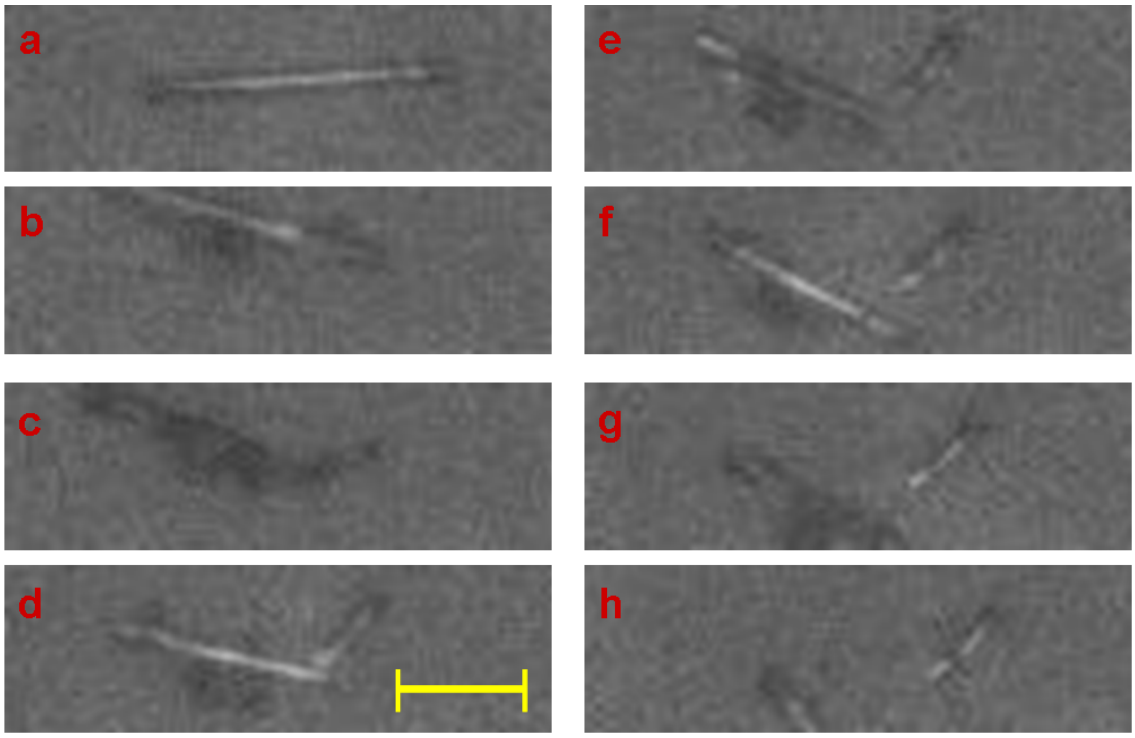

Figure 5.8 Still frame images (1/18000 s) displaying the breaking of MBs modified with PFH emulsion. The (a) first frame displays a quiescent MB before a 44 μsec, 1.6 MPa US pulsing. Bubble formation begins within the center of the MBs after (b) an US pulse and the MB begins to (c) rupture. The rupture continues to (c-f) propagate until the MB completely breaks into (g-h) two separate pieces. Scale bar, 30 μm.

Distinctly sized MBs (40 nm thick, 40 μm long, and 2.5 μm in diameter) produced ultrafast linear motion when functionalized with PFH droplets with a diameter of 180 nm. However, MBs that were longer (lengths >100 μm), longer and slender (60 μm long, 400 nm thick, 3 μm in diameter), and smaller MBs (8 μm long, 800 nm inner diameter) rotated uncontrollably (Figure 7), exploded (Figure 8), and stochastically agitated upon US pulse firing. Additional functionalization tests revealed that lower-boiling-point emulsions (PFP, bp 29°C)[198] vaporized more consistently at low pressures but were less stable during functionalization and increased MB explosion during US triggering. Further optimization of the emulsion size and composition could thus be used to tailor US-triggered propulsion devices for specific biomedical applications that require distinct microbullet velocity and momentum characteristics.

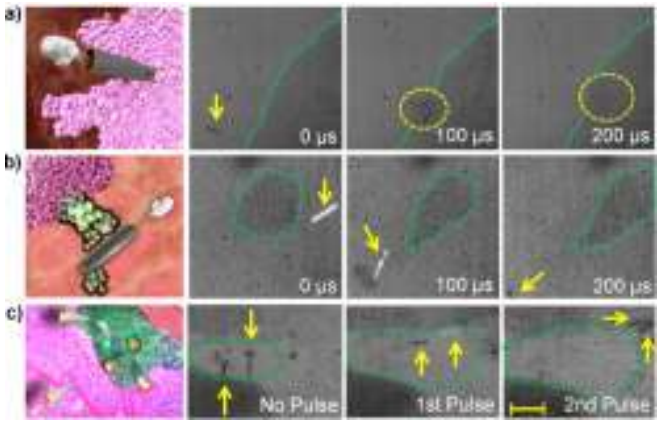

Figure 5.9 Computer-aided graphic (graphics on the left) and corresponding experimental images of PFH-loaded MBs a) penetrating, b) cleaving, and c) expanding a tissue following an US pulse signal. All images were taken sequentially at a frame rate of 10,000 fps and 10X objective. US pulses of 44 µs/1.6 MPa were used for (a, b) and short pulses of 4.4 µs/3.8 MPa were used for (c). Dotted circles and solid arrows are used to indicate the MB's position, while curvilinear dotted lines outline the tissue. Scale bar=100 µm in (a), 40 µm in (b), and 80 µm in (c).

To demonstrate the ability to penetrate through dense materials for potential targeted delivery applications, PFH-loaded MBs were fired into tissue sections from a lamb kidney. The image sequence in Figure 9a depicts the deep penetration of the MB into the lamb kidney tissue section after an US pulse. These sequential images illustrate the MB before locomotion, during initial tissue penetration, and after traveling 200 µm into the tissue from a single US pulse (44 µs, 1.6 MPa). A very short US pulse (4.4 µs) at high pressure (3.8 MPa) also provided sufficient thrust for the MBs to pierce kidney tissue (Figure 5). Figure 9b depicts the ability of the US-triggered MB to penetrate, deform, and cleave kidney tissue. Progressive images illustrate the MB capturing, deforming, and transporting a small piece of kidney tissue after an US pulse (44 µs, 1.6 MPa; Figure 9b). Thus, the US pulse pressure can be tuned to permit MB tissue piercing, deformation, or deep penetration, depending on the specifications and tissue degradation restrictions of distinct biomedical applications. Furthermore, the ability to propel multiple MBs from the same US pulse into a tissue section is displayed in Figure 9c. The potential power of multiple US-triggered MBs can be visualized as the MBs increase the tissue cavity area by 120%

after the first US pulse (4.4 μs, 3.8 MPa) and penetrate the kidney tissue after a second, similarly tuned US pulse (Figure 6).

5.3 Methods

5.3.1 Large microbullet (MB) (length >= 40 μm) fabrication

The Ti/Ni/Au MBs that were 40 μm or greater in length were prepared by modifying a previous top-down photolithographic protocol, which involves angled e-beam evaporation to provide stress-assisted rolling of functional nanomembranes on polymers into conical microtubes[228]. First, a positive microposit S1827 photoresist (Microchem, Newton, MA) was spin-coated onto a silicon wafer at 3000 rpm for 60 seconds. The coated-wafer was baked for 60 seconds at 115 °C before UV light (35 seconds) exposure using a MA6 mask aligner and various-sized MB patterns. Exposed patterns were etched using a MF-321 developer for 90 seconds before washing thoroughly with DI water. Metallic layers of Ti (10 nm), Ni (15 nm), and Au (15 nm) were evaporated sequentially onto the wafer for MBs 40 and 60 μm in length via an e-beam evaporator (Temescal BJD 1800) under high vacuum conditions ($<10^{-8}$ Pa). For larger MBs (>100 μm), 20nm of Ni and Au were deposited to provide needed support. The e-beam substrate holder was tilted to 48° in all cases to asymmetrically deposit the metals on the patterns. Resist remover, MF-1165 (Rohm & Haas, Marlborough, MA), was applied to the pre-stressed metallic layers, allowing for the immediate self-assembly of microtubes. The MBs underwent critical-point drying to prevent unwarranted tubular collapse.

5.3.2 Small Microbullet (length ~8 μm) Fabrication

Alternatively, small 8 μm MBs were prepared by electrodepositing sequential layers into a cyclopore polycarbonate membrane, containing numerous 2 μm conical-shaped pores (Catalog No 7060-2511; Whatman, Maidstone, U.K.). The electrodepostion of an outer polyaniline (PANI) layer and inner Au layer was carried out using a three-electrode set-up[256]. PANI microtubes were electropolymerized at +0.80 V for 0.02 C from a solution containing 0.1 M H_2SO_4, 0.5 M Na_2SO_4 and 0.1 M aniline; subsequently, the inner gold layer was plated at -0.9 V for 1 C from a commercial gold plating solution (Orotemp 24 RTU RACK; Technic Inc.). The membrane was dissolved in methylene chloride and repeatedly washed in methylene chloride, ethanol and ultrapure water. Electron beam evaporation of 10 nm Ti (adhesion layer) and 26 nm Ni (magnetic layer) onto the dried MBs was used to magnetically orient the small MBs.

5.3.3 Perfluorocarbon Emulsion Preparation

Perfluorohexane and perfluoropentane nanoemulsions were prepared in phosphate buffer saline (PBS). Briefly, 10 μL of 1 mM DiI-C18 (Biotium, Hayward, CA) dissolved in chloroform was evaporated in a 1.5 microcentrifuge tube. 850 μL PBS was added to the solution and a XL-2000 (Misonix, Farmingdale, NY) probe-type sonicator was operated at the bottom of the tube at level 20 until the DiI film was completely suspended in the buffer and the solution became hot to the touch. The tube was immediately placed in a heating block at 90ºC for 5 minutes and 50 μL of Zonyl FSE (Wilmington, DE) anionic fluorosurfactant was added. The solution was vortexed until homogenized and subsequently cooled in an ice bath. An 100 μl aliquot of perfluoropentane (Strem Chemicals, Newburyport, MA) or perfluorohexane (Alfa Aesar, Ward Hill, MA) was added and an XL-2000 (Misonix, Farmingdale, NY) probe was lowered in the tube about 8 mm from the bottom. While still in the ice bath, the sonicator was operated with a LabVIEW program interfaced with the sonicator via a foot pedal input and a reed relay board. The program delivered

three 0.5 second bursts and was repeated 60 times. The short bursts prevented the solution from stirring violently and producing foam; a 15 sec delay between each set of 3 bursts served to prevent overheating. This process resulted in a 10 vol% PFC emulsion which was stable and turbid in appearance. Emulsion sizes and zeta potentials were measured by dynamic light scattering with a Zetasizer Nano-ZS (Malvern Instruments, Worcestershire, UK). The 10 vol% PFC emulsion was diluted to 1% vol% by a PBS pH 7.4 solution before incubating with the MBs.

5.3.4 Conjugation of Perfluorocarbon Emulsion to Microbullet Interior

The inner Au layer allowed electrostatic binding and selective localization of the perfluorocarbon emulsions to the inner cavity of the bullet; thus bubbles were formed within and emitted from the MBs during US pulses. This Au interior layer provided an optimum surface for direct cysteamine binding (10mg/mL in water; Figure 1B), thereby forming a densely packed monolayer within 5 minutes[257]. The exposed amine group (pKa 8.6) of the cysteamine[254] is positively charged for the prescribed experimental settings (*i.e.*, pH range 7.4 - 8.0) and thus electrostatically binds to emulsions stabilized with an anionic phosphate fluorosurfactant (pKa 7.2). Emulsions were strongly negative with a measured zeta potential of -46 mV in phosphate buffered saline.

Before the electrostatic emulsion binding, copious amounts of DI water were used in numerous washing steps (~15) to remove all excess cysteamine. To ensure optimal emulsion binding for sufficient MB propulsion, the MBs were incubated overnight within the perfluorohexane emulsion (Figure 1C) under continuous flat shaker agitation (400 rpm). The MBs were repeatedly washed (10 times) with PBS/ultrapure H_2O (1:1000; final pH 8.0) before experimental testing. This composition of the washing solution prevents MBs from electrostatically binding to the glass surface while still promoting the emulsion/MB interaction.

Furthermore, saturation with liquid perfluorohexane (non-active) was used to prevent dissolution of the bound emulsion while stored for several days before experimental testing.

5.3.5 Ultrasound-Triggered Microbullet Propulsion

Subsequent MB propulsion was initiated (Figure 1D) by an US signal generated by a Panametrics V305-SU (Olympus NDT Inc., Waltham, MA), 2.25 MHz transducer connected via a Panametrics BCU − 58–6 W waterproof connector cable. The transducer was positioned within a water tank while the MBs were positioned at the water surface level between a glass slide and cover slip. Distinct US waveforms were generated from a PCI-5412 arbitrary waveform (National Instruments, Austin, TX) and amplified by a 300 W amplifier (Vox Technologies, Richardson, TX) to create acoustic intensities of up to 3 MPa peak negative pressure at the focus. A custom-designed LabVIEW 8.2 program was utilized to initiate the US pulses while a Photron FASTCAM 1024 PCI acquired the image sequences. A 40x magnification lens was used to acquire most initial experiments to visualize the gaseous bubbles; a 10x magnification lens was used to observe MBs locomotion and tissue penetrating characteristics. The glass slide acted as a coupling medium between the water tank and the MBs for the US pulses. In order to reduce the MB velocity for improved imaging, 20% v/v glycerol was added to the MB solution to increase viscosity for Figure 3b.

5.3.6 Microbullet Imaging

In order to capture the MB propulsion videos, individual image frames were acquired at 10,000 or 18,000 frames per second (fps) using a (10X, 20X or 40X Objective) FASTCAM 1024 PCI high speed camera (Photron, San Diego, CA).

5.3.7 Force and Speed Calculations

The velocity of the MB locomotion was calculated via Stoke's law. With the observations of the MB motion, and the Stokes' drag law for cylinders[258], it is possible to calculate multiple key physical parameters:

$$F_d = \frac{2\pi\mu L}{ln\left(\frac{2L}{R}\right) - 0.72} v$$, or $F_d = kv$, where $$k = \frac{2\pi\mu L}{ln\left(\frac{2L}{R}\right) - 0.72}$$,

and μ is the viscosity of the medium, L is the length, R is the radius, and v is the velocity. Using values from the below table, the average speed was calculated to be 6.3 m/s as determined from the distance traveled of 350 μm in 1/18,000 seconds (time elapsed in one frame). Using this calculated velocity in the Stokes' drag law for cylinders, the average drag force is determined to be 50.6 μN. To calculate the initial impulse of the US triggered propulsion, the initial MB speed and metal mass (negating the inner air/liquid containing volume) were evaluated to determine the instantaneous change in momentum.

The equation for the change in velocity over time (acceleration) was utilized to calculate the initial MB velocity

$$\frac{dv}{dt} = -\frac{F_d}{m} = -\frac{kv}{m}$$

, where m is the mass of the MB. By solving this differential equation, one can obtain the velocity function,

$$v(t) = v_0 e^{-\frac{kt}{m}}$$

, where v_0 is the initial velocity—subsequently determined by integrating the velocity over the length of one image frame

$$\int_0^{\Delta t} v(t)dt = \Delta d$$

Since the frame length, Δt is known from the camera settings, and the distance travelled, Δd is also known from image calibration, one can express the initial velocity in terms of known quantities,

$$v_0 = \frac{\Delta d}{\frac{m}{k} - \frac{m}{k} e^{-\frac{k\Delta t}{m}}}$$

Using these derived equations along with the quantity values displayed in Table 5.1, the initial velocity is calculated to be 56.9 m/s. Thus an initial momentum (p = mv) of 2.69E-11 Ns and kinetic energy (KE = ½mv^2) of 0.764 nJ was calculated for a MB with mass of 4.74E-13 kg. A special note should be considered when reviewing these calculations. Although it was possible to capture image sequences at frame rates greater than 18,000 fps, the MB velocity was so great that it was not possible to capture more than 2 or 3 frames during motion within the limited field of view. Since this was a memory speed limitation and not a limitation due to amount of light, we were, however, able to use shutter speeds of at least 1/303,000 seconds which could freeze the objects in motion. Thus, the velocity calculations presented herein are an approximation due to the limitations in MB image capturing.

Table 5.1 Table containing all of the necessary values to calculate the initial speed and impulse of the microbullet

Velocity Components	**Values**
Average Density	11.7 g/cm^3
Pre-rolled Volume (L x W x T)	(40 x 25 x .04 µm) = 4.00 · 10^{-11} cm^3
Mass	4.74 · 10^{-13} kg
Solution Viscosity	1.05 cP
Radius Rolled MB	2.5 µm
Time Between Frames	1/18000 s
Distance Traveled	350 µm
Drag Coefficient	8.89 · 10^{-8}

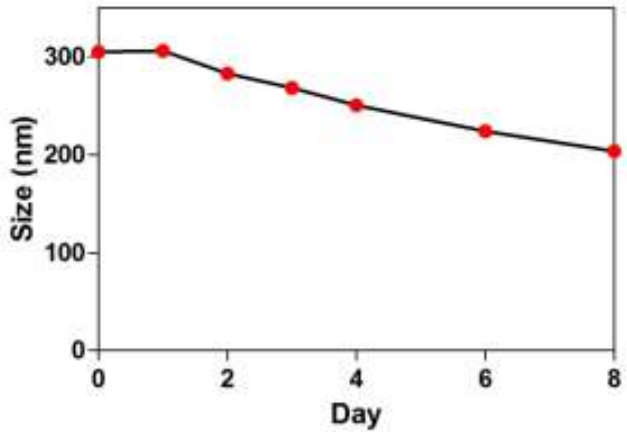

Figure 5.10 Size Stability of Perfluorohexane Emulsion over a Period of 8 Days. The initial diameter is 304.9 nm and there is a slight decrease of 4.7%/day.

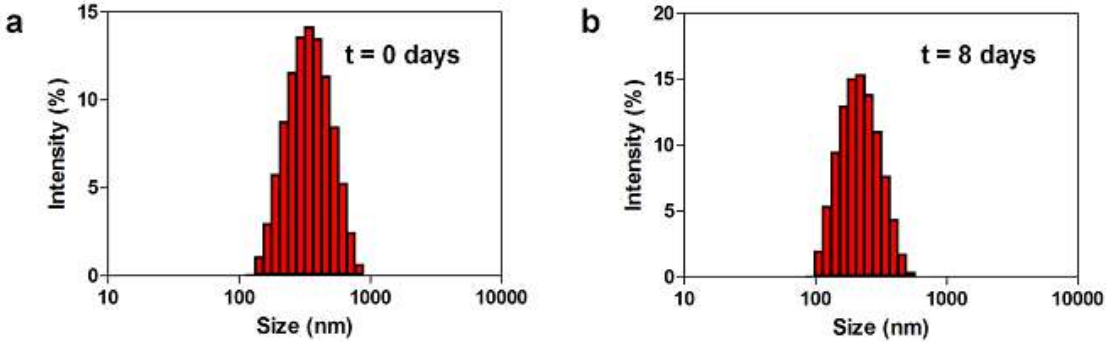

Figure 5.11 Size distribution of perfluorohexane emulsions (a) just after fabrication and (b) 8 days after fabrication. Dynamic light scattering measurements showed an initial mean diameter of 304.9 nm with a PDI of .144 and a diameter of 233.0 nm with a PDI of 0.161.

5.4 Conclusions

The presented ultrasound-triggered microbullet firing technique potentially offers a safe, low-cost, and effective method to project delivery devices into dense tissue or organs. These US-triggered, PFC-loaded MBs possess the unique ability to accelerate rapidly, acquire significant momentum (2.69×10^{-11} N s), and travel at average speeds over 6 m s^{-1} (i.e., approximately 100 times faster than previous micromachines). This unprecedented MB speed and force enables lamb kidney tissue piercing, deep penetration, deformation, and cleaving – capabilities that, to our knowledge, have not been demonstrated to date with micro/nanomachines. The US-triggered MB

propulsion technique is highly reproducible; approximately 80% of perfluorohexane-conjugated microbullets fire upon US pulsing, and MBs display negligible damage after multiple firing under optimized US conditions. The larger 40 μm microrockets were generally used in this study for visualization purposes, but the use of smaller 8 μm microbullets suggest that this is a scalable approach, opening the door for potential use in capillaries that are 5-10 μm in diameter. This US-triggered MB propulsion strategy should thus have a tremendous impact on diverse biomedical applications (e.g., targeted drug delivery, circulating biolistics, micro-tissue and artery-cleaning/removal schemes, precision nanosurgery, and cancer therapeutics). For example, as an alternative to treatment of bladder cancer with Bacillus Calmette-Guerin (BCG), multiple US-triggered MBs could be introduced and fired into the bladder, as illustrated in Figure 9c, to create a natural inflammatory response for fighting cancer cells. While offering a similar immunoprophylactic effect, the use of these MBs may potentially eliminate harmful side effects (e.g. sepsis, dysuria, hematuria, nausea, and fever) associated with BCG.

5.5 Acknowledgements

This chapter, in part, contains material from Kagan, Daniel; Benchimol, Michael; Claussen, Jonathan; Chuluun-Erdene, Erdembileg; Esener, Sadik; Wang, Joseph. "Acoustic Droplet Vaporization and Propulsion of Perfluorocarbon-Loaded Microbullets for Targeted Tissue Penetration and Deformation", Angewandte Chemie, vol. 51, 2012.

5.6 References

178. Kripfgans, O.D., Fowlkes, J.B., Miller, D.L., Eldevik, O.P. & Carson, P.L. Acoustic droplet vaporization for therapeutic and diagnostic applications. *Ultrasound in medicine & biology* **26**, 1177-1189 (2000).

179. Lo, A.H., Kripfgans, O.D., Carson, P.L., Rothman, E.D. & Fowlkes, J.B. Acoustic droplet vaporization threshold: effects of pulse duration and contrast agent. *IEEE transactions on ultrasonics, ferroelectrics, and frequency control* **54**, 933-946 (2007).

198. Le, T.D. & Weers, J.G. QSPR and GCA models for predicting the normal boiling points of fluorocarbons. *J. Phys. Chem.* **99**, 6739-6747 (1995).

219. Mallouk, T.E. & Sen, A. Powering nanorobots. *Scientific American* **300**, 72-77 (2009).

220. Ozin, G.A.M., I.; Fournier-Bidoz, S.; Arsenault, A. Dream Nanomachines. *Adv. Mater.* **17**, 3011-3018 (2005).

221. Pumera, M. Electrochemically powered self-propelled electrophoretic nanosubmarines. *Nanoscale* **2**, 1643-1649 (2010).

222. Howse, J.R. et al. Self-motile colloidal particles: from directed propulsion to random walk. *Physical review letters* **99**, 048102 (2007).

223. Kline, T.R., Paxton, W.F., Mallouk, T.E. & Sen, A. Catalytic nanomotors: remote-controlled autonomous movement of striped metallic nanorods. *Angewandte Chemie* **44**, 744-746 (2005).

224. Wang, J. Can man-made nanomachines compete with nature biomotors? *ACS nano* **3**, 4-9 (2009).

225. Mei, Y., Solovev, A.A., Sanchez, S. & Schmidt, O.G. Rolled-up nanotech on polymers: from basic perception to self-propelled catalytic microengines. *Chemical Society reviews* **40**, 2109-2119 (2011).

226. Mirkovic, T., Zacharia, N.S., Scholes, G.D. & Ozin, G.A. Nanolocomotion - catalytic nanomotors and nanorotors. *Small* **6**, 159-167 (2010).

227. Solovev, A.A., Mei, Y., Bermudez Urena, E., Huang, G. & Schmidt, O.G. Catalytic microtubular jet engines self-propelled by accumulated gas bubbles. *Small* **5**, 1688-1692 (2009).

228. Balasubramanian, S. et al. Micromachine-enabled capture and isolation of cancer cells in complex media. *Angewandte Chemie* **50**, 4161-4164 (2011).

229. Huang, G.W., J.; Mei, Y. Material considerations and locomotive capability in catalytic tubular microengines. *J. Mater. Chem.* **22**, 6519 (2012).

230. Kagan, D. et al. Rapid delivery of drug carriers propelled and navigated by catalytic nanoshuttles. *Small* **6**, 2741-2747 (2010).

231. Sanchez, S., Solovev, A.A., Harazim, S.M. & Schmidt, O.G. Microbots swimming in the flowing streams of microfluidic channels. *Journal of the American Chemical Society* **133**, 701-703 (2011).

232. Gao, W., Sattayasamitsathit, S., Orozco, J. & Wang, J. Highly efficient catalytic microengines: template electrosynthesis of polyaniline/platinum microtubes. *Journal of the American Chemical Society* **133**, 11862-11864 (2011).

233. Calvo-Marzal, P. et al. Propulsion of nanowire diodes. *Chemical communications* **46**, 1623-1624 (2010).

234. Gao, W., Sattayasamitsathit, S., Manesh, K.M., Weihs, D. & Wang, J. Magnetically powered flexible metal nanowire motors. *Journal of the American Chemical Society* **132**, 14403-14405 (2010).

235. Ghosh, A. & Fischer, P. Controlled propulsion of artificial magnetic nanostructured propellers. *Nano letters* **9**, 2243-2245 (2009).

236. Zhang, L. et al. Characterizing the swimming properties of artificial bacterial flagella. *Nano letters* **9**, 3663-3667 (2009).

237. Gao, W. et al. Cargo-towing fuel-free magnetic nanoswimmers for targeted drug delivery. *Small* **8**, 460-467 (2012).

238. Bertilla, S.M., Thomas, J.L., Marie, P. & Krafft, M.P. Cosurfactant effect of a semifluorinated alkane at a fluorocarbon/water interface: impact on the stabilization of fluorocarbon-in-water emulsions. *Langmuir : the ACS journal of surfaces and colloids* **20**, 3920-3924 (2004).

239. Worah, D.M.K., D. R.; Meuter, A. R.; Huang, M. G.; Correas, J.-M.; Quay, S. C. Perflenapent emulsion (EchoGen). *Drugs Fut.* **22**, 378-385 (1997).

240. Lentacker, I.D.S., S. C.; Sanders, N. N. Drug loaded microbubble design for ultrasound triggered delivery. *Soft Matter* **5**, 2161-2170 (2009).

241. Unger, E.C. et al. Therapeutic applications of lipid-coated microbubbles. *Advanced drug delivery reviews* **56**, 1291-1314 (2004).

242. Schutt, E.G., Klein, D.H., Mattrey, R.M. & Riess, J.G. Injectable microbubbles as contrast agents for diagnostic ultrasound imaging: the key role of perfluorochemicals. *Angewandte Chemie* **42**, 3218-3235 (2003).

243. Diaz-Lopez, R., Tsapis, N. & Fattal, E. Liquid perfluorocarbons as contrast agents for ultrasonography and (19)F-MRI. *Pharmaceutical research* **27**, 1-16 (2010).

244. Mattrey, R.F. Perfluorooctylbromide: a new contrast agent for CT, sonography, and MR imaging. *AJR. American journal of roentgenology* **152**, 247-252 (1989).

245. Reznik, N., Williams, R. & Burns, P.N. Investigation of vaporized submicron perfluorocarbon droplets as an ultrasound contrast agent. *Ultrasound in medicine & biology* **37**, 1271-1279 (2011).

246. Sheeran, P.S., Luois, S.H., Mullin, L.B., Matsunaga, T.O. & Dayton, P.A. Design of ultrasonically-activatable nanoparticles using low boiling point perfluorocarbons. *Biomaterials* **33**, 3262-3269 (2012).

247. Riess, J.G. Oxygen carriers ("blood substitutes")--raison d'etre, chemistry, and some physiology. *Chemical reviews* **101**, 2797-2920 (2001).

248. Biro, G.P., Blais, P. & Rosen, A.L. Perfluorocarbon blood substitutes. *Critical reviews in oncology/hematology* **6**, 311-374 (1987).

249. Park, H.C., Byun, K.T. & Kwak, H.Y. Explosive boiling of liquid droplets at their superheat limits. *Chem. Eng. Sci.* **60**, 1809-1821 (2005).

250. Wong, Z.Z., Kripfgans, O.D., Qamar, A., Fowlkes, J.B. & Bull, J.L. Bubble Evolution in Acoustic Droplet Vaporization at Physiological Temperature via Ultra-High Speed Imaging. *Soft Matter* **7**, 4009 (2011).

251. Castro, C.I. & Briceno, J.C. Perfluorocarbon-based oxygen carriers: review of products and trials. *Artificial organs* **34**, 622-634 (2010).

252. Barnett, S.B. et al. International recommendations and guidelines for the safe use of diagnostic ultrasound in medicine. *Ultrasound in medicine & biology* **26**, 355-366 (2000).

253. Raisinghani, A. & DeMaria, A.N. Physical principles of microbubble ultrasound contrast agents. *The American journal of cardiology* **90**, 3J-7J (2002).

254. Mezyk, S.P. Rate constant determination for the reaction of sulfhydryl species with the hydrated electron in aqueous solution. *J. Phys. Chem.* **99**, 13970-13975 (1995).

255. Borkent, B.M. et al. The acceleration of solid particles subjected to cavitation nucleation. *J. Fluid. Mech.* **610** (2008).

256. Campuzano, S. et al. Bacterial isolation by lectin-modified microengines. *Nano letters* **12**, 396-401 (2012).

257. Wirde, M., Gelius, U. & Nyholm, L. Self Assembled Monolayers of Cystamine, Cysteamine and 4-aminothiophenol studied by XPS and Voltammetry. *Langmuir : the ACS journal of surfaces and colloids* **15**, 6370 (1999).

258. Paxton, W.F., Sen, A. & Mallouk, T.E. Motility of catalytic nanoparticles through self-generated forces. *Chemistry* **11**, 6462-6470 (2005).

Chapter 6:

Ultrasound-Induced Fluorescence Modulation of Microbubble Contrast Agents

Abstract

A novel ultrasound-modulated fluorescent microbubble has been experimentally demonstrated. Because fluorescence modulation can be extracted from a strong non-modulated light background, this new contrast agent particle has the potential to significantly increase detection sensitivity by overcoming present limitations of optical detection at increased depths in highly scattering media. Using an optical pump (excitation beam) and focused ultrasound, microbubble size oscillations are converted into fluctuations in the spectrally distinct fluorescence emission. The intensity, spectral, and temporal characteristics of the modulated fluorescent signal can contain information about the contrast agent's biochemical environment such as tissue oxygenation, pH, and other properties which can be disease indicators. Microbubbles were prepared with surface-loaded self-quenching fluorophores and detected in an in-house designed setup to monitor fluorescence emitted from an insonified sample. Fluorescence intensity modulation was demonstrated with frequency components at the ultrasound driving frequency.

6.1 Introduction

Despite over 50 years of research validating the link between hypoxia and cancer malignancy, we have yet to develop a practical method for hypoxia detection[259, 260]. Although fluorescent probes have been developed to efficiently sense the hypoxic state, optical tissue scattering has been a barrier to their clinical translation[261-265]. A hybrid modality of ultrasound (US) and fluorescence imaging can break this barrier by exploiting their individual strengths of spatial resolution and sensitivity, with the added benefits of being non-ionizing, low cost, and real-time. While acousto-optic imaging has these benefits and an optical readout, it lacks the selectivity to modulate fluorophores independently of the autofluorescent tissue background[266].

Creating an US-modulated beacon of light will enable optical detection at the spatial resolution of US, at centimeter-scale depths. The sensitivity of fluorescence will allow the

discrimination of a small labeled region from a large background. Since random "noise" and autofluorescence photons will not fluctuate with any characteristic frequency, they can be removed by filtering or spectral analysis. The enabling technology developed in this work is a microbubble (MB), surface-loaded with a fluorophore at sufficiently high concentration to exhibit self-quenching. The MB oscillates radially in response to US insonation, causing the surface fluorophore concentration to change (Fig. 1). In the high pressure portion of the wave, the bubble compresses, increasing the surface density of fluorophore, and the degree of fluorescence quenching. In the low pressure portion of the wave, the bubble expands, decreasing the surface density of the fluorophore, and thus decreasing the amount of quenching. Thus, the degree of quenching will be modulated at the frequency of the applied US.

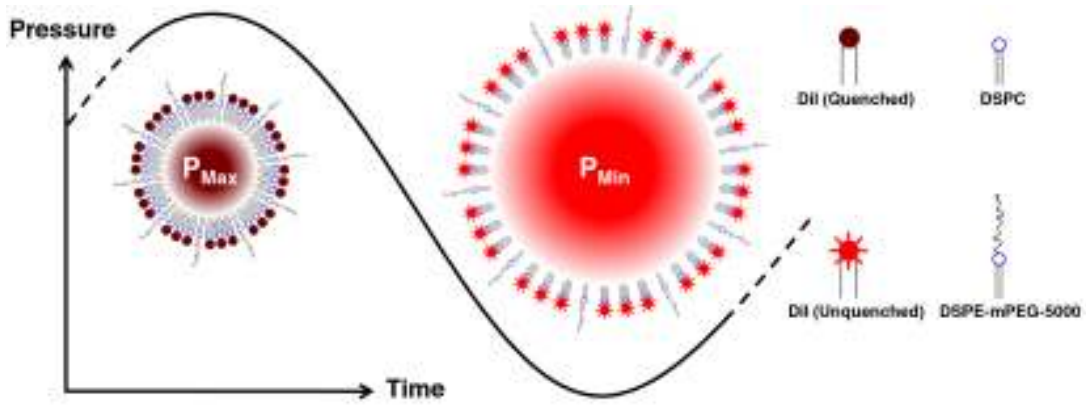

Figure 6.1 Schematic of Principle. A microbubble (MB) experiences radial oscillations in response to acoustic waves. The surface concentration of the dye is inversely proportional to the square of the bubble radius. Due to the non-linear distance dependence of dye quenching efficiency, a small increase in intermolecular distance can produce a large increase in the fluorescence quantum yield.

B. Yuan has provided a theoretical description of a similar system using a fluorophore-quencher pair[267], predicting a possible 100% modulation efficiency. The MB structure presented in this work is achieved by modifying a stable MB formulation with the addition of a single dye component in the MB shell. While the concept of this particle has been previously discussed

theoretically in the literature, we present the first experimental evidence of dye-loaded MBs whose fluorescence emission can be modulated in response to US.

6.2 Results

MBs containing DiI and biodegradable phospholipids were fabricated using variations on published formulations[268, 269] very similar to those used in Definity®, an FDA approved US contrast agent. A gas mixture containing perfluorocarbon was used as the MB core due to the perfluorocarbon's inertness and low solubility in blood, which helps prolong MB *in vivo* biological half-life[242]. MBs were easily purified from excess lipid and dye by centrifugation due to their buoyancy. Multiple washings yielded a very pure sample while preserving the MBs (Fig. 2a,b). The fabricated MBs ranged between 1-5 μm in diameter, optimal to achieve resonance with medical US frequencies of 1-10 MHz[270]. The MBs were strongly echogenic, as verified by a clinical ultrasound scanner, which was able to observe a strong contrast enhancement at a 1:1000 dilution (Fig. 2d).

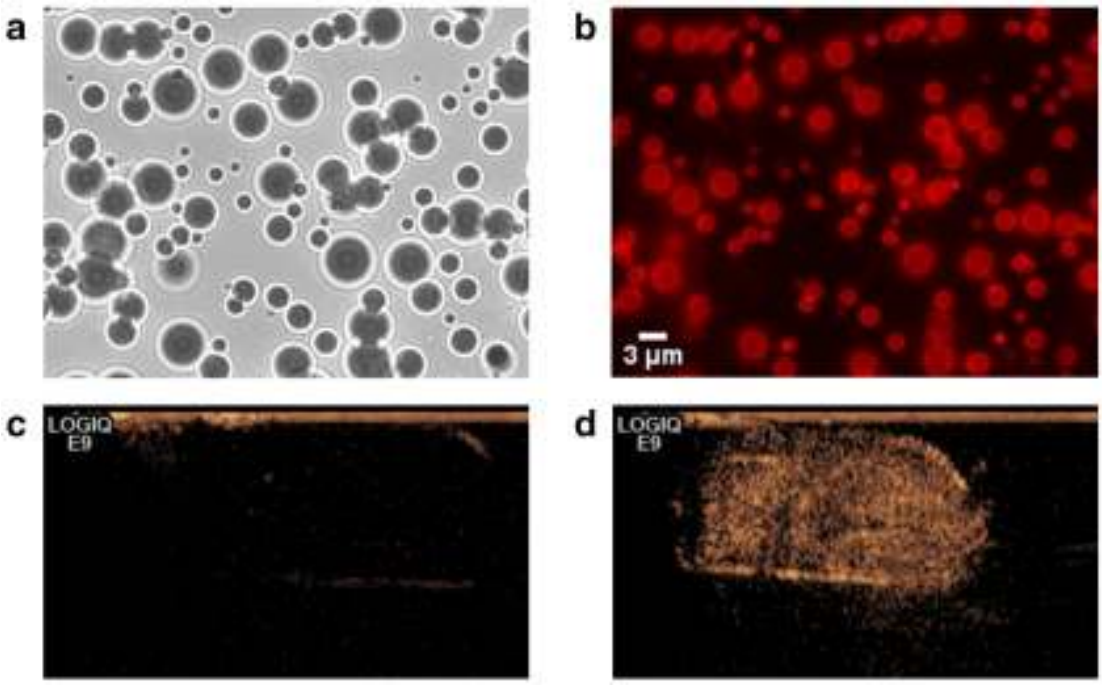

Figure 6.2 Microbubbles surface-loaded with a high concentration of DiI (2 mol %), imaged in (a) brightfield, (b) fluorescence, and (d) ultrasound contrast-mode. a, Brightfield microscope images show microbubbles with a 1-5 µm distribution. **b,** Although fluorescence quenching is occurring to an extent, residual fluorescence can still be seen. Even unloaded MBs (not shown here) will appear as a bright ring in a fluorescent medium, due to reflection off the gas/liquid boundary, but fluorescence from the center of the bubble is evidence of efficient surface loading. **c,** A pure buffer control shows a faint outline of the transfer pipette container with no contrast enhancement. **d**, A 1:1000 dilution of microbubbles in buffer generated a strong contrast enhancement.

MBs were fabricated with varying concentrations of DiI and relative fluorescence intensity of individual MBs was quantified by fluorescence microscopy (Fig. 3). The average fluorescence emitted from a molecule of DiI decreased with increased surface concentrations, following a trend characteristic of self-quenching (Fig. 3b). These results predict a concentration of 2 mol % to be in the optimal range, since it is there that the slope of fluorescence intensity vs. dye concentration is highest. For the relationship between quenching efficiency and intermolecular distance, there was good agreement between experimental results and a theoretical curve developed from a FRET efficiency model. This model was chosen due to the dynamic nature of DiI self-quenching.

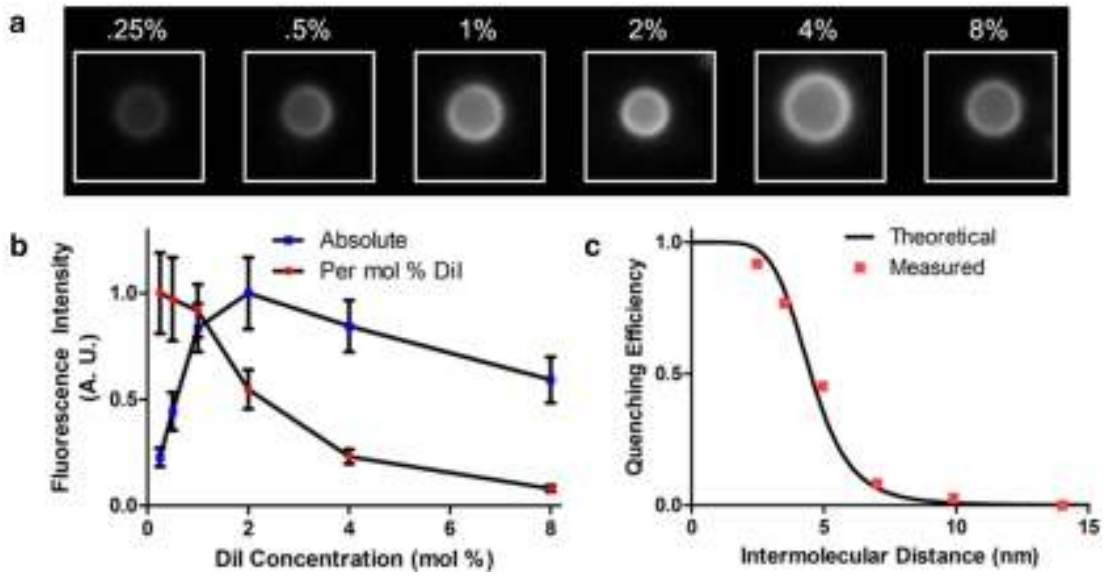

Figure 6.3 Self-quenching of DiI loaded on the surface of MBs. a, Representative MBs loaded with increasing dye concentrations were imaged, and the fluorescence intensity per unit area was calculated. **b**, The normalized fluorescence intensity is plotted against DiI concentration, both in absolute intensity, and adjusted for DiI concentration. **c**, Quenching efficiency was plotted, assuming the complete absence of quenching for the lowest concentration, and shown with a theoretical quenching curve. DiI intermolecular distance was calculated based on molar concentration. See section 2.3 for a more detailed description of the theoretical calculation and measured values.

An in-house designed high-throughput MB characterization setup[271] was modified to detect US-modulated fluorescence as described in section 4.4. Experiments were conducted in deionized water and no additional scattering media was added. A representative voltage output of the PMT detecting MB fluorescence emission is shown in Figure 4a as a function of time. There is a very clear time domain oscillation with the corresponding Fourier transform (Fig. 4b) revealing a strong component at the US driving frequency of 2.25 MHz. Second harmonic frequency signatures at 4.5 MHz were also detected on occasion, indicating non-linear effects stemming from known asymmetric oscillations of lipid MBs[272, 273]. Peak-to-peak voltage was approximately 65mV, yielding an SNR of 3.68 for the single 15-cycle pulse. Moving to a time-averaged or frequency lock-in system may provide a means to further increase the SNR.

MBs are also capable of amplifying the acousto-optic modulation of fluorescence as previously shown in the literature[274]. To control for this effect, fluorescent liposomes were added to a sample of MBs prepared without the fluorophore coating, to achieve the same bulk fluorescence intensity as in the surface-loaded MBs. Under the same conditions, no fluorescence oscillations were seen in the control samples. This supports that the observed fluorescence modulation is due to the hypothesized self-quenching effect as opposed to modulation of the excitation beam or a change in the optical properties of the MB.

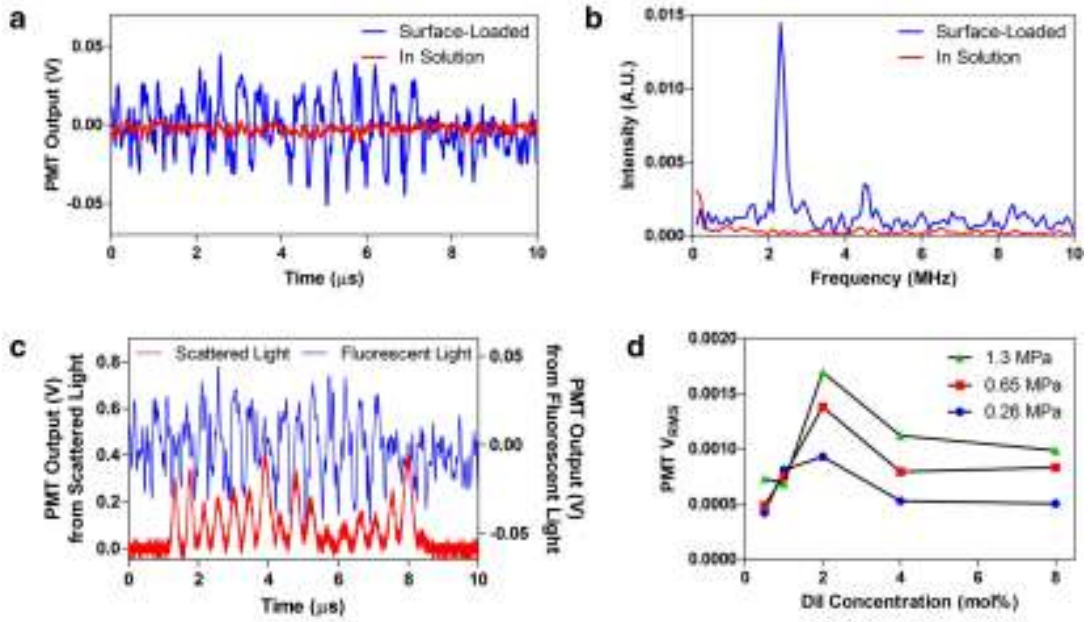

Figure 6.4 Demonstration of fluorescence modulation with US. Microbubbles were excited with 15 cycles at 2.25 MHz while a CW laser excited their fluorescence. **a**, Voltage output from the PMT which is detecting the fluorescence. **b**, FFT of the time-domain signal showing a strong peak at the fundamental and a smaller peak at the second harmonic. Non-fluorescent microbubbles were diluted into a fluorescent medium as a control, which showed no fluorescence modulation. **c**, Simultaneous acquisition of fluorescent and scattered light from a sample of MBs. Two PMTs were used to independently detect the signals, which were observed to be in phase. This demonstrates that the fluorescent signal is directly correlated with the contraction and expansion of the MBs. The US pressure used was 1.3 MPa. **d**, Mean modulation intensity at different dye concentrations and US intensities. MBs were fabricated with varying surface concentrations of fluorophore. For a population of detection events, the mean modulation intensity was taken as a measure of the signal strength. With too little fluorophore, there is not much quenching. With too much fluorophore, there is too much quenching. An optimal concentration was determined to be around 2 mol% of the stabilizing lipid shell.

The experimental setup described in section 4.4 is also capable of monitoring US-induced size oscillations of MBs through the detection of scattered light[275]. Since the light is collected orthogonal to the incident laser, unfiltered light is representative of the side scatter intensity, which has a strong dependence on particle size. By observing the radial oscillations of individual MBs, this method verified that oscillating MBs were present in the control samples.

A second detector was used to observe the oscillations of the scattered light at the same time as the fluorescence oscillations by splitting the light with a beamsplitter, and filtering only one path (Fig. 5). Peaks in fluorescence corresponded temporally with peaks in the scatter signal (Fig. 4c). This was expected since in the rarefaction phase, when the bubble diameter is the greatest, the bubble will scatter more light and the fluorophore molecules should be most separated, giving the greatest fluorescence intensity. The scattered light modulation was seen consistently and prevalently in all samples containing MBs. However, the fluorescence modulation signal was only observed for a subset of these MBs, all of which were fluorescent (Fig. 2b), and was not always present for those bubbles which generated the largest scattered light modulations. These observations suggest that the fluorescence modulations are produced by the ability of a distinct population of MBs to undergo the above described fluorescence quenching of surface dyes. Future work will look into the underlying cause of the MB variability in this fluorescence quenching modulation.

In order to extract the fluorescence signal of the oscillating MB from a noise-limited environment, both a strong peak fluorescence intensity and maximum modulation intensity are desirable. As the MB dye concentration was varied, it was shown that the signal intensity was dependent on the surface concentration of the fluorophore (Figure 4d). An optimal concentration was found near 2 mol% where the transition of the MB from fully contracted to fully expanded corresponds with the greatest change in degree of quenching. Insufficient fluorophore concentration resulted in weakly quenched MBs, even when fully contracted. Similarly, MBs

containing very high concentrations of fluorophore were always overly quenched. The signal strength also increased with US intensity, even to a point where the pressure was sufficiently large to destroy some of the MBs with just a few pulses. Still, most MBs were able to stably oscillate for more than 10 cycles at peak-to-peak pressures above 1 MPa.

6.3 Discussion

The self-quenching of DiI is a well-documented dynamic quenching mechanism, evidenced by a change in fluorescence lifetime at increasing concentrations[276]. Many similar carbocyanine dyes exist at longer wavelengths, but the excitation and emission spectra of DiI were ideally matched with light sources and detectors available to us. It has been shown that in response to US the radius of a lipid-stabilized MB can change by a factor of 5 or more from its most compressed state to its most expanded state[277]. The strong distance dependence of quenching would predict that even a much smaller oscillation could result in a large change in fluorescence emission.

A new lipid-based MB incorporating the lipophilic dye DiI into the stabilizing shell has been developed to test the combination of these two physical mechanisms. The working principle of the MBs studied here relies on the relatively uniform and elastic expansion of the MB shell. If shell "cracking" occurs, where the lipid monolayer splits open in a region, a much less pronounced effect should be expected, since most of the fluorophores will remain closely packed. This is likely to happen for MBs stabilized with lipids forming domains, segregated regions of certain lipid molecules[278]. Phase segregation in stabilizing lipid monolayers is more present in formulations containing a significant amount of lipopolymer[279, 280]. For this reason, the amount of lipopolymer in our formulation was limited to the minimum required for stability. For neutrally charged MBs, a certain amount of polymer (typically polyethylene glycol) is often used for steric

repulsion, in order to prevent coalescence and gas dissolution and maintain a stable MB suspension[281].

The insonation frequency is also an important parameter in the design of a fluorescence-modulating MB, since the frequency has an impact on the velocity of molecular separation. Physically separated lipid molecules are not in a thermodynamically stable state. If given time, they will rearrange to pack closely and minimize surface contact. For this reason, a MB or emulsion suspension made with limited surfactant is unlikely to have sparsely-coated droplets. Instead, there will either be fewer number of large droplets, or more likely, the particles will coalesce to reduce the surface-to-volume ratio until there is a small enough surface area which can be completely coated. By using MHz frequencies, the lipid molecules are forced to separate and come back together in under a microsecond. This study indicates that this time is insufficiently long for them to rearrange, since the basic mechanism of modulation is dependent on molecular separation. The frequency was kept constant in this study for the sake of simplicity. Further work will be done to study the frequency dependence of fluorescence modulation. It is expected that fluorescence modulation intensity will decrease at lower frequencies.

The US-modulated fluorescent emission of the MB will enable the extraction of optical information at the higher spatial resolution possible with US. A promising potential application of this technique is to use the optical spectral information detected to determine biochemical properties of the tissue being probed. Types of tissue have specific optical absorptive and scattering properties which can modify the spectral signature. By analyzing detected spectra, the fluorescence-modulating MBs can help classify the tissue into various categories including benign versus cancerous. The MB contrast agents can be tuned to provide information about local tissue properties by the inclusion of fluorescent agents whose emission wavelength and intensity are sensitive to the environment[282]. The spectrum of the detected light can contain information about relative tissue oxygenation, pH, and other properties which can be disease indicators[283].

6.4 Materials and Methods

6.4.1 Microbubble Materials

Distearoyl phosphatidylcholine (DSPC) and distearoyl phosphatidylethanolamine-methyl poly(ethylene glycol) MW5000 (mPEG-DSPE) were purchased from Avanti Polar Lipids, Inc. (Alabaster, AL). DiI (DiIC18(3), or 1,1'-dioctadecyl-3,3,3',3'-tetramethylindocarbocyanine perchlorate) was purchased from Biotium Inc. (Hayward, CA). DPBS was purchased from GIBCO (Bethesda, MD). Perfluorohexane was purchased from Sigma-Aldrich (St. Louis, MO).

6.4.2 Microbubble Preparation

Stock solutions of the lipids and the dye were prepared by dissolving the dry powder in chloroform. 1 mg of DSPC and 1 mg of mPEG-DSPE were combined in a 1.5 mL microcentrifuge tube. An appropriate amount of DiI was added to the same tube. The solution was vortexed at low speed while applying an argon stream to evaporate all of the chloroform and create a lipid film.

500 μL of DPBS was added to the lipid film, and the tube was vortexed at high speed for 1 minute. The tube was immediately placed into a heating block which was at 70°C. After 1 hour, the tube was removed and placed directly on ice for 5 minutes. A 3 mL syringe was loaded with 100 μL perfluorohexane. A 1.5" 22 gauge needle was attached and bent at a 60° angle to allow the syringe to be pumped without ejecting liquid. By pumping the syringe, the perfluorohexane was vaporized, and the headspace of the tube was filled with a mixture of air and perfluorohexane vapor.

The XL-2000 probe sonicator (QSonica LLC., Newtown, CT) was operated at the liquid/gas interface for 3 seconds at 25 W to produce MBs. The bubbles were then put back on ice. To purify the bubbles and wash away the excess lipid and dye, the bubbles were centrifuged at 1000 rpm for 3 minutes. The subnatant was removed with a syringe (approximately 450 μL), and the bubbles were resuspended with 500 μL DPBS. This was repeated once more. For the

control samples, MBs containing no DiI were prepared in the same method. In addition, liposomes containing DiI were prepared with fluorescence equivalent to the DiI-labeled MBs.

6.4.3. Contrast-Enhanced Ultrasound Imaging of DiI-Loaded Microbubbles

Microbubbles surface-loaded with 2 mol% DiI were diluted 1:1000 into standard disposable transfer pipettes (ThermoFisher Scientific, Waltham, MA) containing DPBS to achieve a total volume of 3 mL. Samples were held in water tank at 22°C while a Logiq E9 (GE Healthcare, Wauwatosa, WI) ultrasound scanner coupled to a ML6-15 probe was used to acquire images of the microbubbles in contrast mode.

6.4.4 Quantification of Static Fluorescence and Calculation of Intermolecular Distance

Microscope images were acquired through MetaMorph® Microscopy Automation & Image Analysis Software. Fluorescence was imaged using a Cy3/Cy5 filter. Unscaled images were acquired for each dye concentration and processed in ImageJ. For each dye concentration, the pixel intensity per unit area from 20 representative bubbles was integrated and the standard deviation was calculated. For the calculation of quenching efficiency, the lowest dye concentration (.25 mol%) was taken as a completely unquenched state, for simplicity. Quenching efficiency at a given dye concentration was calculated as the percent decrease of fluorescence per mole of dye from that at .25 mol%.

Intermolecular distance was calculated using an average lipid head diameter of 7 Å[284]. The linear density was taken as the square root of the surface density. The theoretical quenching efficiency was computed using the Förster resonance energy transfer (FRET) efficiency equation

$$E = \frac{1}{1 + (r/R_0)^6}$$

, where R_0 is the Förster radius of 45 Å, as cited for the DiO-DiI distance[285]. DiO is a lipophilic carbocyanine dye structurally similar to DiI and the DiO-DiI Forster radius was assumed similar to that of DiI-DiI, since there is a similar degree of spectral overlap.

6.4.5 Experimental Setup

An acousto-fluorescence detection setup was used to study the interaction of US with the quenchable MBs. The experimental setup is shown in Figure 5. A two liter black water bath was used for a clean sound field with transparent optical windows for light delivery and collection. A Verdi-V5 continuous-wave 532nm laser source (Coherent Inc., Santa Clara, CA, USA) was focused with a 20x objective with a power density greater than 5μW/cm^2 at the laser focus. A 2.25MHz focused single-element Panametrics V306 ultrasound transducer (Olympus NDT Inc., Waltham, MA, USA) was aligned with its focus confocal with the laser focus. The US was pulsed at a 1Hz repetition rate, with 15 cycles per pulse at 2.25MHz, which was within the resonance frequency range of the 1-5 μm MBs. Transducer positioning and US pressure were calibrated with a HNC-0200 needle hydrophone (Onda Corp., Sunnyvale, CA, USA).

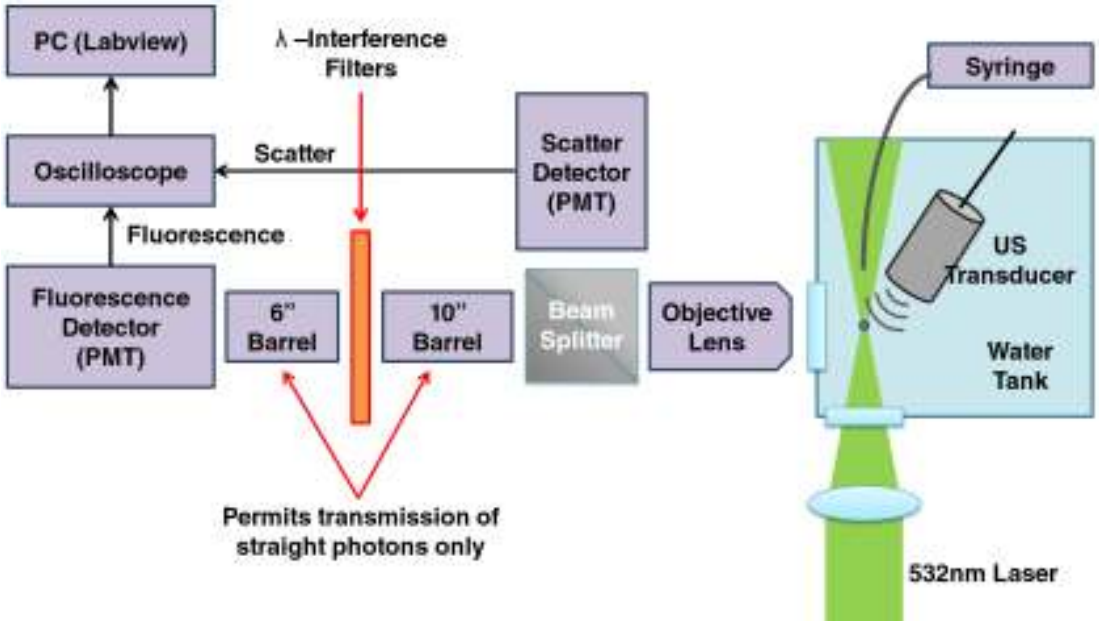

Figure 6.5 Experimental setup for fluorescence modulation detection. An US transducer, laser-focusing lens, and collection objective are all confocal and mutually orthogonal. The collected light is split into two paths, one of which is filtered to look at fluorescence. Two independent PMTs collect the different signals, and their output is connected to an oscilloscope. Data is acquired and preprocessed through LabVIEW.

Light was collected at 75^{o} to 95^{o} and split into two paths with a beam splitter with two photomultiplier tubes (PMTs) used simultaneously to monitor both the fluorescence signal and the optical scatter of excitation light to correlate MB size changes to fluorescence modulation intensities. Both optical signals were recorded simultaneously with LabVIEW. The scattered light was intense enough to be detected with a PMT operating at low gain. At this gain, MB fluorescence was too weak to be detected. To detect the fluorescent signal, light was passed through two optical filters onto a low dark current R6095 PMT optical detector (Hamamatsu Corp., Bridgewater, NJ, USA) with a 10MHz bandwidth, operated at high gain. Two filters (a 546 nm long pass and 570 nm band pass) were used for a high rejection ratio of the excitation light. Because the filters are interference filters, normal incidence of photons is necessary for high rejection ratios. Therefore, two long black optical barrels were used to ensure only straight photons could pass through the filters and reach the optical detector. The PMT signal was then

passed through a low noise M7279 amplifier (Hamamatsu Corp., Bridgewater, NJ, USA), held at constant gain, to a high-speed digital TDS2020 sampling oscilloscope (Tektronix Inc., Beaverton, OR, USA) which was controlled using LabVIEW software on a computer. MBs were delivered using a PHD 2000 syringe pump (Harvard Apparatus, Holliston, MA, USA) and a capillary tube placed in-line with the laser optical axis and outside the US interaction region. The presence of flowing MBs was confirmed by looking at the unfiltered scattered light with a standard video-rate 1322 CCD camera (Cohu Inc., San Diego, CA, USA).

To load a sample, a 60 mL syringe was filled with 40 mL of DI water, to which 100 μL of the MB suspension was added. For the control samples, after 100 μL of undyed MBs was added, 100 μL of fluorescent liposomes was then added to achieve a bulk fluorescence equal to that of the fluorescent MBs. The syringe was then rotated gently to completely disperse the MBs and liposomes in the entire volume. It was chosen to have the sample flow directly into the water tank, since water is an excellent medium both for optics and acoustics. This prevented the need for any tube which could potentially scatter light and/or sound. In between samples, the water tank was drained, washed, and refilled to prevent contamination.

6.5 Conclusions

Stable MBs were fabricated and surface-loaded with a lipophilic self-quenching dye. These MBs were demonstrated to modulate their fluorescence emission in response to applied US. While many known methods use acoustic waves to modulate the paths of existing photons, to our knowledge this is the first experimental demonstration of US modulation of the number of emitted fluorescent photons. Therefore, the acoustic stimulation is changing the ratio of excitation energy converted into radiative vs. non-radiative energy. A clinically relevant future approach will be to design modulating MBs utilizing near-infrared fluorophores to enhance signal-to-background ratios and increase light penetration depth through the body. The system described in

this work has the potential to be used in conjunction with the above-mentioned environmental biochemical sensors, and to allow spatially precise measurements of deep tissue properties.

6.6 Acknowledgements

This chapter, in part, has been submitted for publication as it may appear in Soft Matter, Benchimol, Michael; Hsu, Mark; Schutt, Carolyn; Hall, David; Mattrey, Robert; Esener, Sadik. "Phospholipid/Carbocyanine Dye-Shelled Microbubbles as Ultrasound-Modulated Fluorescent Contrast Agents".

I am grateful to Emilia Olson for help with ultrasound imaging of microbubbles.

6.7 References

259. Gray, L.H., Conger, A.D., Ebert, M., Hornsey, S. & Scott, O.C. The concentration of oxygen dissolved in tissues at the time of irradiation as a factor in radiotherapy. *The British journal of radiology* **26**, 638-648 (1953).

260. Seton-Rogers, S. Hypoxia: New connections. *Nature reviews. Cancer* **12**, 320-321 (2012).

261. McEvoy, A.K.M., C. M.; MacCraith, B. D. Dissolved oxygen sensor based on fluorescence quenching of oxygen-sensitive ruthenium complexes immobilized in sol–gel-derived porous silica coatings *The Analyst* **121**, 785-788 (1996).

262. Zhong, W.U., P.; Mycek, M. A. Imaging fluorescence lifetime modulation of a ruthenium-based dye in living cells: the potential for oxygen sensing *Journal of Physics D: Applied Physics* **36**, 1689-1695 (2003).

263. Kiyose, K. et al. Hypoxia-sensitive fluorescent probes for in vivo real-time fluorescence imaging of acute ischemia. *Journal of the American Chemical Society* **132**, 15846-15848 (2010).

264. Zhang, G., Palmer, G.M., Dewhirst, M.W. & Fraser, C.L. A dual-emissive-materials design concept enables tumour hypoxia imaging. *Nature materials* **8**, 747-751 (2009).

265. Okuda, K. et al. 2-Nitroimidazole-tricarbocyanine conjugate as a near-infrared fluorescent probe for in vivo imaging of tumor hypoxia. *Bioconjugate chemistry* **23**, 324-329 (2012).

266. Yuan, B., Gamelin, J. & Zhu, Q. Mechanisms of the ultrasonic modulation of fluorescence in turbid media. *J Appl Phys* **104**, 103102 (2008).

267. Yuan, B. Ultrasound-modulated fluorescence based on a fluorophore-quencher-labeled microbubble system. *J Biomed Opt* **14**, 024043 (2009).

268. Kabalnov, A. et al. Dissolution of multicomponent microbubbles in the bloodstream: 2. Experiment. *Ultrasound Med Biol* **24**, 751-760 (1998).

269. Sirsi, S. & Borden, M. Microbubble Compositions, Properties and Biomedical Applications. *Bubble Sci Eng Technol* **1**, 3-17 (2009).

270. Phelps, A.D.L., T. G. The Subharmonic Oscillations And Combination-Frequency Subharmonic Emissions From A Resonant Bubble: Their Properties and Generation Mechanisms *Acta Acustica united with Acustica* **83**, 59-66(58) (1997).

271. Hsu, M.J. et al. Characterization of individual ultrasound microbubble dynamics with a light-scattering system. *J Biomed Opt* **16**, 067002.

272. Crum, L.A. & Prosperetti, A. Nonlinear oscillations of gas bubbles in liquids: An interpretation of some experimental results. *Journal of the Acoustical Society of America* **73**, 121-127 (1983).

273. Shi, W.T. & Forsberg, F. Ultrasonic characterization of the nonlinear properties of contrast microbubbles. *Ultrasound Med Biol* **26**, 93-104 (2000).

274. Yuan, B., Liu, Y., Mehl, P.M. & Vignola, J. Microbubble-enhanced ultrasound-modulated fluorescence in a turbid medium. *Applied Physics Letters* **95** (2009).

275. Hall, D.J., Hsu, M.J., Esener, S.C. & Mattrey, R.F. Detection of ultrasound-modulated photons and enhancement with ultrasound microbubbles. *SPIE Proceedings* **7177** (2009).

276. Packard, B.S. & Wolf, D.E. Fluorescence lifetimes of carbocyanine lipid analogues in phospholipid bilayers. *Biochemistry* **24**, 5176-5181 (1985).

277. Morgan, K.E. et al. Experimental and theoretical evaluation of microbubble behavior: effect of transmitted phase and bubble size. *IEEE Trans Ultrason Ferroelectr Freq Control* **47**, 1494-1509 (2000).

278. Borden, M.A. et al. Influence of lipid shell physicochemical properties on ultrasound-induced microbubble destruction. *IEEE Trans Ultrason Ferroelectr Freq Control* **52**, 1992-2002 (2005).

279. Borden, M.A. et al. Lateral phase separation in lipid-coated microbubbles. *Langmuir* **22**, 4291-4297 (2006).

280. Borden, M.A., Pu, G., Runner, G.J. & Longo, M.L. Surface phase behavior and microstructure of lipid/PEG-emulsifier monolayer-coated microbubbles. *Colloids Surf B Biointerfaces* **35**, 209-223 (2004).

281. Klibanov, A.L. Ultrasound Contrast Agents: Development of the Field and Current Status. *Topics in Current Chemistry* **222**, 73-106 (2002).

282. Niu, C.G., Gui, X.Q., Zeng, G.M. & Yuan, X.Z. A ratiometric fluorescence sensor with broad dynamic range based on two pH-sensitive fluorophores. *Analyst* **130**, 1551-1556 (2005).

283. Helmlinger, G., Yuan, F., Dellian, M. & Jain, R.K. Interstitial pH and pO2 gradients in solid tumors in vivo: high-resolution measurements reveal a lack of correlation. *Nat Med* **3**, 177-182 (1997).

284. Heimburg, T. A model for the lipid pretransition: coupling of ripple formation with the chain-melting transition. *Biophys J* **78**, 1154-1165 (2000).

285. Yefimova, S.L. et al. Hydrophobicity effect on interactions between organic molecules in nanocages of surfactant micelle. *Journal of Applied Spectroscopy* **75**, 658-663 (2008).

Chapter 7:

Conclusions and Future Directions

7.1 Localized Chemotherapy Using Drug-Loaded Ultrasound-Ruptured Liposomes

The novel liposome structures developed in this work and described in this dissertation are delivery platforms for a broad range of anti-cancer agents and other therapeutics which benefit from specific delivery. The microbubble-encapsulating liposome (SHERPA) described in Chapter 2 was able to be disrupted by low levels of ultrasound in the diagnostic range. The microbubble also potentially can be used as a contrast agent for in vivo tracking of the particles in the bloodstream.

An ultrasound-ruptured liposome (URL) containing cavitation-nucleating nanoparticles was then developed to scale down the liposome size and improve stability. Although the required acoustic activation power was higher, it was still in the range of energies which can be safely used for therapy. These structures were able to show efficient release of small molecule payloads in vitro, and local delivery of fluorescent markers in vivo.

In order to demonstrate the therapeutic potential of the ultrasound-ruptured liposomes (URL) described in Chapter 3, the most logical and straightforward next step is to encapsulate a chemotherapy drug and apply a similar sonication protocol to those used in the fluorescent demonstrations. Doxorubicin will be the first drug used due to its extensive clinical history in liposomal formulations, and prior use in well established animal models. In mice with human xenograft tumors, tumor regression in sonicated vs. non-sonicated tumors will be the primary measure of treatment efficacy.

In order to establish superiority of the URL to current chemotherapy regimes, two different demonstrations can be explored. The first demonstration can show improved tumor regression vs. standard free or liposomal doxorubicin, using the same dose. The second demonstration can be to achieve equal efficacy to a clinical formulation with a lower dose. Since the current paradigm is to achieve maximum tumor eradication at the expense of significant side effects, the first demonstration is probably closer to what would be implemented in a clinical

setting. However, the second demonstration enables effective chemotherapy with fewer side effects, potentially allowing for more cycles of treatment before reaching a cumulative cardiotoxicity dose limit. Also, if the target region is adequately treated, the use of a lower dose could be equally effective by sparing the immune cells which are associated with remission[286].

7.2 Protein Payloads for Cancer Therapy

The enzyme-loaded URL described in Chapter 4 is a new way to connect the worlds of acoustics and chemistry by effectively switching on chemical nanofactories. The presented structure opens avenues for many therapeutic applications of enzymes, such as enzyme prodrug therapy and amino acid depletion. The demonstrated 15-fold increase in activity upon rupture is just a starting point, with no foreseen theoretical limit to the selectivity. Also, the bioconjugation chemistry which was used for β-lactamase is applicable to many other enzymes

The ultrasound-ruptured liposome can easily be adapted to deliver antibody-based therapeutics, immunostimulatory compounds, or other proteins. One application of interest is the delivery of those enzymes used by neutrophils to kill bacteria. The combination of glucose oxidase and myeloperoxidase is capable of converting native glucose into hydrogen peroxide, and then into hypochlorous acid. This potent product (a key component in bleach) is very damaging to biomolecules, and its highly reactive nature makes it difficult for cells to develop a method of resistance. The short half-life of hypochlorous acid (0.4 ms) keeps the effects localized to the region containing enzyme. Also, since production of hypochlorous acid depends on the sequential activity of both enzymes, the efficiency of the two-enzyme system increases with the square of enzyme concentration.

Another category of enzymes which can be applied towards cancer medicine are those which can digest collagen, often referred to as collagenases. Solid tumors are prone to desmoplasia, the growth of a thick stroma layer of extracellular matrix proteins surrounding the

tumor. A reactive stroma is associated with tumorigenesis and poor prognosis and acts as a protective barrier to treatment[287-290]. This is especially prevalent in pancreatic ductal adenocarcinoma, where it increases the interstitial fluid pressure, thereby decreasing the penetration of molecules[291, 292]. The poor access of chemotherapy drugs to the tumor is thought to be one factor contributing to the poor survival rate of pancreatic cancer patients[293]. Targeting the stroma with degrading enzymes or growth factor inhibitors has been shown to enhance the permeation of molecules into the tumor, and improve the efficacy of chemotherapy[294-297]. However, the ubiquity and structural significance of collagen in other parts of the body poses a danger to the nonspecific delivery of collagenase. Therefore, a logical application of the URL is to delivery such enzymes locally, to reduce dangerous side effects, and provide access for a subsequently administered chemotherapy agent.

7.3 Ultrasound-Ruptured Liposomes for Nucleic Acid Delivery

The same challenges of short circulation, lack of protection, and lack of specificity which apply to immunogenic compounds also apply to gene delivery and gene silencing approaches. Similarly, the URL has the potential to be an excellent delivery vehicle for nucleic acids due to its ability to trigger a shift in the state of a nucleic acid from protected and long circulating to exposed and ready to transfect. A transfection complex which would normally function poorly in vivo due to rapid clearance and accumulation in the lungs, liver, and spleen could be encapsulated inside of the URL to add this functionality.

7.4 Nucleation Sites and Ultrasound-Ruptured Liposomes for Sonothrombolysis

Cancer treatment is not the only application to benefit from localizing therapeutic effects. Cavitation nucleation sites, specifically perfluorocarbon nanoemulsions may in the future serve as ultrasound sensitizers for sonothrombolysis. In time-critical situations (such as a stroke), the

application of high intensity ultrasound is a rapid way of breaking up a clot and restoring blood flow[298-300]. A purely physically-based method may be a viable alternative for patients ineligible of treatment with tissue plasminogen activator (tPA)[301]. Microbubbles (MB) and other nucleation sites lower the US intensity required to induce cavitation, and consequently allow for more cavitation to occur without causing tissue heating which itself can cause necrosis and be thrombogenic[302-305]. In addition, the nucleation sites, too large to extravasate through normal blood vessels, restrict cavitation to the vascular space and thus prevent undesired cavitation in surrounding tissue.

As mentioned earlier, the benefits of using of PFC particles as sensitizers are due to their biocompatibility, eventual elimination through exhalation, and prior clinical use. PFC MBs are too short-lived in vivo and too large to penetrate well into a clot for efficient seeding of cavitation. Though they have been shown to facilitate sonothrombolysis, MBs do not persist after cavitation, and instead flash into solution, so there is no opportunity to continually use MBs as nucleation sites. Instead, it is necessary to wait after an US pulse for a new set of MBs to flow in, a challenge in a blood vessel with restricted flow. For this reason, people have looked into using low boiling point liquid PFCs as nucleation sites. Even if these can be made stable through circulation, generating a significant amount of cavitation with low boiling point PFCs is accompanied by the generation of a large amount of PFC bubbles. The 100-fold volume increase from the liquid-to-gas transition poses a danger by creating potential emboli, and is a strategy pursued to starve tumors through blood vessel occlusion[191, 306].

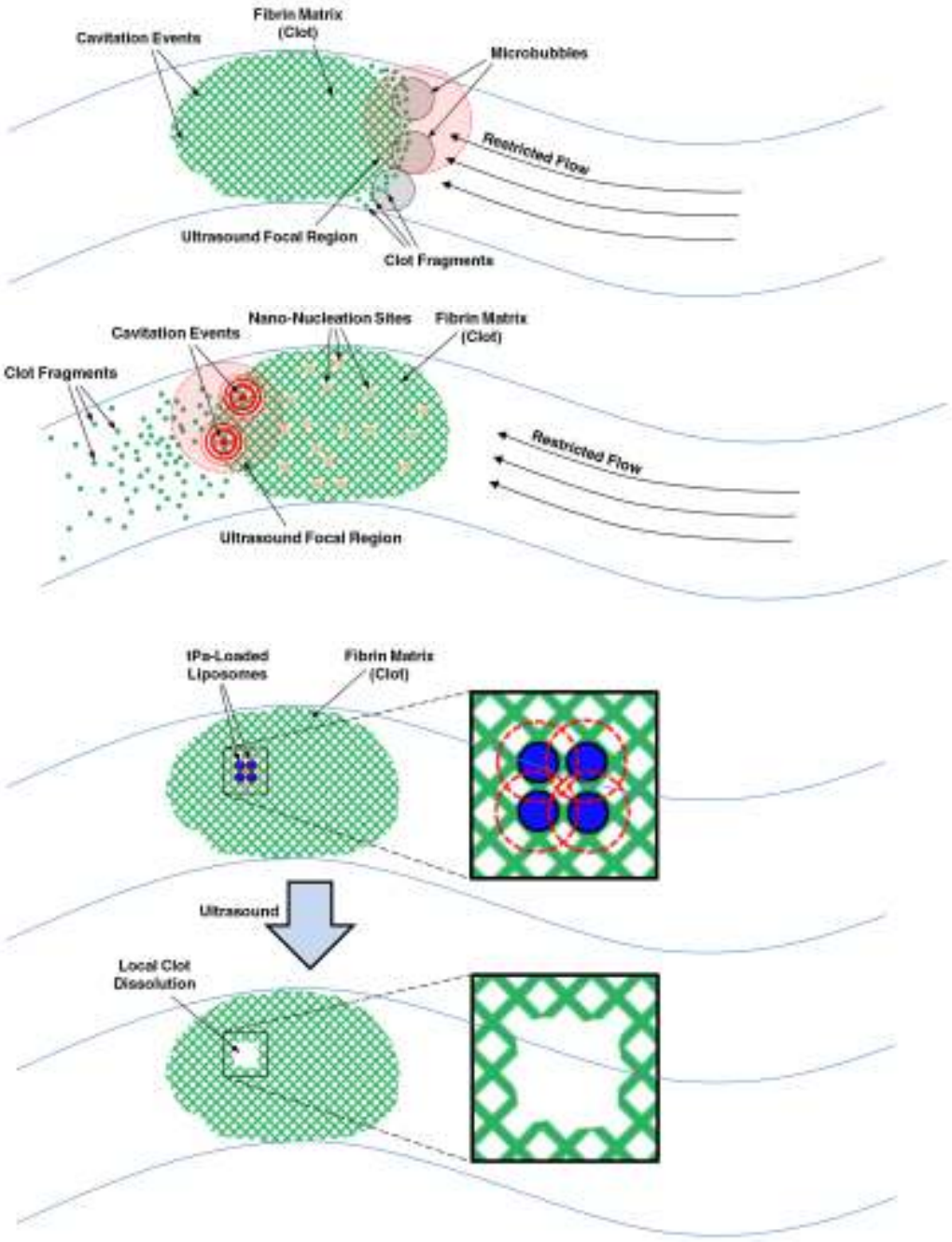

Figure 7.1 Strategies for particle-enhanced sonothrombolysis. a) Existing approaches have used microbubbles to enhance local mechanical effects, such as cavitation. However, microbubbles are too large to achieve efficient penetration into the clot. b) Nanoemulsions may better penetrate into the clot, and may act as persistent cavitation nucleation sites for effective clot lysis. c) tPa loaded URL can be ruptured with ultrasound to cause local clot dissolution, reducing the required systemic dose.

The higher boiling point PFCs described in this dissertation remain liquid or rapidly turn back into liquid after cavitation, and have no risk of spontaneous vaporization in vivo. In addition, since they can be made as small as 20 nm, they are likely to better penetrate a clot, and break the clot into smaller fragments which are less likely to create downstream emboli.

The ultrasound-ruptured liposome could provide an effective seed for cavitation while simultaneously releasing a clot-dissolving compound, such as tPA or heparin. The local release of these drugs could reduce the required dose and potentially mitigate dangerous side effects such as hemorrhage and edema[307]. Furthermore, PFC emulsions, with their ability to dissolve high quantities of oxygen, could have a secondary effect of providing oxygen to the deprived tissue.

7.5 Ultrasound-Driven Micro/Nano Projectiles

The microbullets described in Chapter 5 show a step towards the development of the magic bullet, by creating a method for externally controlled, highly energetic motion. The particles shown here were significantly faster and more energetic than previous micromachines and did not depend on the presence of an externally-located fuel source, which could enable their application in living systems where the environment cannot be controlled as it can in in vitro systems.

Still, a few key steps need to be taken to prepare these particles for in vivo studies. Their size must be greatly scaled down, so that the bullet diameter is at most 100 nm. To maintain directed propulsion instead of chaotic motion, this would also require shortening the length significantly. Also, although the microbullets demonstrated here were fabricated from metals, similar structures could be made using biodegradable polymers. The key characteristic is the conical/tubular geometry for directed propulsion and a strong material which can resist the destructive power of cavitation. Though some breakage of the material could be acceptable, like

shrapnel, the shatter of the bullet into very small nanofragments would likely limit their ability to penetrate multiple layes of cells due to dominant drag forces.

Once these requirements are met, the new biodegradable nanobullet could possess similar characteristics to biolistic (gene gun) devices, which can currently only be used for superficial tissues. The circulating particle could be loaded with nucleic acids so that transfection can be induced at specific targets using focused ultrasound. Such an ability could be applied for immunotherapy, enzyme-prodrug therapy, direct cell killing, and gene replacement to name a few.

7.6 Ultrasound Modulated Fluorescence Contrast Agents

The fluorescent microbubble described in Chapter 6 enables a method to control fluorescence emission with ultrasound, potentially for a hybrid imaging modality. The detected modulation shows the ability to detect the bubbles in a medium free of scattering. However, the realization of this modality will require strengthening the signal so that it may be detected even through a scattering medium. Adaptation of the bubble's fluorescence to a near infrared wavelength can aid in maximizing the signal through reduced tissue absorption, and slightly decreasing scattering. Hardware improvements such as an optical system optimized for collection of scattered light, and a lock-in amplifier also have the potential to improve the system's sensitivity.

7.7 Translation to Clinical Practice

The work described in this dissertation opens the doors to a variety of clinically-applicable technologies. Most of this work is in the discovery/early development stage, and significant advances are needed before commencing testing in humans. Systematic animal studies are needed to demonstrate safety and optimize pharmacokinetics and efficacy as a function of

formulation and ultrasound treatment procedure. The described liposome technologies are at this stage and have the potential to accelerate quickly to large animal preclinical studies. The microbullet and microbubble particles described in Chapters 5 and 6 still require in vitro development before they can be tested in animal models.

7.8 References

286. Hersh, E.M., Whitecar, J.P., Jr., McCredie, K.B., Bodey, G.P., Sr. & Freireich, E.J. Chemotherapy, immunocompetence, immunosuppression and prognosis in acute leukemia. *The New England journal of medicine* **285**, 1211-1216 (1971).

287. Bhowmick, N.A. & Moses, H.L. Tumor-stroma interactions. *Current opinion in genetics & development* **15**, 97-101 (2005).

288. Kim, J.B., Stein, R. & O'Hare, M.J. Tumour-stromal interactions in breast cancer: the role of stroma in tumourigenesis. *Tumour biology : the journal of the International Society for Oncodevelopmental Biology and Medicine* **26**, 173-185 (2005).

289. Finak, G. et al. Stromal gene expression predicts clinical outcome in breast cancer. *Nature medicine* **14**, 518-527 (2008).

290. Jessani, N. et al. Carcinoma and stromal enzyme activity profiles associated with breast tumor growth in vivo. *Proceedings of the National Academy of Sciences of the United States of America* **101**, 13756-13761 (2004).

291. Heldin, C.H., Rubin, K., Pietras, K. & Ostman, A. High interstitial fluid pressure - an obstacle in cancer therapy. *Nature reviews. Cancer* **4**, 806-813 (2004).

292. Mahadevan, D. & Von Hoff, D.D. Tumor-stroma interactions in pancreatic ductal adenocarcinoma. *Molecular cancer therapeutics* **6**, 1186-1197 (2007).

293. Milosevic, M. et al. Interstitial fluid pressure predicts survival in patients with cervix cancer independent of clinical prognostic factors and tumor oxygen measurements. *Cancer research* **61**, 6400-6405 (2001).

294. Provenzano, P.P. et al. Enzymatic targeting of the stroma ablates physical barriers to treatment of pancreatic ductal adenocarcinoma. *Cancer cell* **21**, 418-429 (2012).

295. Bouzin, C. & Feron, O. Targeting tumor stroma and exploiting mature tumor vasculature to improve anti-cancer drug delivery. *Drug resistance updates : reviews and commentaries in antimicrobial and anticancer chemotherapy* **10**, 109-120 (2007).

296. Skliarenko, J.V. et al. Effects of the vascular disrupting agent ZD6126 on interstitial fluid pressure and cell survival in tumors. *Cancer research* **66**, 2074-2080 (2006).

297. Tong, R.T. et al. Vascular normalization by vascular endothelial growth factor receptor 2 blockade induces a pressure gradient across the vasculature and improves drug penetration in tumors. *Cancer research* **64**, 3731-3736 (2004).

298. Meairs, S., Alonso, A. & Hennerici, M.G. Progress in sonothrombolysis for the treatment of stroke. *Stroke; a journal of cerebral circulation* **43**, 1706-1710 (2012).

299. Molina, C.A. et al. Transcranial ultrasound in clinical sonothrombolysis (TUCSON) trial. *Annals of neurology* **66**, 28-38 (2009).

300. Kaul, S. Sonothrombolysis: a universally applicable and better way to treat acute myocardial infarction and stroke? Who is going to fund the research? *Circulation* **119**, 1358-1360 (2009).

301. Eggers, J., Seidel, G., Koch, B. & Konig, I.R. Sonothrombolysis in acute ischemic stroke for patients ineligible for rt-PA. *Neurology* **64**, 1052-1054 (2005).

302. Soltani, A. et al. Potentiating intra-arterial sonothrombolysis for acute ischemic stroke by the addition of the ultrasound contrast agents (Optison & SonoVue((R))). *Journal of thrombosis and thrombolysis* **31**, 71-84 (2011).

303. Storm, F.K., Harrison, W.H., Elliott, R.S. & Morton, D.L. Normal tissue and solid tumor effects of hyperthermia in animal models and clinical trials. *Cancer research* **39**, 2245-2251 (1979).

304. el-Sabban, F. & Fahim, M.A. Local cerebral hyperthermia induces spontaneous thrombosis and arteriolar constriction in the pia mater of the mouse. *International journal of biometeorology* **38**, 92-97 (1995).

305. Khairy, P. et al. Lower incidence of thrombus formation with cryoenergy versus radiofrequency catheter ablation. *Circulation* **107**, 2045-2050 (2003).

306. Samuel, S., Duprey, A., Fabiilli, M.L., Bull, J.L. & Brian Fowlkes, J. In vivo microscopy of targeted vessel occlusion employing acoustic droplet vaporization. *Microcirculation* (2012).

307. Adibhatla, R.M. & Hatcher, J.F. Tissue plasminogen activator (tPA) and matrix metalloproteinases in the pathogenesis of stroke: therapeutic strategies. *CNS & neurological disorders drug targets* **7**, 243-253 (2008).